UNIVERSIDAD
DE LA REPUBLICA
URUGUAY

UNIVERSITÉ DE
GRENOBLE

THÈSE

Pour obtenir le grade de

DOCTEUR DE L'UNIVERSITÉ DE GRENOBLE

préparée dans le cadre d'une cotutelle entre l'*Université de Grenoble* et l' *Universidad de la República, Montevideo, Uruguay*

Spécialité : **Physique Appliquée**

Arrêté ministériel : le 6 janvier 2005 -7 août 2006

Présentée par

Javier BRUM

Thèse dirigée par **Carlos NEGREIRA** et **Stefan CATHELINE**

préparée au sein du **Laboratorio de Acústica Ultrasonora** et **l'Institut des Sciences de la Terre**

dans **le PEDECIBA - Física et l'École Doctorale de Physique**

Elastographie et retournement temporel des ondes de cisaillement: application a l'imagerie de solides mous

Thèse soutenue publiquement le **23 novembre 2012**,
devant le jury composé de :

Mr. Horacio FAILACHE
DR. Universidad de la República, Montevideo, Président
Mr. Michelle CAMPILLO
Pr. Université de Grenoble, Membre
Mr. Mathias FINK
Pr. Université Diderot, Paris, Membre
Mr. Mickaël TANTER
DR. INSERM, Paris, Rapporteur
Mr. Ricardo ARMENTANO
Pr. Universidad Favaloro, Buenos Aires, Rapporteur
Mr. Carlos NEGREIRA
Pr. Universidad de la República, Montevideo, Membre
Mr. Stefan CATHELINE
DR. INSERM, Lyon, Membre

*Université Joseph Fourier / Université Pierre Mendès France /
Université Stendhal / Université de Savoie / Grenoble INP*

Résumé

L'interaction onde-matière a toujours été un sujet d'étude en Physique, c'est le cas de la propagation des ondes élastiques dans le corps humain qu'a conduit à plusieurs modalités d'imagerie. En particulier, les techniques d'elastographie reposent sur l'utilisation des ondes de cisaillement pour obtenir une image élastique des tissus mous. Dans ce contexte, cette thèse présente une étude des différentes techniques d'élastographie, en prêtant particulier attention aux aspects plus fondamentaux comme à ces potentielles applications.

Tout d'abord, cette thèse montre que l'élastographie impulsionnelle unidimensionnelle (1D) peut être utilisée pour évaluer l'élasticité des couches de tissue d'épaisseur inférieure à la longueur d'onde utilisée. A cet effet, des simulations et des expériences ont été réalisées avec différents fantômes formés par une couche mince immergée dans un milieu d'élasticité différente. La concordance entre expériences et simulations, ainsi que le valeur de l'élasticité obtenue par élastographie 1D et le valeur de l'élasticité intrinsèque de la couche permettent de valider cette technique. Au même temps ces résultats ont été comparés avec ceux obtenus par la technique de Supersonic Shear Imaging (SSI), où l'onde est guidée le long de la plaque. On ajustant la courbe de dispersion expérimentale obtenue par SSI avec un modèle de Lamb, l'élasticité intrinsèque de chaque plaque est estimée. Les résultats obtenus par élastographie 1D et SSI montrent un bon accord entre eux. Le principal avantage de l'élastographie 1D est qu'il n'est pas nécessaire d'utiliser un modèle pour estimer l'élasticité de la plaque.

Deuxièmement, deux nouvelles modalités d'imagerie quantitative pour l'extraction de élasticité des tissus mou à partir d'un champ élastique complexe sont approfondies: l'Elastographie par Retournement Temporel et le filtre inverse passif. Le but de ces deux techniques est d'estimer localement l'élasticité des tissus, par la mesure de la taille de la tâche focale dans une expérience virtuelle de retournement temporel avec des ondes de cisaillement. A partir de l'étude du processus de retournement temporel dans les solides mous, la faisabilité de ces deux techniques est démontrée *in vitro* dans des échantillons "bi-couche" et *in vivo* dans le foie et les muscles, en utilisant le bruit physiologique naturel crée par l'activité cardiaque et musculaire. L'efficacité de l'élastographie par retournement temporel diminue dans le cas d'un champ diffus non isotrope. L'emploie du filtre inverse adaptée à une configuration de source de bruit, permet de rétablir l'isotropie du champ et d'améliorer la résolution pour la détection de petites inclusions. Le filtre inverse passif permet, de surcroît, de contrôler la fréquence qui domine le champ de retournement temporel. Ceci est exploité, dans la dernière partie du manuscrit, pour mener la première expérience de spectroscopie passive en volume. Deux situations sont envisagées: la

dispersion due à la propagation d'ondes guidées dans des plaques minces et la dispersion des ondes due à la viscosité.

Abstract

The interaction between wave and matter has long been studied in Physics. In particular, regarding medical applications, wave propagation through the human body resulted in several imaging modalities, each of which uses a specific type of wave linked to a given physical property. The elasticity of soft biological tissues is directly linked to its shear wave speed. Thus, in Elastography, shear waves are tracked for non-invasive assessment of the mechanical properties of soft tissues. In this context, this thesis proposes a study of different elastography techniques from a basic point of view, as well as from its potential applications.

Firstly, in this manuscript, the use of 1D transient elastography for the quantitative elasticity assessment of thin layered soft tissues is proposed. Experiments on three phantoms with different elasticities and plate thicknesses were performed. Experimental shear wave speed estimations inside the plate were obtained and validated with finite difference simulation. In addition, the Supersonic Shear Imaging (SSI) technique was performed. For the SSI technique, the propagating wave inside the plate is guided as a Lamb wave. Experimental SSI dispersion curves were fitted using a generalized Lamb model to retrieve the plate bulk shear wave speed. Finally both techniques resulted in similar shear wave speed estimations. The main advantage of 1D transient elastography is that the bulk shear wave speed can be directly retrieved from a time of flight measurement without requiring a dispersion model.

Secondly, throughout this thesis, two novel quantitative imaging modalities for extracting the soft tissue's elasticity from a complex reverberated diffuse elastic field are deepen: Time Reversal Elastography (TRE) and the passive inverse filter. The goal of both techniques is to locally estimate the tissue's elasticity, by measuring the focal spot size in a virtual time reversal experiment involving shear waves. By studying the Physics of a time reversal process in soft solids, the feasibility of both techniques as a quantitative imaging techniques is demonstrated *in vitro* in bi-layer phantoms and *in vivo* in the liver-belly muscle, by using the physiological noise due to heartbeats and muscular activity. The efficiency of TRE decreases in the presence of a non-isotropic diffuse field. The use of the inverse filter adapted to a passive source configuration, restores the isotropy of the field. As a consequence, the resolution of the elasticity images is improved, leading to a better detection of small inclusions. In addition, the passive inverse filter allows to control the frequency dominating the time reversed field. This is exploited in the last part of the manuscript to conduct the first passive wave spectroscopy experiment in the volume of a soft solid. Two situations are considered: dispersion due to guided wave propagation in thin plates and wave dispersion due to viscosity effects.

Acknowledgments

A PhD thesis is a long three years journey. Now, sitting in front of this last blank page, I would like to dedicate a few lines to all the people that accompanied me along this trip.

I would like to express my heartfelt thanks to Dr. Carlos Negreira and Dr. Stefan Catheline, my advisors, for the guidance and support throughout this thesis. You have been great mentors. Thank you Stefan for your patience and endless "skype" hours. You taught me a unique way to see and interpret Physics. Carlos, you always struggled to give your students the best opportunities, for that I will be forever grateful. Thank you for the trust and advices which kept me always motivated.

I am also very grateful to the members of the thesis committee Dr. Michel Campillo, Dr. Mathias Fink, Dr. Horacio Failache, Dr. Mickaël Tanter and Dr. Ricardo Armentano for taking their time to read this dissertation. In particular, I would like to thank the "french part" of the committee for being here today. I am very glad and honored with your presence.

I would like to extend a warm gratitude to Dr. Jean Luc Gennisson who kindly received me in Paris and assisted me through many passages of Chapter II. It was a real pleasure working with you. I am very pleased that you are here today.

The Laboroatorio de Acústica Ultrasonora has been an integral part of my academic life. I would like to thank all the people in the ultrasound laboratory for their friendship and support. In particular to Dr. Nicolás Benech for the fruitful discussions that inspired several passages of this thesis and to MSc. Guillermo Balay whose energy and determination is always an inspiration.

Moreover, during this three years I spent 1/3 of the time in Grenoble. I would like to thank all the members of the Institute des Sciences de la Terre (former LGIT) who kindly received me during my stays, in particular, to the team "Ondes et Structures". The great ambience in the laboratory made me feel at home.

I would like to thank PEDECIBA Fisica, in particular to Jimena Rodriguez and Ana Ines Zambrana for their administrative assistance. Thanks to the ANII (Agencia Nacional de Investigación e Innovación, Uruguay) and to the French Embassy at Montevideo for their financial support. In particular I would like to express a warm thanks to Ms. Graciela Vigo for her administrative assistance.

Many people helped me directly and indirectly during the past three years, I would like to extend my acknowledgments to them. In particular to Miguel ("mon guide de montagne") and Tatiana, two very dear persons I had the chance to encounter in Grenoble. Thank you Thu-Mai for the discussions on guided wave propagation, Martin for "tuning up" my presentation and Cecilia for correcting my English. Thanks to my dearest friends from all times: Alfa, Nico, Pablo, Cutu, Seba, Diego, briefly, to all the "Muchachotas". Thank you Alejo, Cecilia, Juan and Maria for all the support, especially during this last year.

I was blessed with an incredibly loving family, my parents, Gustavo and Patricia, and my brother Federico. I would like to dedicate this thesis to you. What I am today, I owe it to you. Finally, but never last, I extend a deep heartfelt "thank you" to the two suns in my life, Cecilia, my wife, and Lucas, my son. Without your support and encouragement this thesis would not have been possible. I love you deeply.

To Ramiro

Table of Contents

Chapter IV

Chapter V

Introduction

The interaction between wave and matter has long been studied in Physics. In a non exhaustive list it can be mentioned seismology, acoustics, classic and quantum optics, fluid and solid state physics. From the propagation of different types of waves, the material properties can be directly, or indirectly, measured. In particular, regarding medical applications, wave propagation through the human body resulted in several imaging modalities, each of which uses a specific type of wave linked to a given physical property. For example, ultrasonic waves used in echography, reveal the tissue's acoustical impedance. The electromagnetic waves used in X-Ray tomography or in Nuclear Magnetic Resonance, which are respectively linked to the electromagnetic absorption and spin relaxation time, are used to image bones and organs with a very high resolution. In this direction, for the past two decades, several techniques based on shear wave propagation, were developed for non-invasive assessment of the mechanical properties of soft tissues with application to medical diagnosis. These techniques were termed as Elastography.

Elastography techniques can mainly be divided in two groups: static and dynamic elastography. In Static Elastography, a compression is applied by pressing an ultrasonic probe on the tissue. Ultrasonic waves are used to obtain a strain map by comparing the displacements before and after each compression. Based on Hooke's Law, hard tissue will deform less than soft tissue, when submitted to the same stress. Thus, the obtained strain image will be proportional to the tissue's stiffness. However due to the lack of information on the stress to which the tissue is submitted, this method does not provide a quantitative elasticity estimation. To overcome this limitation, a set of techniques, based on shear wave propagation inside the tissue, have been developed during the past decade. The speed at which the shear waves propagate inside the tissue is directly linked to the tissue's stiffness, providing a quantitative estimation of the tissue elasticity. These techniques can be categorized under the name Dynamic Elastography. Dynamic Elastography techniques can be sub-divided in two groups: active and passive techniques. Passive Elastography techniques take advantage of the shear waves naturally present in the human body to conduct an elastography experiment. On the other hand Active Elastography techniques use artificially induced shear waves, which are generated by carefully applying a controlled external source.

The first part of this manuscript is devoted to the active elastography techniques, in particular to the one dimensional (1D) transient elastography technique and its applicability for the elasticity assessment of thin layered soft tissue. For this purpose, in Chapter I, in a non exhaustive list, several elastography techniques are presented: 1D transient elastography, magnetic resonance elastography, Acoustic Radiation Force Imaging (ARFI), Supersonic Shear Imaging (SSI), etc. The physics behind each technique, as well as it advantages and limitations will be briefly discussed. All of the aforementioned techniques have been successfully applied to determine non-invasively the mechanical parameters of living tissue such as breast, liver or muscle. Recently, elasticity estimation of thin layered soft tissues has gained increasing interest propelled by medical applications like skin, cornea or arterial wall elasticity assessment.

In Chapter II the use of 1D transient elastography for the quantitative elasticity assessment of thin layered soft solids is proposed. Experiments on three phantoms with different elasticities and plate thicknesses were performed. Firstly, using 1D transient elastography the shear wave speed dispersion curve inside the plate was obtained and validated with finite difference simulation. No dispersive effects were observed and the shear wave speed was directly retrieved from time-of-flight measurements. Secondly, the SSI technique (considered as a gold-standard) was performed. For the SSI technique, the propagating wave inside the plate is guided as a Lamb wave. In this thesis a general Lamb model is proposed, since the plates under study were surrounded by an elastic medium. Experimental SSI dispersion curves were compared with finite difference simulation and fitted using the Lamb model to retrieve the plate bulk shear wave speed. Finally, the results obtained by 1D transient elastography and SSI are discussed and compared.

During the first part of this manuscript, attention was focused in two particular active elastography techniques: 1D transient elastography and SSI technique. Both techniques have one thing in common: they use a controlled source to generate the shear wave. In the second part of the manuscript, a completely different approach is proposed. Two novel imaging modalities for extracting the soft tissue's elasticity from a complex reverberated elastic field generated by a set of uncontrolled sources are presented: Time Reversal Elastography (TRE) and the Passive Inverse Filter.

The key concept in TRE is the use of spatiotemporal correlations interpreted in the frame of the time-reversal symmetry. Time reversal has shown to be an efficient way to focus a wave back to its source. The original idea was proposed in the nineties by *M. Fink et al.* [1] and is based on the time-reversal invariance of the wave equation in a lossless medium. According to the Rayleigh criterion, the focal spot width is directly related to the wavelength and therefore depends on the mechanical properties of the medium. Thus, the general idea of TRE is to extract a quantitative elasticity estimation using a time-reversal approach based on cross-correlations of the wave field. The first steps of the TRE technique were given in the Laboratorio de Acústica

Ultrasonora (L.A.U.), Facultad de Ciencias, Universidad de la República, between 2007 and 2009, in the works of *Catheline et al.* [2], *Benech et al.* [3] and *Brum et al*. [4]. In these works, an external source creates mechanical waves inside a tissue mimicking phantom. One component of the displacement field is measured along a line by means of an ultrasonic speckle interferometry technique. From the time reversal point of view, the shear elasticity can be obtained by two different ways: measuring the wave speed as the wave converges or measuring the focal width. Then, the global shear elasticity is deduced from the reverberated mechanical waves by using spatiotemporal correlations interpreted in the frame of the time-reversal symmetry. The advantage of the TRE technique is its independence on the source kind, shape, and time excitation function. This robustness as regard to shear wave source allows thinking in applications of this technique in the medical field, in particular for passive elastography experiments.

In Chapter III the feasibility of the TRE technique as a novel quantitative imaging modality will be demonstrated. In particular, its potential as a passive elastography technique is tested *in vivo* in the liver-belly muscle. First, in order to validate the technique *in vitro* experiments on a bi-layer tissue mimicking phantom were performed. Since the idea is to extract the shear elasticity from a complex elastic field, the following two step experiment is conducted: in a first step, a complex wave field is created inside the phantom by random fingers impacts from its surface. The displacement field is measured inside the sample by means of an ultrasonic speckle tracking technique. In a second step a virtual time-reversal experiment is performed in the computer by using either normalized correlation or phase correlation. Shear waves will be virtually focused on each imaging point, resulting in a 2D focus. By locally measuring the focal size a shear wavelength tomography is conducted, resulting in shear elasticity image. In order to retrieve a quantitative elasticity estimation, an analytical expression relating the spatial focalization size with the shear wave speed is developed in this thesis. Second, to show the potential of TRE as an passive imaging technique, a feasibility *in vivo* study in the human liver was carried out. For this case, the complex elastic field is created by the physiological noise present in the human body due to cardiac beating and breathing. To conclude Chapter III, the potential of the TRE technique for imaging small inclusions embedded in a larger medium will be tested. Contrary to the bi-layer mediums, the inclusions could not be satisfactory resolved using TRE, leading to several image artifacts. The cause of this problem lies in the directivity of the time reversed field. Since the source distribution in the noise experiments is not homogeneously distributed, the resulting time reversed has a privileged propagation direction, leading to deformed focal spots due to diffraction effects.

In Chapter IV a solution to this problem is proposed by adapting the technique known as inverse filter to the particular case of a passive source configuration: the passive inverse filter. With such a passive inverse filter the spatial distribution of noise sources is made homogeneous. As a result better resolved images are obtained, or in other words a better Green's function reconstruction is achieved, when compared to the standard cross correlation. The passive inverse filter will be tested for the same experiments presented in Chapter III: bi-layer medium, inclusions and *in vivo* passive elastography. The obtained shear wave speed maps will be presented and compared to the ones obtained by normalized/phase correlation.

But directivity correction of the time reversed field is not the only advantage of the passive inverse filter. In addition, the temporal frequency dominating the time reversed field is also controlled through the passive inverse filter. In Chapter V the advantage of having a monochromatic focalization will be exploited to measure wave dispersion from a complex reverberated field. Firstly, the ability of the passive inverse filter for measuring wave dispersion will be tested in metals. A finite difference simulation is conducted in a metallic bar, where wave propagation is known to be highly dispersive. Then, an experiment is carried out in a stainless steel plate where the complex reverberated field is known to be dominated by Lamb waves. Secondly, the passive inverse will be used to measure the shear wave dispersion in the case of the elastography experiments presented throughout this thesis. Two situations will be considered: guided wave propagation in a soft solid thin layer and dispersion due to viscosity effects.

Chapter I

Elastography: a remote palpation method

The stiffness of living tissue is an important medical parameter which can often be related to pathology. For example the presence of cirrhosis results in an abnormal hardening of the liver. In fact, the aforementioned link between the mechanical parameters of living tissue and pathology is the basis for the palpatory diagnosis of various diseases, such as detection of cancer nodules in the breast or prostate. However, palpatory diagnosis is a qualitatively methodology which depends on the examiner personal knowledge and expertise. Thus, to help medical diagnosis several techniques were developed within the past two decades for non-invasive assessment of the mechanical properties of living tissues. These set of techniques were named as Elastography. The physical magnitude which is sensed through palpation is the Young's modulus Y, which describes the tendency of an object to deform along an axis when opposing forces are applied along that axis. It is defined as the ratio between tensile stress σ (compression per unit area) and tensile strain ϵ (fractional change in length):

$$Y = \sigma/\epsilon \tag{1.1}$$

The constitutive relation between stress and strain for a linear, elastic, isotropic medium (Hooke's Law) is given by

$$\sigma_{ij} = 2\mu\epsilon_{ij} + \lambda\epsilon_{kk}\delta_{ij} \tag{1.2}$$

Where σ is the stress tensor, ϵ the strain tensor and λ and μ are the Lamé constants. In Eq. 1.2, the Einstein summation convention has been used and δ_{ij} denotes the Kronecker's delta equal to 1 if $i = j$ and 0 otherwise. The Lame constant λ is usually referred as bulk modulus and characterizes how the tissue's volume changes in response to a compression. Contrary, the shear modulus μ quantifies how tissue responds to shear stresses. Thus, based in Eq. 1.1 and Hooke's Law (Eq. 1.2), the Young's modulus for an homogeneous, isotropic elastic solid can be calculated as:

$$Y = \mu\frac{3\lambda+2\mu}{\lambda+\mu} \tag{1.3}$$

For soft tissues $\lambda \gg \mu$ ($\lambda/\mu \sim 10^6$), this is reflected by the fact that soft tissue is difficult to compress but easy to shear. In Fig. 1.1 a schematic representation of the compression and shear modulus value for different types of tissue is presented. As a consequence of the relation between λ and μ ($\lambda \gg \mu$), by approximating Eq. 1.3, the Young's modulus of soft tissues can be considered to be proportional to the shear modulus:

$$Y \cong 3\mu \tag{1.4}$$

Thus the goal of each elastographic technique is to measure no invasively the Young's modulus or equivalently the shear modulus of living tissue.

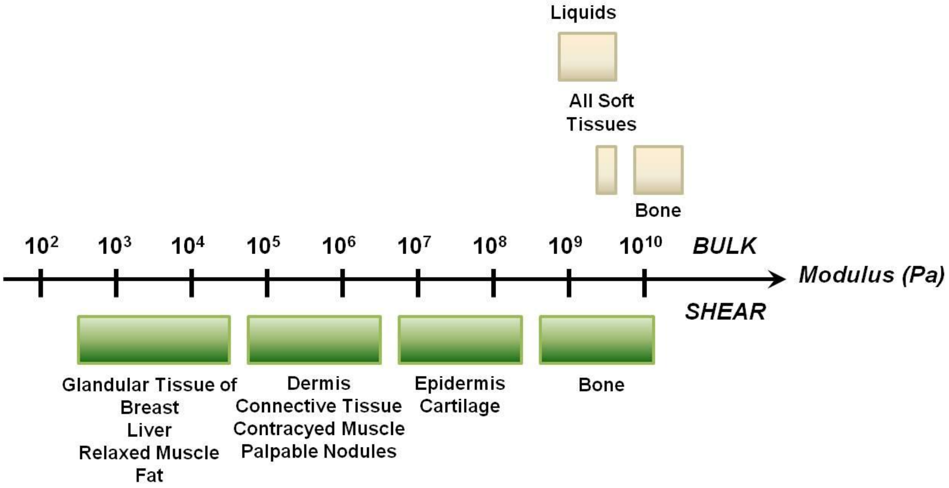

Fig. 1.1 Bulk and shear modulus for different tissues. **Source:** ***Sarvazyan et al.*** **[5]**

The first steps in this direction were given by *Ophir et al.* in the early nineties. Their approach was termed Static Elastography [6],[7]. In Static Elastography a compression is applied by pressing an ultrasonic probe on the tissue. A strain image is obtained by comparing the displacements before and after each compression through a radio frequency data cross-correlation algorithm. Based on the Young's modulus definition (Eq. 1.1) hard tissue (higher Young's modulus) will deform less than soft tissue when submitted to the same stress. Thus, the obtained strain image will be proportional to the tissue Young's modulus. A schematic representation of this procedure is shown in Fig. 1.2.

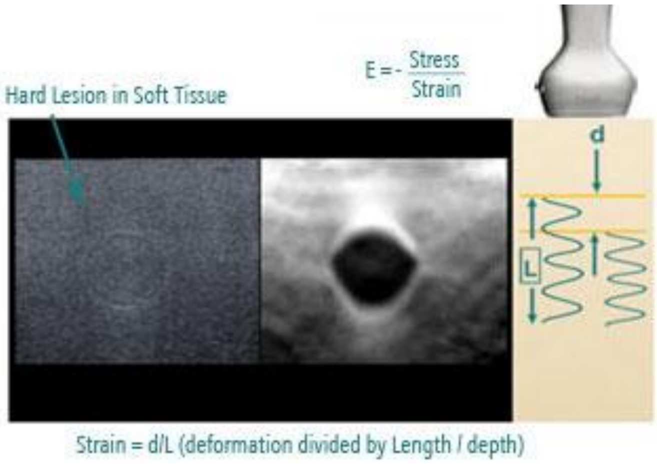

Fig. 1.2 Schematic representation of the strain imaging principle used in Static Elastography. **Source:** ***medical.siemens.com***

Strain imaging of tissue proved to be capable of displaying the relative responses of hard and soft regions with a high spatial resolution. Nowadays, at least two commercial ultrasound scanners which have incorporated a Static Elastography modulus into their system can be mentioned. Hitachi with its "eMode" modality allows to superimpose to a conventional B-mode image a qualitatively elastogram (Fig. 1.3(a)). This imaging modality is implemented in the Hi Vision 900 echographs. Siemens with its "eSie Tocuh Elastography Imaging", available on the echographs Acuson Antares, developed a similar application (Fig. 1.3(b)). The main drawback of Static Elastography is that due to the lack of information on the stress to which the tissue is submitted, is not possible to invert Eq. 1.1 in order to retrieve a quantitative Young's modulus estimation.

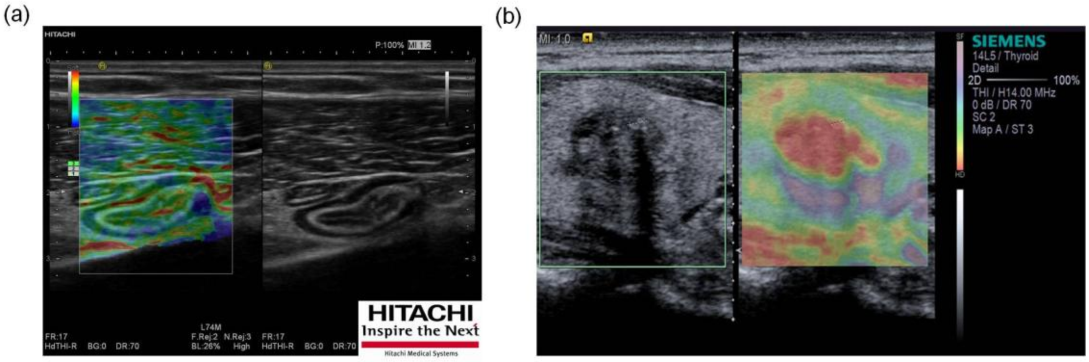

Fig. 1.3 Commercial applications of Static Elastography. (a) Hitachi "eMode". Strain image of the appendix. **Source:** ***hitachimed.com*** (b) Siemens with its "eSie Touch". Strain image of the thyroid. **Source:** ***medical.siemens.com***

Parallel and independently of *Ophirs*'s work another type of elastography technique based on shear wave propagation was developed by *Parker et al.* [8]: the vibration sonoelastography technique. The basic concept behind vibration sonoelastography is that hard tissue will vibrate less in amplitude than soft tissue. Thus by generating with an external source low-amplitude and low-frequency shear waves (typically below 1000 Hz) the vibration response of deep organs is imaged using real-time color Doppler techniques. A hard inhomogeneity, such as a tumor, will be detected since it produces a localized disturbance in the vibration pattern. Sonoelastography imaging was able to identify hard and soft regions with a high spatial resolution. However the main drawback of the technique is that only a relative elasticity image is obtained.

Through both of the aforementioned techniques, which have set the milestone of the actual quantitative elastography techniques, hard lesions were detected but in a qualitatively manner. Thus, the following question arises: is it possible to obtain a local quantitative estimation of the tissue Young's modulus? The answer to this question lies in the mechanical wave propagation through soft tissues, more specifically, as it will be treated in next section, in the shear wave propagation.

1.1: Wave propagation in soft tissues: relation between Young's modulus and shear wave speed

The human body supports the propagation of many types of waves, each of which conveys a specific type of information. In particular, mechanical waves reveal how tissue responds to compression and shear stresses. From the wave equation two different types of wave will emerge from its solution: compressional waves and shear waves. The first type of waves are used in echography at ultrasonic frequencies for obtaining a morphological image of the organs. The second type of wave, the shear wave, will be used to retrieve a quantitative measurement of the tissue Young's modulus as it will be shown below.

By combining Newton's Second Law and Hooke's Law the equation governing an elastic displacement field $\vec{u}(\vec{r},t)$, in the case of an homogeneous, isotropic, elastic solid is given by:

$$(\lambda+2\mu)\nabla(\nabla.\vec{u})+\mu\nabla\times(\nabla\times\vec{u})=\rho\ddot{\vec{u}} \tag{1.5}$$

In Eq. 1.5 ∇ denotes the differential operator with respect to space and the two superposed dots indicate a second order time derivative. The term $(\lambda+2\mu)\nabla(\nabla.\vec{u})$ accounts for the compressional (dilational) portion of the displacement field while the term $\mu\nabla\times(\nabla\times\vec{u})$ accounts for the rotational (equivoluminal) portion. Using Helmholtz decomposition the three dimensional displacement field $\vec{u}$ can be expressed as a sum of a compressional scalar potential ϕ and an equivoluminal vector potential ψ as

$$\vec{u}=\vec{u}_L+\vec{u}_T=\nabla\phi+\nabla\times\psi \tag{1.6}$$

The divergence of ψ is chosen to be identically zero, which implies that the field is solenoidal, i.e. there are no sources or sinks of energy within the region. Specifying the divergence provides the necessary additional condition to uniquely determine the three components of $\vec{u}$ from the four components of the two potentials introduced by Helmholtz decomposition. By substituting Eq. 1.6 into Eq. 1.5 the following two equations are found:

$$\ddot{\vec{u}}_L = \frac{\lambda+2\mu}{\rho}\nabla^2\vec{u}_L \tag{1.7}$$

$$\ddot{\vec{u}}_T = \frac{\mu}{\rho}\nabla^2\vec{u}_T \tag{1.8}$$

Each of the preceding equations corresponds to a conventional wave equation but with different wave speeds. Equation 1.7 describes a compressional wave with a wave speed $c_L = \sqrt{(\lambda+2\mu)/\rho}$. The compressional wave corresponds to sound at audible frequencies and to ultrasound at higher frequencies. When a plane wave solution is imposed to Eq. 1.7, the propagation direction of such wave is parallel to the displacement field $\vec{u}_L$, thus this type of wave is also termed longitudinal. On the other hand Eq. 1.8 describes a shear wave with a wave speed $c_T = \sqrt{\mu/\rho}$. When a plane wave solution is imposed to Eq. 1.8, the propagation direction of such wave is perpendicular to the displacement field $\vec{u}_T$, thus another way to name this type of wave is transverse wave.

To sum up, an isotropic elastic medium characterized by Lamé constants λ and μ supports two types of wave propagation: compressional and shear waves whose speeds are given respectively by:

$$c_L = \sqrt{(\lambda+2\mu)/\rho} \tag{1.9}$$

$$c_T = \sqrt{\mu/\rho} \tag{1.10}$$

Thus, the answer to the question "how is it possible to obtain a local quantitative estimation of the tissue Young's modulus?" lies in Eq. 1.10. As already stated above, due to the high existing contrast between λ and μ in biological tissue, the Young's modulus is directly linked to the shear modulus of the tissue through Eq. 1.4 and as a consequence to the shear wave speed through Eq. 1.10. Thus by combining both equations, the Young's modulus is related to the shear wave speed through the following expression:

$$Y \cong 3\mu = 3\rho c_T^2 \tag{1.11}$$

Thus a way to access the local stiffness of tissue is by locally tracking the shear wave speed. This is the basic concept behind Dynamic Elastography techniques. Throughout this manuscript the concepts of shear wave speed and elasticity will be used indiscriminately, since for soft solids both magnitudes are equivalent.

1.2: Dynamic Elastography: state of the art

The goal in Dynamic Elastography techniques is the assessment of the tissue Young's modulus by measuring the speed of the propagating shear waves. As already demonstrated in the previous section, this approach has the advantage to be quantitative. Dynamic Elastography techniques can be sub-divided in two groups: active and passive techniques. Passive Elastography techniques take advantage of the shear waves naturally present in the human body due to heartbeats, breathing and muscular activity to conduct an elastography experiment [9], [10]. On the other hand Active Elastography techniques use artificially induced shear waves which are generated by carefully applying a controlled external source. They consist basically on three steps: first the tissue is mechanically stressed resulting in a shear wave generation, secondly the induced displacements are imaged and finally the tissue elastic properties are deduced from the measured displacement field. There are several ways to image the displacement field (e.g. ultrasound [11], [12] or nuclear magnetic resonance [13]) and to generate the shear waves (e.g. mechanical vibrator [14]-[16] or ultrasound radiation force [5], [17], [18]). The different combinations of how the shear wave is generated and tracked resulted in several different elastographic techniques. In what follows, a non exhaustive list of the existing active elastography techniques will be presented. Particular interest will be focused in the one dimensional (1D) transient elastography and Supersonic Shear Imaging (SSI) techniques since they will be used and compared in Chapter II to retrieve the shear elasticity of a thin layered soft tissue.

1.2.1 One dimensional transient elastography

One dimensional transient elastography was developed by S. Catheline during his PhD thesis at the Laboratoire Ondes et Acoustique (present Institut Langevin) in 1994 [19]. The experimental setup used in his work is presented in Fig. 1.4(a). It includes an ultrasonic transducer placed in front of a circular mechanical vibrator. The mechanical vibrator is used to send a low-frequency (typically ≈ 100 Hz) transient elastic wave, while the ultrasonic transducer acquires radio frequency lines at a repetition frequency of 1000 Hz. The induced displacement field is retrieved by using an acoustical speckle interferometry technique [19]. The result is displayed in Fig. 1.4(b) in a seismogram-like representation.

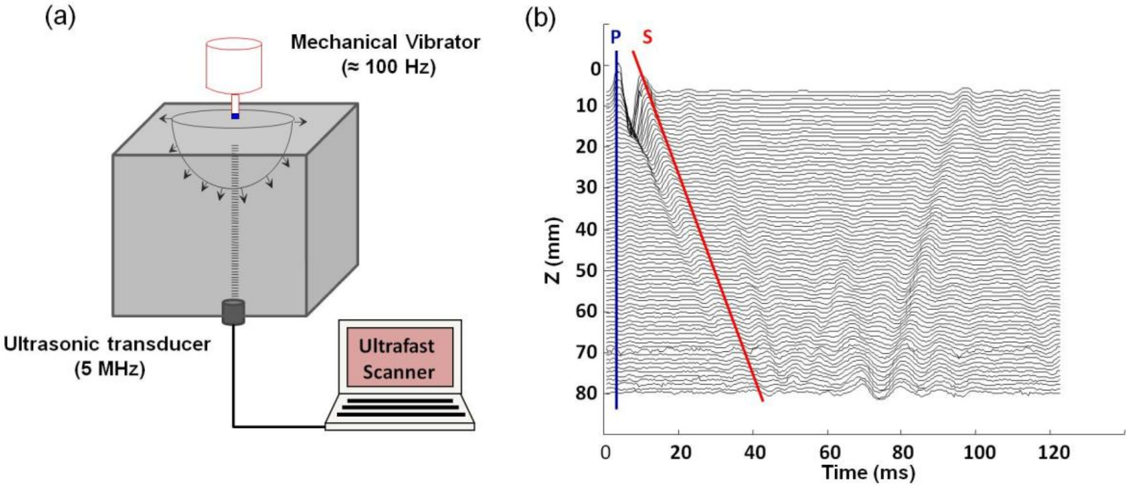

Fig. 1.4 (a) Schematic representation of the experimental setup used in the 1D transient elastography technique. An external vibrator creates a low frequency elastic field inside the sample. (b) Displacement field recorded by means of an ultrasonic speckle interferometry technique. Two types of wave with different speeds are observed: a compressional wave (P) and a shear wave (S). Due to its high speed the compressional wave propagates almost instantaneously throughout the sample while the shear wave propagation is clearly visible. **Source: *Catheline et al.* [14].**

As the piston taps on the phantom' surface two types of waves are generated: a compressional and a shear wave. Due to the cylindrical symmetry of the problem, both wave propagation directions are parallel to the piston's axis. Although shear waves are purely transverse in the far field (where they can be considered as plane waves), they have a longitudinal component in the near field of the piston because of diffraction effects [14], [15]. This fact, represented in Fig. 1.5, can be qualitatively explained using Huygen's principle: the summed contributions of transversely polarized shear waves coming from secondary sources give rise to a globally longitudinally polarized shear wave on the piston's axis. This longitudinally polarized shear wave propagating along the piston axis is denoted by *S* in Fig. 1.4(b). Further details on the solution to the problem of a piston like source acting on a semi-infinite medium will be given in Chapter II.

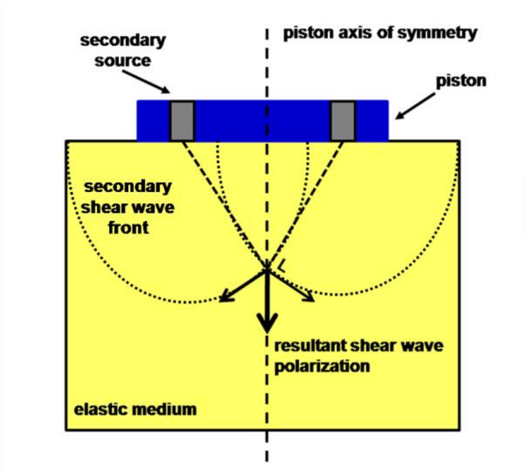

Fig. 1.5 Schematic representation of diffraction effects present in 1D transient elastography experiment. The summed contributions of transversely polarized shear waves coming from secondary sources give rise to a globally longitudinally polarized shear wave on the piston axis.

One dimensional transient elastography in its present form (Fig. 1.4(a)) suffers from an important drawback: because it worked in transmit mode it is necessary to access both sides of the medium under investigation. In 2002 *Sandrin et al.* [15] proposed an improved system in which the pulsed low frequency vibration is given by the ultrasonic transducer itself. This method relies on a probe that associates the vibrator and the transducer, which is built on the axis of the vibrator. The low frequency shear wave is driven by the transducer itself acting as a piston while it is used simultaneously in pulse echo mode to acquire the radio frequency ultrasonic data.

This improved setup is the basis of the Fibroscan developed by the company Echosens (*www.echosens.com*) founded in 2001 as a startup company linked to the Laboratoire Ondes et Acoustique. The Fibroscan is designed to characterize the fibrotic state of the liver relating its mean elasticity to a global hepatic score. In this specific case 1D transient elastography is able, in certain cases, to replace biopsy. One dimensional transient elastography has also been applied to determine non-invasively the mechanical parameters of other types of living tissue such as skin [20] or muscle [21]. In particular, in the Laboratorio de Acústica Ultrasonora, several applications were developed, like monitoring heat induced changes in muscle [22] or meet tenderness evaluation [23]. However, its feasibility to quantify the elasticity of thin layered soft tissue still presents its difficulties. This problem is the core of Chapter II.

1.2.2 Magnetic Resonance Elastography (MRE)

Magnetic Resonance Elastography was initiated by Dr. Raja Muthupillai and colleagues at Mayo Clinic (Rochester, Minnesota) in 1995 [24]. A schematic representation of the experimental setup used for this technique is presented in Fig. 1.6(a). The shear waves are induced, as in the case of 1D transient elastography, by positioning an external vibrator in contact with the patient and by driving it to generate a continuous vibration. The vibrator excitation frequency lies between 50 Hz to 1000 Hz depending on the size and the type of organ to be imaged. A specially designed nuclear magnetic resonance sequence allows to measure in three dimensions the induced displacement field. In Fig. 1.6(b) the acquired displacement field on a tissue mimicking gel containing two different cylindrical inclusions is presented. Each inclusion is marked with a dotted white line. The cylinder on the left is stiffer than the surrounding gel resulting in a larger wavelength. Contrary, a shorter wavelength in the softer cylinder on the right is observed. Finally, by locally inverting the wave equation (Eq. 1.5), a quantitative shear modulus image is obtained (Fig. 1.6(c)).

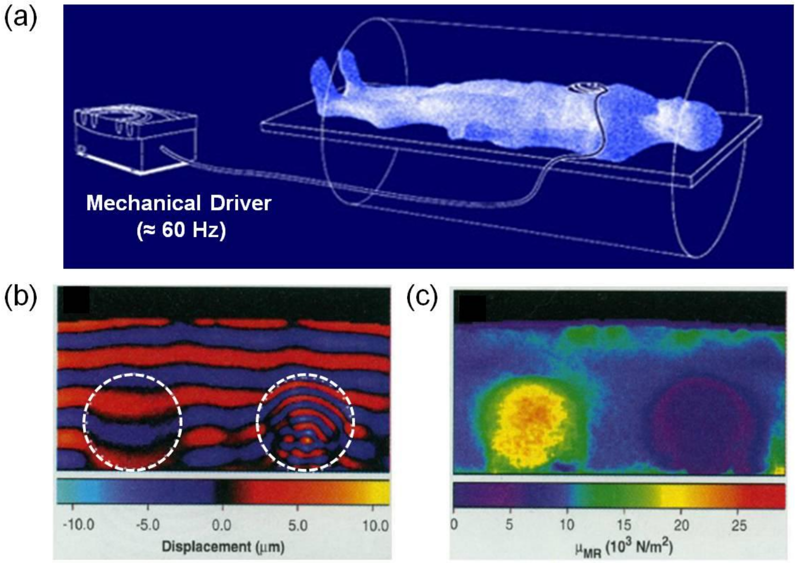

Fig. 1.6 (a) Schematic representation of experimental setup used in MRE. (b) Acquired displacement field on a tissue-simulating gel containing two different cylindrical inclusions with different stiffness. Each inclusion is marked with dotted line. The cylinder on the left is stiffer than the surrounding gel resulting in a larger wavelength. Contrary, a shorter wavelength in the softer cylinder on the right is observed. (c) Quantitative shear modulus map computed from the local wavelength of the displacement image. **Source:** ***Muthupillai et al.*** **[24]**

The strength of MRE lies in its high resolution elasticity images (typically 2x2x2 mm^3) however the prize to pay is a high acquisition time (~ 10 minutes) which doesn't allow real time elasticity imaging. Another drawback is its high cost, which prevents from realizing systematic studies, e.g. for cancer detection. However, MRE has been successfully applied to the elasticity imaging of breast, liver, brain and muscle [25]-[28].

1.2.3 Acoustic radiation force based imaging methods

Another way to induce shear waves, other than by using a mechanical vibrator, consists in using the radiation force of a focused ultrasonic beam. This idea was proposed by Armen Sarvazyan and colleagues in 1998 [5]. By focusing an ultrasonic beam in the tissue using an array of transducers or a single focalized transducer, a localized force in the focal spot and oriented along the ultrasonic beam axis can be created. That force is due to the momentum transfer from the ultrasonic wave to the medium caused by nonlinearities, dissipation and reflection effects. For an homogeneous medium, the volumic force F (in N/m^3) depends on the amplitude absorption coefficient of the pressure wave α (in Np/m), on the acoustic intensity I (in W/m^2), and on the speed of the pressure wave c_L as [29]:

$$F = 2\alpha I/c_L \tag{1.12}$$

The radiation force described in Eq. 1.12 is highly localized and directional, its main axis being in the direction of propagation of the ultrasonic beam. The force components in the other directions are at least one order of magnitude smaller [5]. Thus for the case of a focused transducer, the radiation force is usually negligible outside of the focal zone.

As a result of this remote force, an axial displacement of the tissue of some tens of microns at several centimeters depth is achieved. Once the ultrasonic burst ends (typical burst duration 100 μs), the displaced tissue comes back to its equilibrium resulting in the generation of a shear wave. Several elastographic techniques use acoustic radiation force for retrieving the elastic properties of tissue. In what follows three of them will be presented: acoustic radiation force impulse (ARFI) imaging, ultrasound stimulated vibro-acoustography (USVA) and Supersonic Shear Imaging (SSI).

- Acoustic Radiation Force Impulse (ARFI) imaging

ARFI was developed by Kathryn Nightingale and collaborators in 2001 at Duke University (Durham, North Carolina) [17]. A transducer array is used to generate the acoustic radiation force. ARFI technique consists in measuring, through a speckle interferometry technique, the movement of the tissue at the focal spot during and after the application of the radiation force. Two different times that are related to the local viscosity and elasticity of the tissue at the focal spot are measured (Fig. 1.7(a)). The "time to peak" is the time taken by the tissue to achieve its maximum displacement. The "recovery time" is the time needed for the tissue to recover equilibrium. ARFI estimates both times as well as the maximum displacement amplitude.

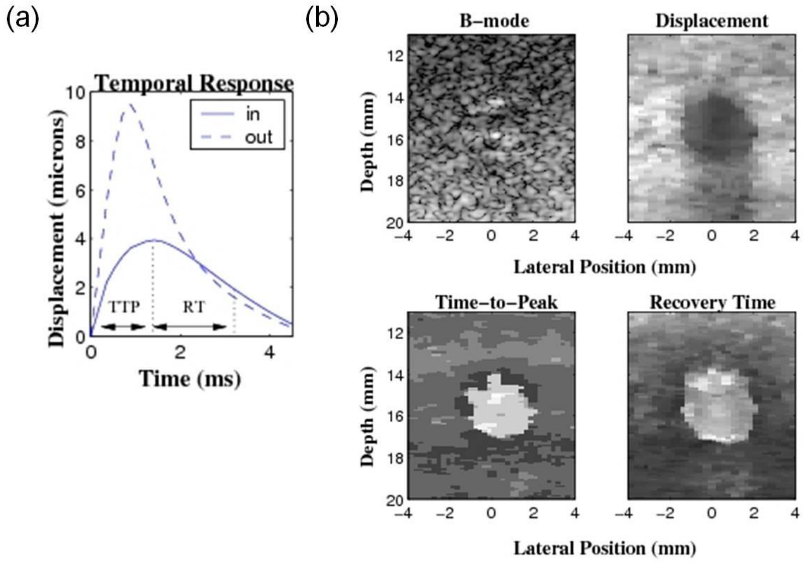

Fig 1.7 (a) Measured magnitudes in ARFI: the maximum displacement amplitude, "time to peak" (TTP) and the "recovery time" (RT). (b) Parametric ARFI images obtained for a gelatin-based tissue mimicking phantom containing a spherical inclusion. ARFI maximum displacement amplitude, time-to-peak, and recovery time images clearly delineate the inclusion. **Source:** ***kathynightingalelab.pratt.duke.edu***

A complete image of the entire medium is obtained by steering the focal spot to different locations. Parametric ARFI images obtained for a gelatin-based tissue mimicking phantom containing a spherical inclusion are presented in Fig. 1.7(b). The inclusion is not ultrasonically-visible in the B-mode image. However, ARFI maximum displacement amplitude, time-to-peak, and recovery time images clearly delineate the inclusion due to its mechanical contrast from the background material.

The main drawback of the ARFI technique lies in retrieving the shear modulus from the above mentioned parameters. In order to solve the inverse problem other parameters have to be taken into account, e.g. the beam and object geometry. As a consequence ARFI technique results in a qualitatively way to estimate the tissue Young's modulus.

Nowadays, at Nightingale's laboratory, attention is focused in measuring the shear waves that propagate away from the focal spot as the radiation force ceased. This improved ARFI technique has the advantage of being quantitative. Recently this technique was successfully applied in measuring the elastic properties *in vivo* in the human liver [30].

- Ultrasound Stimulated Vibro-Acoustography (USVA)

Another imaging modality that uses the acoustic response of an object to a highly localized dynamic radiation force is ultrasound stimulated vibro-acoustography (USVA). This technique was developed in 1998 by Mostafa Fatemi and James F. Greenleaf [31]. In Fig. 1.8(a) the experimental setup used in his work is presented.

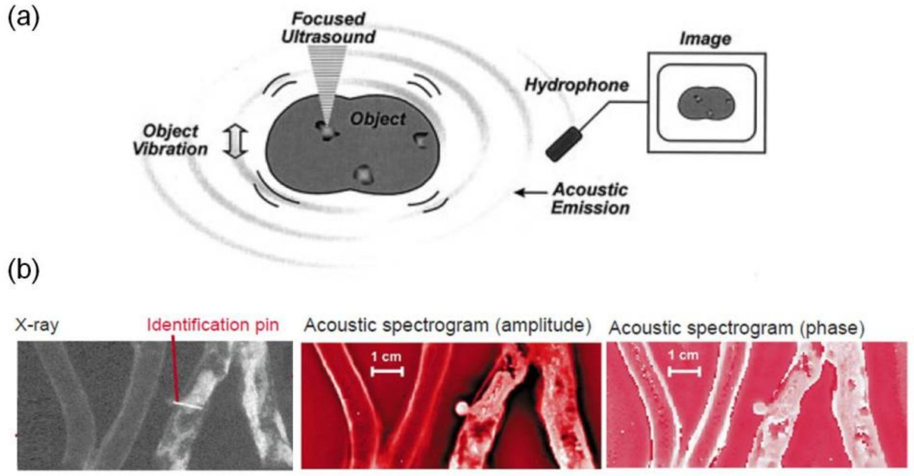

Fig. 1.8 (a) Experimental setup for USVA. (b) Vibro-acoustic images of excised human arteries. On the left the X-ray image of a normal (left) and calcified (right) artery is presented. Bright areas indicates calcifications. On the amplitude and phase images of the acoustic spectrogram the calcifications are clearly visible. **Source: *Fatemi et al.* [31], [32].**

The radiation force is generated by a two-element confocal transducer consisting of a center disc and an outer ring. Each element is driven by two continuous wave sources at frequencies equal to ω_1 and $\omega_2 = \omega_1 + \Delta\omega$. These frequencies are very close to the central frequency of each element, however $\Delta\omega$ is much smaller, corresponding to the kHz range. The ultrasound beams of each element will interact only in a small region around the focal spot, generating a radiation force which oscillates at the difference frequency $\Delta\omega$. In response, a portion of the object vibrates sinusoidally in a pattern determined by its viscoelastic properties. The acoustic emission resulting from the object vibrations is then received by an hydrophone. The amplitude and phase are used to generate an image that represents the ultrasonic and low-frequency (kHz range) mechanical characteristics of the object. In Fig. 1.8(b) the phase and amplitude of the acoustic emission from calcified and non calcified iliac human arteries are presented and compared to an X-Ray image. Calcifications are clearly visible producing distinctive amplitude and phase values.

The main drawback of USVA is its difficulty to retrieve the tissue Young's modulus in a quantitative way. The acoustic emission depends on the tissue hardness, but other parameters also play an important role, e.g. the acoustic radiation force amplitude or the geometry of the object. Thus, the obtained images correspond to a mixture of multiple physical parameters. However, due to its high spatial resolution USVA has proven to be an efficient and useful technique in imaging breast and prostate tissue [33]. Recently this technique was implemented in a standard ultrasound scanner [34].

Nowadays, at Greenleaf's laboratory, attention is focused on the shear waves travelling away from the focal spot. The approach was termed "Shear Dispersion Ultrasound Vibrometry" (SDUV) [35] and consists in extracting the shear wave dispersion curve (phase velocity as a function of frequency). The confocal transducer is used as a remote shear wave source at a given $\Delta\omega$ frequency. Then by varying the frequency difference and measuring the shear wave speed the dispersion curve is obtained. From the dispersion curve it is possible to extract the visco-elastic properties of the tissue.

- Supersonic Shear Imaging (SSI) technique

The SSI technique was developed in 2004 at the Laboratoire Ondes Acoustique (present Institut Langevin) by *J. Bercoff et al.* [18]. For the SSI technique the acoustic radiation force produced by an ultrasonic array is used to generate the shear wave. Then its propagation is tracked as it travels away from the source in the direction perpendicular to the ultrasonic beam. The main problem is that the amplitude of a single radiated shear wave decreases rapidly with distance. Thus, in order to increase the area sensed by the shear wave, a cylindrical shear wave is generated by focusing the ultrasonic beam at different focal depths. This is achieved by changing the electronic delays between the transmitted signals of each transducer element. The procedure is illustrated in Fig. 1.9(a). If the shear wave source moves faster than the radiated shear waves, constructive interference along a Mach cone will result in a high-displacement cylindrical shear wave that propagates over relatively long distances. The experimental Mach cone is presented in Fig. 1.9(b).

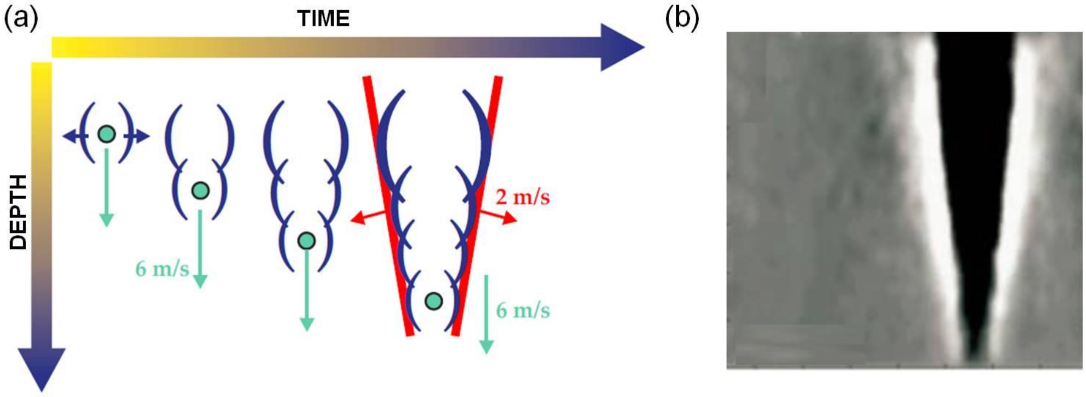

Fig. 1.9 (a) Generation of the Mach cone by focusing ultrasound at different depths. (b) Experimental Mach cone in a gelatin based phantom. **Source:** ***Bercoff et al.*** **[18]**

After the pushing sequence finishes, an ultrafast imaging sequence begins by sending plane-wave insonifications at a high-frame rate (up to 20 kHz) in order to track the shear wave propagation. The displacement movie is then recovered by using an acoustical speckle tracking technique for successive radio frequency data images. Three frames of the displacement movie on a tissue mimicking phantom containing a 20 mm diameter stiff cylindrical inclusion are presented in Fig. 1.10. It can be observed how the shear wave accelerates while passing through the inclusion (t = 12 ms) resulting in a distorted wave front.

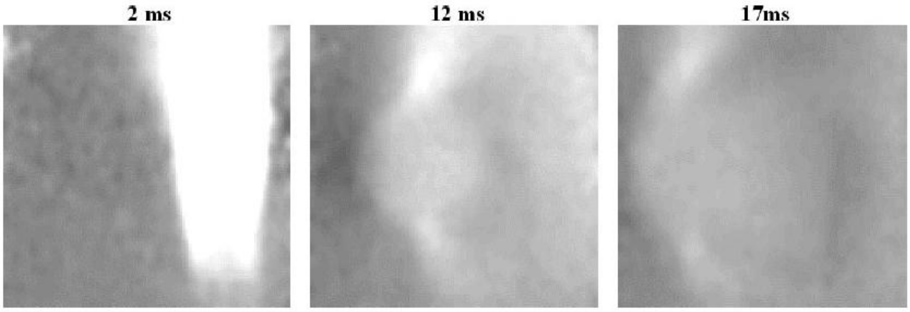

Fig. 1.10 Three frames of the displacement movie of the shear wave propagation in a tissue mimicking phantom containing a 20 mm diameter stiffer inclusion. Evidently, the shear wave is sensitive to the material's Young modulus as it accelerates while passing through the inclusion. **Source:** ***Bercoff et al.*** **[18]**

Finally, by locally inverting the wave equation (Eq. 1.5) [18] or by locally measuring the shear wave time of flight [36] a quantitative elasticity image is obtained. In Fig. 1.11(a) the obtained result for the displacement movie in Fig. 1.10 is presented. The inclusion is clearly visible with a high spatial resolution in the elasticity image. Recently the SSI technique has been successfully applied to determine non-invasively the mechanical parameters of living tissue such as breast [37], liver [38] or muscle [39].

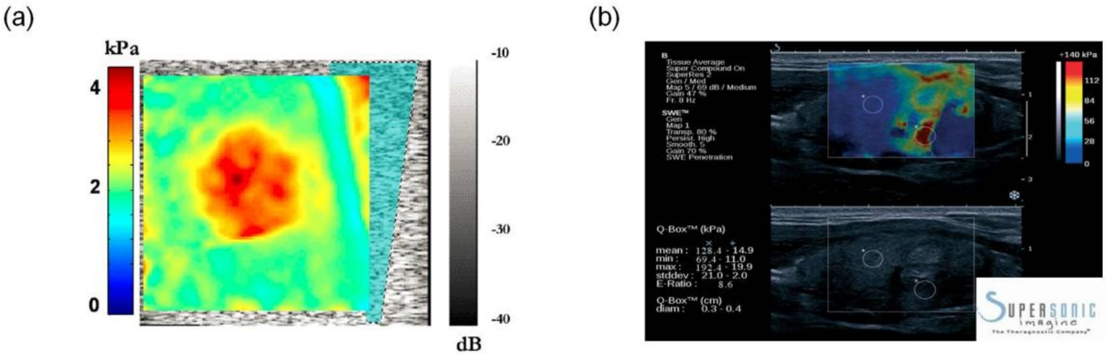

B
Tissue Average
Super Compound On
SuperRes 2
Gen / Med
Map 5 / 69 dB / Medium
Gain 47 %
Fr. 8 Hz

SWE™
Gen
Map 1
Transp. 80 %
Persist. High
Smooth. 5
Gain 70 %
SWE Penetration

Q-Box™ (kPa)
mean : 128.4 - 14.9
min : 69.4 - 11.0
max : 192.4 - 19.9
stddev : 21.0 - 2.0
E-Ratio : 8.6

Q-Box™ (cm)
diam : 0.3 - 0.4

Fig. 1.11 (a) Quantitative elasticity image obtained from the displacement movie in Fig. 1.9 superimposed to the B-mode image. **Source:** ***Bercoff et al.*** **[18]** (b) Aixplorer's elasticity and echographic image. **Source:** ***supersonicimagine.fr***

The SSI technique is the basis of the Aixplorer ultrasound scanner developed by the company Supersonic Imagine (*www.supersonicimagine.fr*) founded in 2005 as a startup company linked to the Laboratoire Ondes et Acoustique. Nowadays, the Aixplorer is the only ultrasound scanner in the market able to quantitatively image elasticity in real time in an operator-independent way (Fig. 1.11(b)).

1.2.4 Towards passive elasticity imaging

In the previous sections in a non exhaustive list, several Active Dynamic Elastography techniques were presented. However as stated above, there is a "new-born" type of Dynamic Elastography which does not induce the shear wave into the tissue, instead it takes advantage of the shear waves naturally present in the human body due heartbeats, breathing and muscular activity to conduct an elastography experiment. This recent type of Dynamic Elastography technique is termed Passive Elastography.

The pioneering work in this field was done by *Sabra et al.* in 2007 [9]. In his work he measured *in vivo* the global visco-elastic properties of skeletal muscle by using the noise naturally present in such tissue. For the experiment, sixteen miniature accelerometers were skin mounted along the vastus lateralis muscle providing the surface displacement field. By applying correlation techniques to the recorded displacement field, the shear wave dispersion curve was extracted. Finally by fitting a Voigt model the tissue's global viscosity and elasticity were retrieved.

In the work of *Gallichan et al.* in 2009 [40] a "quasi" passive elastography experiment is performed by using a nuclear magnetic resonance scanner. In his work the diffuse elastic field created by the vibrations of the patient table that result from low-frequency switching of the imaging gradients were utilized to image the elasticity of a gelatin phantom with stiff cylindrical gelatin inclusions and brain.

From the encouraging results obtained in the works of *Sabra et al.* and *Gallichan et al.*, passive elastography is making its first steps as an alternative elastography imaging modality. However, there is still a long way to travel in order to establish passive elastography as a consolidated imaging modality.

1.3: Conclusions

Elasticity imaging is an always developing research area with direct implications into medical imaging and diagnosis. This is reflected in the multiple commercial applications developed within the past ten years. In Static Elastography a strain image is obtained, however due to the lack of information on the stress to which the tissue is submitted this method does not provide a quantitative elasticity estimation. To overcome this limitation a set of techniques based on shear wave propagation inside the tissue have been developed during the past decade: Dynamic Elastography. Due to the use of shear waves whose speed is related to the tissue elasticity, the dynamic approach has the advantage of being quantitative. Dynamic elastography techniques can be subdivided in two groups: active and passive elastography techniques.

Starting in 1994, with the work of *Catheline et al.* [14], active elastography has shown to be an always growing research area. Countless techniques, applications and devices were developed during the last twenty years. In this Chapter, in a non exhaustive list, several active elastography techniques were presented. Although all the presented techniques are based on the same common concept, which are shear waves, the physics underneath each technique is different. This has direct implications on the inverse problem solution. An example of this situation will be presented in the following Chapter when measuring the elasticity of thin layered soft tissue with the SSI technique and 1D transient elastography.

Contrary to active elastography, passive elastography is a new developing research area, which is making its first steps as a new elastography modality. In this thesis, a step forward is taken towards passive elasticity imaging. A method for extracting the elasticity of soft tissues from a complex reverberated elastic field using spatiotemporal correlations interpreted in the frame of the time-reversal symmetry was developed. This approach is baptized Time Reversal Elastography. In Chapter III the feasibility of Time Reversal Elastography as a passive quantitative elasticity imaging technique is demonstrated, first in vitro in bi-layer heterogeneous tissue mimicking phantoms, and then *in vivo* in the belly muscle and liver. In Chapter IV a novel technique inspired in the acoustical inverse filter was developed: the passive inverse filter. This technique posses some advantages when compared to Time Reversal Elastography: it corrects for the anisotropy of the passive source distribution and the frequency of the time reversed field is completely controlled. As a result better resolved images are obtained. In Chapter V the frequency control through the passive inverse filter is exploited to extract the shear wave dispersion curve *in vivo* in the belly muscle and liver.

Chapter II

Shear modulus assessment of thin layered soft solids: comparison between 1D Transient Elastography and Supersonic Shear Imaging technique

On the preceding Chapter several dynamic elastography techniques were presented, in particular the 1D transient elastography technique and the SSI technique. Both techniques have been successfully applied to determine non-invasively the mechanical parameters of living tissue such as breast [37], liver [38], [41] or muscle [21], [39]. Recently elasticity estimation of thin layered soft tissues has gained increasing interest propelled by several medical applications. For example arterial elasticity assessment has gained importance as an independent predictor of cardiovascular diseases and mortality [42], [43]. Another example lies in dermatology where the severity of many skin diseases (e.g., scleroderma, Ehlers-Danlos, keloids), which induce alterations of the mechanical properties of the skin, could be assessed by measuring the skin elastic properties.

The feasibility of the SSI technique to viscoelastic assessment of thin soft tissues has been demonstrated in cornea [44] and the arterial wall [45]. In these specific cases, the wavelength of the propagating wave is of the order of the cornea/arterial wall thickness leading to a propagation which is related to the “leaky” Lamb wave theory of guided waves. The bulk shear wave speed and thus the shear elasticity are retrieved from the Lamb wave dispersion curve using a specific model [45], [46].

Regarding 1D transient elastography, its feasibility to quantify the elasticity of thin layered soft tissue remains a challenge. In the work of *Gennisson et al.* [20] 1D transient elastography was applied to skin by using a monochromatic mechanical excitation. A good resolution was reached with this method, however the elasticity measurements turned out to be overvalued. On a previous work [47], it was possible to extract the shear modulus of one arterial phantom (fixed shear modulus and thickness) by applying 1D transient elastography using as mechanical excitation a 150 Hz central frequency impulsion. However, in order to verify the feasibility of 1D transient elastography for a wide range of experimental conditions, further studies needed to be carried out. In the present Chapter such study is proposed, validating the use 1D transient elastography for the quantitative elasticity assessment of thin layered soft tissues. The results presented in this Chapter were published in the article entitled "Application of 1D transient elastography for the shear modulus assessment of thin layered soft tissue: comparison with

Supersonic Shear Imaging technique" in *IEEE Transactions on Ultrasonics Ferroelectrics and Frequency Control*, volume 59, number 4 on April 2012 [48].

Firstly, 1D transient elastography experiments were simulated by finite difference simulation in plates with exactly known thickness and elasticity for a wide range of excitation frequencies (100 - 400 Hz). Secondly, 1D transient elastography experiments on three different phantoms with different elasticities and layer thicknesses were performed, also for a wide range of excitation frequencies. The experimental dispersion curves were compared to the ones obtained by 1D transient elastography finite difference simulation. Moreover, to complete the validation process, the SSI technique (considered as a gold standard) was applied on each sample. For this case, the propagating wave is guided as Lamb wave. In previous works [45], [46] the Lamb wave model used to retrieve the shear modulus of thin tissue layers takes into account that the tissue layer is surrounded by an insviscuid fluid. In this Chapter a more general Lamb model is proposed since the plates under study were surrounded by an elastic medium. Experimental dispersion curves were compared with the ones obtained by finite difference simulation and fitted by numerically solving the generalized Lamb model. This allows the retrieval of the bulk shear wave speed for each layer.

Finally, the results obtained by 1D transient elastography and SSI are discussed, compared and shown to be in good agreement, although the physics on the wave generation and propagation for each technique is different. While for the SSI the generated wave is guided along the plate, no guidance effect will be observed for 1D transient elastography. This difference in the inverse problem for each technique can be attributed to the type of shear wave generated and thus used by each technique. In order to further clarify this point, a detailed description of the physics underneath each technique will be presented in the next section.

2.1: The physics on the wave propagation and generation for 1D transient elastography and SSI techniques

The shear wave used in the 1D transient elastography and the SSI techniques is generated by applying an impulsional force on the tissue, either from its surface using a mechanical vibrator (1D transient elastography) or in its volume using the radiation force of a focalized ultrasonic beam (SSI). Thus in order to better understand the displacement field created by this type of source the elastodynamic Green's function will be introduced.

The elastodynamic Green's function $\vec{G}_i$ is defined as the solution to the wave equation (Eq. 1.5) for an infinite medium given an impulsional point source $\vec{F}_i$ oriented along a given direction $\vec{x}_i$:

$$(\lambda + 2\mu)\nabla\left(\nabla.\vec{G_i}\right) + \mu\nabla \times \left(\nabla \times \vec{G_i}\right) + \vec{F_i} = \rho\ddot{\vec{G_i}} \tag{2.1}$$

with

$$\vec{F_i}(\vec{r}, t) = \delta(\vec{r})\delta(t).\vec{x}_i \tag{2.2}$$

For solving Eq. 2.1 the force $\vec{F_i}$ is defined as acting at the center of a Cartesian coordinate system at time zero. Based on [49] the $\vec{x}_j$ component of the Green function is given by:

$$G_{ij}(\vec{r}, t) = \frac{1}{4\pi\rho}\left\{\frac{\gamma_i\gamma_j}{rc_L^2}\delta\left(t - \frac{r}{c_L}\right) + \frac{\delta_{ij} - \gamma_i\gamma_j}{rc_T^2}\delta\left(t - \frac{r}{c_T}\right) + \frac{3\gamma_i\gamma_j - \delta_{ij}}{r^3}\int_{r/c_L}^{r/c_T} \tau\delta(t - \tau)d\tau\right\} \tag{2.3}$$

with

$$\begin{cases} r = |\vec{r}| \\ \gamma_i = \frac{x_i}{r} = cos(\vec{r}, \vec{x}_i) \end{cases} \tag{2.4}$$

The Green's function presented in Eq. 2.3 is composed of three terms corresponding to a compressional wave, a shear wave and a coupling term between both waves. The first two terms of Eq. 2.3 are classical far-field terms with an amplitude decay of $1/r$. The direction of particle motion of the first term is parallel to the direction of wave propagation, while for the second term those directions are normal to each other [49]. Thus, each term represent a longitudinal and a transversal wave respectively. Their contributions occur respectively at times $t_L = r/c_L$ and $t_S = r/c_T$. The third term in Eq. 2.3 is a mixture of longitudinally and transversally polarized waves, resulting in a coupling term between both purely transverse and purely longitudinal waves. Its amplitude being proportional to t/r^3, with $r/c_L < t < r/c_T$, which results in an amplitude decay of $1/r^2$ [49]. Due to its fast attenuation with distance from the source, this term is usually named as near-field term.

For the 1D transient elastography and the SSI technique the component along the ultrasonic beam axis (z-component) of the induced displacement field is acquired by means of an ultrasonic speckle interferometry technique. On the other hand, the force will be usually applied along the z-direction. As a consequence, attention will be focused in the Green's function component $G_{zz}(\vec{r}, t)$:

$$G_{zz}(\vec{r}, t) = \frac{1}{4\pi\rho}\left\{\frac{\cos^2\theta}{r.c_L^2}\delta\left(t - \frac{r}{c_L}\right) + \frac{\sin^2\theta}{r.c_T^2}\delta\left(t - \frac{r}{c_T}\right) - \frac{3\cos^2\theta - 1}{r^3}\int_{r/c_L}^{r/c_T} \tau\delta(t - \tau)d\tau\right\} \tag{2.5}$$

Where θ denotes the angle between the force axis (z-axis) and the observation point. From Eq. 2.5, in the far field the compressional wave is maximal along the force axis ($\theta = 0; \pi$) and zero along the perpendicular axis. Contrary, the shear wave amplitude is zero along z-axis and maximal in the perpendicular direction ($\theta = -\pi/2; \pi/2$). However, at the shear wave arrival time, the near field wave is maximal on the force's axis resulting in a non negligible displacement field in all directions for the shear wave. Thus there are two shear waves of different physical nature that can be tracked in order to estimate the tissue's elasticity. The first shear wave, which propagates perpendicularly to the direction of the applied force, corresponds to the far field term. The second shear wave corresponds to the near field term and propagates parallel to the direction of the applied force. Each type of wave is respectively exploited by the SSI technique and the 1D transient elastography technique as it will be shown below.

2.1.1 Green's function for 1D transient elastography: Lamb's problem

For the 1D transient elastography technique, a piston like source attached to a mechanical vibrator acts on the phantom's surface generating shear waves inside the sample. An approximate solution to this problem can be found from the Green's function for an infinite elastic medium (Eq. 2.5) by using the Method of Images. The free surface acts as a mirror and yields a secondary image source of the original source by a mirror symmetry through the free surface. For 1D transient elastography the original source is located on the interface, thus the secondary source coincides with the original one. As a consequence, the approximate Green's function to the problem $\tilde{G}_{zz}^{o}$ is obtained by multiplying the infinite medium Green's function by a factor 2. Thus, based on Eq. 2.5, in a 1D transient elastography experiment, two types of waves with different arrival times and amplitudes will be observed: a compressional and a shear wave. Since the displacement field is acquired on the piston axis, according to the source's directivity pattern (Eq. 2.5) the far field term, corresponding to a pure shear wave is negligible, thus the shear wave used in 1D transient elastography will corresponds to the one present in the coupling term.

An exact solution to the problem of a piston like source acting on semi-infinite elastic medium (Lamb's problem) was already given by *Gakenheimer and Miklowitz* [50] for a Heaviside time dependent point force. Thus to obtain the exact Green's function G_{zz}^{o} for this problem, which is the response for a delta excitation along the axis of the punctual force, the solution obtained by *Gakenheimer and Miklowitz* should be time differentiated. The difference between the exact solution G_{zz}^{o} and the approximate solution $\tilde{G}_{zz}^{o}$ is that the exact solution takes into account the presence of surface waves along the free surface.

Since the experimental displacement field is obtained through a radio frequency data cross-correlation process for successive acquisitions, the measured seismograms correspond to the particle velocity. Thus, to compare experimental and theoretical results the time derivative of the Green’s function has to be calculated. Finally, the on axis displacement field at fixed depth z is obtained from the convolution between the time derivative of Green’s function and the time excitation of the force $F(t)$. For a monochromatic sinusoidal excitation of angular frequency ω the following approximated expression for the particle velocity at a given depth, valid for the soft solid case, is obtained [14]:

$$\begin{aligned} V_z(z,t) &= \frac{\partial G_{zz}^{o}}{\partial t} \otimes F(t) = \\ &= \frac{c_L}{2\pi.\mu.z^2\gamma^2}\left\{\omega.t_L.\cos(\omega.(t-t_L)) - 2\gamma\sin(\omega.(t-t_T)) + \frac{2\gamma}{\omega.t_T}\left[\cos(\omega.(t-t_T)) - \cos(\omega.(t-t_L))\right]\right\} \end{aligned} \tag{2.6}$$

Where c_L is the compressional wave speed, t_L and t_S are the arrival time for the compressional and shear wave respectively and γ is the ratio between c_L and c_T. From Eq. 2.6 it is important to point out that, for high frequencies the first term dominates, thus the most part of the energy propagate as a compressional wave. For very low frequencies the last term dominates, which represents the coupling term (a mixture of a shear wave and a compressional wave). Finally, between those two extremes the middle term dominates, which corresponds to a shear wave. In the frequency range of the 1D transient elastography experiments (100 – 400 Hz) even though the shear wave dominates the coupling term cannot be neglected. As a result the presence of both, a compressional and a longitudinal component of the shear wave corresponding to the near field term will be observed in the experimental displacement field.

2.1.2 Shear wave propagation for the SSI technique

As presented in Chapter I, for the SSI technique the acoustic radiation force produced by an ultrasonic array is used as a remote source. The medium's response to such force is described by the Green's function for an infinite, elastic, isotropic medium (Eq. 2.5). As predicted by Eq. 2.5 pure shear waves will propagate away from the source in the direction perpendicular to force's axis. Those shear waves, which corresponds to the far field term of the elastodynamic Green's function, are used by the SSI technique to estimate the medium's elasticity.

Thus, while in the SSI technique the tracked shear wave corresponds to the far field component of the elastodynamic Green's function, in 1D transient elastography the measured shear wave corresponds to the Green's function near field term. The different nature of the shear wave involved in each technique will have direct implications on the inverse problem solution. As it was mentioned above, for the SSI technique the generated wave is guided as a Lamb wave along the plate due to the successive reflections on the plate boundaries. Thus, the relationship between shear wave speed and elasticity is more complex [46] than in the case of an infinite elastic isotropic soft solid, as it will be described below.

2.2: Wave propagation in soft solid plates

As mentioned above, for the SSI technique, in the case of thin layered soft tissues, the wave propagation is guided along the plate due to the successive reflections on the plate boundaries, resulting in a more complex relation between shear wave speed and elasticity. In previous works a Lamb wave model was used to retrieve the shear modulus of arteries [45], [51] and thin tissue layers submerged in water [46]. The Lamb model used in these works takes into account that the artery/thin tissue layer is surrounded by an insviscuid fluid: "leaky" Lamb wave model. The influence of the surrounding medium being not fluid was qualitatively studied in [45] using numerical simulation but was not taken into the model. In the experiments presented in this Chapter, the thin plate is embedded in an elastic medium, so a generalized Lamb model is needed, which takes this effect into account. Each phantom was considered as a three layered structure. Multilayered structures have been widely studied in non-destructive evaluation [52] and seismology [53]. The generalized Lamb wave model is achieved by adapting the global matrix technique for modelling elastic waves in multilayered media developed by M. J. S. Lowe [52], [54] for the simple case of an isotropic elastic plate embedded in an elastic infinite medium.

The global matrix method is based on the fact that the field equations for the displacements and stresses in a flat isotropic elastic plate can be written as the superposition of the fields corresponding to four bulk waves within the plate. In Fig. 2.1 the case for a single layer embedded in an elastic medium is presented. Inside the plate there are four waves, two shear waves ($S^{\pm}$) and two longitudinal waves ($L^{\pm}$), propagating with positive (S^{+},L^{+}) and negative (S^{-},L^{-}) x_1 component. These four waves create two kinds of waves (one shear and one compressional wave) in the surrounding medium.

The first step of the method consists in deriving the field equations for bulk waves, which are solutions to the wave equation in an infinite medium. As a result the stresses and displacements within the plate can be expressed in terms of the amplitudes of all the bulk waves that can exist within that plate. Then by introducing the boundary conditions at each interface the rules for coupling between layers and for the superposition of the bulk waves are defined. The stresses and displacements at the boundaries of each layer can be combined with the boundary conditions to describe the entire system in one large global matrix that relates the bulk wave amplitudes to the physical constraints.

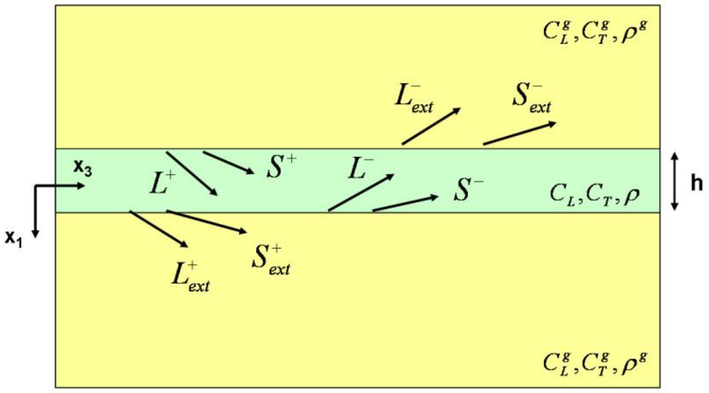

Fig. 2.1 Sample geometry used for the Lamb wave theory. In each layer the partial waves ($L^{\pm}$, $S^{\pm}$) that combined to generate the guided wave are presented. The longitudinal/shear wave speeds and the medium density are respectively c_L, c_T, ρ for the plate and c_L^g, c_T^g, ρ^g for the surrounding medium.

2.2.1 Field equations for plane waves in two dimensions

In what follows it will be assumed that the wavelengths involved are smaller than the width of the plate and therefore a plane strain analysis is valid. The coordinate system may then be reduced to the plane defined by the wave propagation direction and the normal to the plate. In Fig. 2.1 the coordinate system which will be used for the plate is presented. For plane strain there is no variation of any quantity in the x_2 direction. As a consequence the model is restricted to waves whose particle motion is entirely in the plane thus excluding for example Love modes.

A convenient way of presenting the solutions in a vector form, as presented in section 1.1, is by introducing Helmholtz potentials, in which longitudinal waves (L) are described by a scalar function ϕ and shear waves (S) by a vector function $\vec{\psi}$ whose direction is normal to the wave propagation direction and the particle motion direction.

$$\phi = -iA_L e^{i(\vec{k}.\vec{x}-\omega t)} \tag{2.7}$$

$$\vec{\psi} = -iA_S e^{i(\vec{k}.\vec{x}-\omega t)} \hat{x}_2 \tag{2.8}$$

Here A_L and A_S are the longitudinal and shear wave amplitudes, $\vec{k}$ is the wavenumber vector and ω is the angular frequency. From the potentials, the displacements of the longitudinal and shear waves can be calculated as:

$$\vec{u}_L = \nabla\phi = \begin{pmatrix} k_1 \\ 0 \\ k_3 \end{pmatrix} A_L e^{i(\vec{k}.\vec{x}-\omega t)} \tag{2.9}$$

$$\vec{u}_S = \nabla \times \vec{\psi} = \begin{pmatrix} -k_3 \\ 0 \\ k_1 \end{pmatrix} A_S e^{i(\vec{k}.\vec{x}-\omega t)} \tag{2.10}$$

2.2.2 Superposition of plane waves in an isotropic elastic plate

As stated above, the development of a model for wave motion in plates is achieved by the superposition of longitudinal and shear bulk waves and the imposition of boundary conditions at the interfaces between the layers. For modelling the Lamb wave propagating along the plate it is sufficient to assume the presence of four bulk partial waves in the plate: two shear waves ($S^{\pm}$) and two longitudinal waves ($L^{\pm}$), propagating with positive (S^{+},L^{+}) and negative (S^{-},L^{-}) x_1 component. This situation is schematized in Fig. 2.1.

Let k_3 be denoted by k, which corresponds to the Lamb wavenumber. Then, the k_1 components of the partial wave wavenumber vector can be expressed in terms of the Lamb wavenumber and the bulk wave velocities of the plate as:

$$k_i = \pm\sqrt{\frac{\omega^2}{c_i^2} - k^2} \tag{2.11}$$

In Eq. 2.11 the subscript $i = L, T$ stands for the longitudinal or shear partial wave, c denotes the bulk phase velocity of each type of wave for the plate and the $+$ and $-$ signs correspond to a wave moving with positive (“downward”) and negative (“upward”) x_1 component. It is important to notice that if ω^2/c_i^2 is greater than k^2 then k_i is real and the wave is homogeneous travelling at some nonzero angle with respect to the x_3 direction. On the other hand if ω^2/c_i^2 is less than k^2 then k_i is imaginary and the wave is inhomogeneous or evanescent propagating in the x_3 direction and decaying in the x_2 direction.

The displacements and stresses at any location inside the plate may be found from the amplitudes of the bulk waves using the field equations. In what follows the expressions for the two displacement components u_1 and u_3, the normal stress σ_{11} and the shear stress σ_{13} will be derived since for a plate system the quantities of interest are those which must be continuous at the interfaces. From Hooke's Law and the strain definition the stresses can be calculated as:

$$\sigma_{11} = \lambda\left(\frac{\partial u_1}{\partial x_1} + \frac{\partial u_2}{\partial x_3}\right) + 2\mu\frac{\partial u_1}{\partial x_1} \tag{2.12}$$

$$\sigma_{13} = \mu\left(\frac{\partial u_1}{\partial x_3} + \frac{\partial u_3}{\partial x_1}\right) \tag{2.13}$$

Thus for the longitudinal partial bulk waves it can be found:

$$u_1 = \pm k_L A_{L\pm} e^{\pm ik_L x_1}.\,e^{i(kx_3-\omega t)} \tag{2.14a}$$

$$u_3 = kA_{L\pm} e^{\pm ik_L x_1}.\,e^{i(kx_3-\omega t)} \tag{2.14b}$$

$$\sigma_{11} = i\alpha.\,A_{L\pm} e^{\pm ik_L x_1}.\,e^{i(kx_3-\omega t)} \tag{2.14c}$$

$$\sigma_{13} = \pm i\beta.\,k_L.\,A_{L\pm} e^{\pm ik_L x_1}.\,e^{i(kx_3-\omega t)} \tag{2.14d}$$

For the partial shear bulk waves:

$$u_1 = -k.\,A_{S\pm} e^{\pm ik_T x_1}.\,e^{i(kx_3-\omega t)} \tag{2.15a}$$

$$u_3 = \pm k_T A_{S\pm} e^{\pm ik_T x_1}.\,e^{i(kx_3-\omega t)} \tag{2.15b}$$

$$\sigma_{11} = \mp i\beta.\,k_T.\,A_{S\pm} e^{\pm ik_T x_1}.\,e^{i(kx_3-\omega t)} \tag{2.15c}$$

$$\sigma_{13} = i\alpha.\,A_{S\pm} e^{\pm ik_T x_1}.\,e^{i(kx_3-\omega t)} \tag{2.15d}$$

Where $\alpha = \rho(\omega^2 - 2c_T^2k^2) = \rho c_T^2(k_T^2 - k^2)$ and $\beta = 2\rho k c_T^2$, ρ the mediums density and $\omega = 2\pi f$, f being the wave frequency. The displacements and stresses at any location in the plate may therefore be found by summing the contributions due to the four partial wave components.

$$\begin{pmatrix} u_1 \\ u_3 \\ \sigma_{11} \\ \sigma_{13} \end{pmatrix} = \begin{pmatrix} k_L e^{ik_L x_1} & -k_L e^{-ik_L x_1} & -k e^{ik_T x_1} & -k e^{-ik_T x_1} \\ k e^{ik_L x_1} & k e^{-ik_L x_1} & k_T e^{ik_T x_1} & -k_T e^{-ik_T x_1} \\ i\alpha.\,e^{ik_L x_1} & i\alpha.\,e^{-ik_L x_1} & -i\beta.\,k_T.\,e^{ik_T x_1} & i\beta.\,k_T.\,e^{-ik_T x_1} \\ i\beta.\,k_L.\,e^{ik_L x_1} & -i\beta.\,k_L.\,e^{-ik_L x_1} & i\alpha.\,e^{ik_T x_1} & i\alpha.\,e^{-ik_T x_1} \end{pmatrix} . \begin{pmatrix} A_{L+} \\ A_{L-} \\ A_{S+} \\ A_{S-} \end{pmatrix} \tag{2.16}$$

The matrix in Eq. 2.16 describes the relationship between the wave amplitudes and the displacements and stresses at any position inside the plate. Its coefficients depend on the through-thickness position in the plate x_1, the material properties of the layer at this position (ρ,c_T,c_L), the frequency and the Lamb wavenumber k.

2.2.3 The Global Matrix method

Based on Eq. 2.16 it is possible to describe the boundary conditions for each interface of the plate. By combining all the different boundaries conditions at each interface it is possible to find a single global matrix $[G]$ which represents the entire system. This is the global matrix method [54]. The columns of the global matrix correspond to the amplitudes of the partial wave in each layer, where the surrounding medium is treated as two semi-infinite layers. Each row of the global matrix corresponds to one boundary condition: continuity of displacements and stresses along the interfaces of each layer. Thus by multiplying the global matrix by the partial wave amplitudes all boundary conditions will be simultaneously satisfied. The resulting equation will always be zero providing the characteristic equation of the system:

$$[G].\{A\} = 0 \tag{2.17}$$

where $[G]$ is the global matrix method and $\{A\}$ is the partial wave amplitude vector. Equation 2.17 is satisfied if the determinant of the global matrix is zero. The frequency and wavenumber values will determine whether this condition is met.

2.2.4 The generalized Lamb model: an elastic isotropic plate embedded in an elastic medium

For a plate embedded in an elastic medium eight partial waves should be taken into account: four for the plate and four for the surrounding medium. This situation is represented in Fig. 2.1. The four waves inside the plate create two kinds of waves in the surrounding medium: one shear and one longitudinal wave propagating with positive (L_{ext}^{+},S_{ext}^{+}) and negative (L_{ext}^{-},S_{ext}^{-}) x_1 component. As a consequence at each interface six partial waves should be taken into account. By applying the superposition principle and the continuity at each of the interfaces of the two displacement components u_1 and u_3, the normal stress σ_{11} and the shear stress σ_{13} the global matrix governing the system can be written as:

$$[G]=\begin{array}{cccccccc|l}
-k_L^g.F_L^g & -k.F_T^g & -k_L.F_L^* & k_L.F_L & k.F_T^* & k.F_T & 0 & 0 & \rightarrow u_1(-h/2) \\
k.F_L^g & -k_T^g.F_T^g & -k.F_L^* & -k.F_L & -k_T.F_T^* & k_T.F_T & 0 & 0 & \rightarrow u_3(-h/2) \\
i\alpha^g.F_L^g & i\beta^g.k_T^g.F_T^g & -i\alpha.F_L^* & -i\alpha.F_L & i\beta.k_T.F_T^* & -i\beta.k_T.F_T & 0 & 0 & \rightarrow \sigma_{11}(-h/2) \\
-i\beta^g.k_L^g.F_L^g & i\alpha^g.F_T^g & -i\beta.k_L.F_L^* & i\beta.k_L.F_L & -i\alpha.F_T^* & -i\alpha.F_T & 0 & 0 & \rightarrow \sigma_{13}(-h/2) \\
0 & 0 & k_L.F_L & -k_L.F_L^* & -k.F_T & -k.F_T^* & -k_L^g.F_L^g & k.F_T^g & \rightarrow u_1(h/2) \\
0 & 0 & k.F_L & k.F_L^* & -k_T.F_T & -k_T.F_T^* & -k.F_L^g & -k_T^g.F_T^g & \rightarrow u_3(h/2) \\
0 & 0 & i\alpha.F_L & i\alpha.F_L^* & -i\beta.k_T.F_T & i\beta.k_T.F_T^* & -i\alpha^g.F_L^g & \beta^g.k_T^g.F_T^g & \rightarrow \sigma_{11}(h/2) \\
0 & 0 & i\beta.k_L.F_L & -i\beta.k_L.F_L^* & i\alpha.F_T & i\alpha.F_T^* & -i\beta^g.k_L^g.F_L^g & -i\alpha^g.F_T^g & \rightarrow \sigma_{13}(h/2) \\
\hline
L_{ext}^{-} & S_{ext}^{-} & L^{+} & L^{-} & S^{+} & S^{-} & L_{ext}^{+} & S_{ext}^{+} &
\end{array} \tag{2.18}$$

Where $F_{L,T} = e^{ik_{L,T}h/2}$,$\alpha = \rho(\omega^2 - 2c_T^2k^2)$ and $\beta = 2\rho k c_T^2$, h being the plate thickness, ρ the mediums density and $\omega = 2\pi f$, f being the wave frequency. For the equation of F, α and β with a subscript g, the longitudinal/shear wave speeds and the density are substituted by the ones of the surrounding medium. In Eq. 2.18 each column stands for one partial wave amplitude in each layer, including the two half spaces. On the other hand, each line corresponds to the continuity of the displacements and stresses applied in each layer interface.

To obtain non trivial solutions for the vector of partial wave amplitudes A, the determinant of the global matrix must be zero. This constraint will allow only particular Lamb wave numbers k for a given frequency, corresponding to each mode. The following linear combinations were applied to the columns and rows to simplify the determinant calculation:

$\frac{1}{2}(c_3 + c_4) \to c_3, \frac{1}{2}(c_4 - c_3) \to c_4, \frac{1}{2}(c_5 + c_6) \to c_5, \frac{1}{2}(c_6 - c_5) \to c_6,\ (l_2 + l_6) \to l_2,$
$(l_3 + l_7) \to l_3,\ (l_1 - l_5) \to l_1,\ (l_4 - l_8) \to l_8,\ (c_1 + c_7) \to c_7, (c_2 - c_8) \to c_8, \frac{1}{2}c_4 \to$
$c_4, \frac{1}{2}c_5 \to c_5$

Thus, the determinant of $[G]$ can be calculated as follows:

$$\det(G) = \begin{vmatrix} -k_L^g & -k & k_L.\cos\left(\frac{k_L h}{2}\right) & k.\cos\left(\frac{k_T h}{2}\right) \\ k & -k_T^g & -i.k.\sin\left(\frac{k_L h}{2}\right) & i.k_T.\sin\left(\frac{k_T h}{2}\right) \\ i\alpha^g & i\beta^g.k_T^g & \alpha.\sin\left(\frac{k_L h}{2}\right) & \beta.k_T.\sin\left(\frac{k_T h}{2}\right) \\ -i\beta^g.k_L^g & i\alpha^g & i.\beta.k_L.\cos\left(\frac{k_L h}{2}\right) & -i\alpha.\cos\left(\frac{k_T h}{2}\right) \end{vmatrix} . \begin{vmatrix} i.k_L.\sin\left(\frac{k_L h}{2}\right) & i.k.\sin\left(\frac{k_T h}{2}\right) & -k_L^g & k \\ k.\cos\left(\frac{k_L h}{2}\right) & -k_T.\cos\left(\frac{k_T h}{2}\right) & -k & -k_T^g \\ i.\alpha.\cos\left(\frac{k_L h}{2}\right) & i.\beta.k_T.\cos\left(\frac{k_T h}{2}\right) & -i\alpha^g & i.\beta^g.k_T^g \\ -\beta.k_L.\sin\left(\frac{k_L h}{2}\right) & \alpha.\sin\left(\frac{k_T h}{2}\right) & -i\beta^g.k_L^g & -i\alpha^g \end{vmatrix} = 0 \tag{2.19}$$

As described in Eq. 2.19, the determinant of the global matrix is calculated as a product of two determinants. The determinant on the left corresponds to the anti-symmetric modes and the one on the right to the symmetric modes. In the framework of SSI, the radiation force induces mainly displacements perpendicular to the plate, generating mainly an anti-symmetric mode; therefore the attention will be focus in solving only the left determinant of Eq. 2.19 using a Nelder-Mead minimization method as described in [46], [55], [56]. Since the plate is embedded in an elastic medium attenuation of the guided wave will occur due to energy leakage into the surrounding medium. Thus, as explained in [55], for solving Eq. 2.19 complex wave vectors k will be searched: the real part being related to the phase velocity and the imaginary part to the attenuation.

2.2.5 Lamb wave empirical formula

For some particular medical applications (shear wave imaging in medium such as cornea, skin or arterial wall), it is much simpler to use an empirical formula based on the Lamb theory (Eq. 2.20) to derive the plate shear wave speed rather than solving Eq. 2.19. In Eq. 2.20, V is the phase velocity of the guided Lamb wave.

$$V = \sqrt{\frac{\omega . h . c_T}{2\sqrt{3}}} \tag{2.20}$$

This empirical formula was first proposed by *M. Couade et al.* [45] for the shear modulus assessment of the arterial wall. Then, the validity of this empirical formula was discussed in the work of *T. M. Nguyen et al.* [46] in the case of thin elastic plates submerged in water. In [46] Eq. 2.20 was tested for plates thicknesses and shear wave speeds ranging between 0.5 and 1.5 mm and 5 and 10 m/s respectively. An agreement within 5% between simulated dispersion curves and the empirical formula was found for the thinner and harder plates.

2.3: Materials and methods

2.3.1 Phantoms preparation

Experiments on three types of phantoms were performed. Phantom dimensions were 10 x 15 x 15 cm^3. Phantom A consists of an elastic plate of 1.1 ± 0.1 mm thickness surrounded by a Polyvinil Alcohol Cryogel (PVA-C) [57]. The layer, also made of PVA-C, underwent 4 freeze-thaw cycles while the surrounding gel only underwent one cycle. Phantom B consists of a three cycles PVA-C layer of 2.2 ± 0.2 mm thickness surrounded by a one cycle PVA-C gel. The number of freeze-thaw cycles is directly related to the final phantom's shear wave speed: the more cycles the sample underwent the higher the sample's shear wave speed is [57]. Phantom C consists of an agar layer (2% agar diluted in water) of 2.2 ± 0.2 mm thickness surrounded by gelatine based gel (4% gelatine, 1% agar as ultrasound scatter diluted in water). Layer thicknesses were measured from the B-Mode image. For each kind of phantom a homogenous bulk gel sample of dimensions 4 x 4 x 10 cm^3 was made from the same melt following an identical procedure as the different central layers in order to measure the bulk shear wave dispersion curve of the material, e. g. Bulk Sample A corresponds to a bulk sample made of the same material and following the same procedure as the central layer of Phantom A. No bulk samples were made for the outer layers of the different phantoms. For each phantom, both 1D transient elastography and SSI were applied successively without moving the probe. The experimental setup is presented in Fig. 2.2.

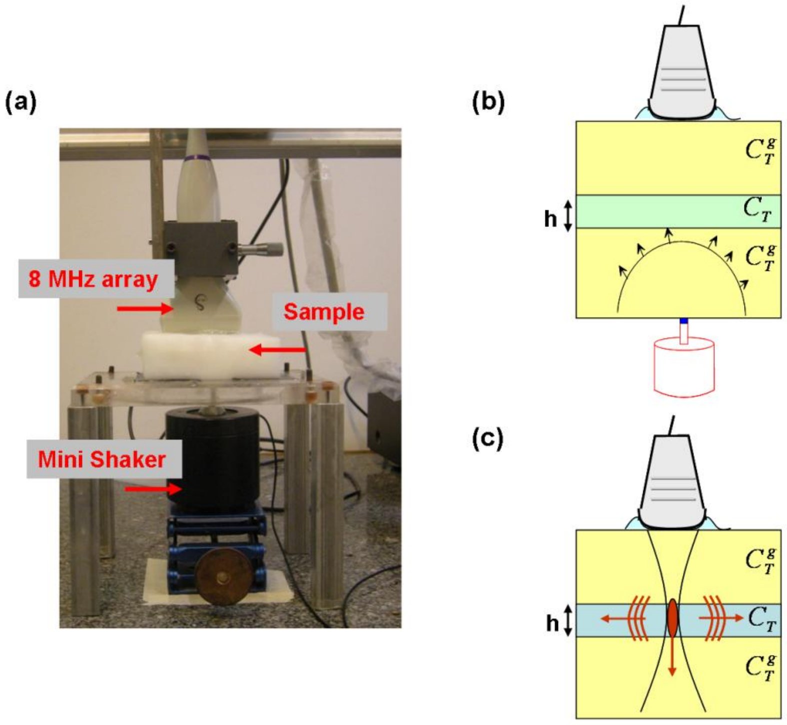

Fig. 2.2 (a) Experimental Setup. (b) 1D transient elastography: in a first step a low frequency elastic field was created using a mechanical vibrator. The black arrows indicate the propagation direction. (c) SSI: in a second step an elastic field was created using the ultrasonic radiation force. In both cases the displacement field was caught using an ultrafast ultrasound scanner. c_T stands for the shear wave speed in the plate while c_T^g stands for the shear wave speed in the surrounding gel.

2.3.2 One dimensional transient elastography

For the 1D transient elastography experiment, a 5 mm diameter piston attached to a mechanical vibrator (Mini-shaker, type 4810, Bruel&Kjaer, Denmark) working from 100 to 400 Hz acts on the phantom's surface generating shear waves inside the sample (Fig. 2.2(b)). For each frequency the vibrator was excited with a one-cycle sinusoid at the corresponding central frequency. The longitudinally polarized shear wave propagating along the piston axis is imaged using an ultrafast ultrasound scanner at 3000 frames/s (Aixplorer, Supersonic Imagine, Aix en Provence, France) and an ultrasonic array (256 elements, 8 MHz central frequency, pitch 0.2 mm) (SL 15-4, Supersonic Imagine, Aix en Provence, France) through a RF data cross-correlation algorithm [15], [19].

2.3.3 Supersonic Shear Imaging

For the SSI experiment, the ultrasonic radiation force is used as a shear wave source (Fig. 2.2(c)). Once again an ultrafast ultrasound scanner (Aixplorer) is used to drive a conventional ultrasonic probe by a per channel programming in transmit and reception mode. The SSI technique allows to focus ultrasound on several points ("pushing sequence") along the ultrasonic axis in order to generate a quasi plane shear wave [18]. In a first step a pushing sequence consisting on three "pushing points" (100 μs duration each) at three different depths, 5 mm spaced and centred on the central layer position, is used to induce a transient axial displacement. As the sample relaxes a wave propagating perpendicularly to the ultrasonic beam axis is generated. Secondly the system is switched into an ultrafast imaging mode to image the shear wave propagation. For large homogeneous media the elasticity is directly deduced from the shear wave speed. In the case of thin layered soft tissues, where the wave propagation is guided along the plate due to the successive reflections on the plate boundaries, the relationship between shear wave speed and elasticity is more complex as it was described above.

2.4: Finite differences simulation

In order to verify the experimental dispersion curves and the theoretical model used, the SSI as well as the 1D transient elastography experience were simulated using an in-house finite differences simulation code (ACEL) developed at the Langevin Institute [58]. The code is based on the discretization of the equation of motion in an elastic medium by a Virieux scheme.

To model 1D transient elastography experiments, a one-cycle sinusoid excitation propagating through the surrounding gel and arriving at the thin plate was simulated for different excitation frequencies (from 100 to 400 Hz with 50 Hz step). The transient shear wave propagation inside the plate was isolated. In order to minimize boundaries reflections, a directional filter was applied by performing a two dimensional Fourier transform and eliminating the components for which the product $\omega k < 0$ [59]. Then, for each excitation frequency, the phase velocity was calculated leading to the shear wave dispersion curve. Plates of 2.5 and 1 mm thickness with shear wave speed of 10 and 5 m/s were simulated. For all 1D transient elastography simulations the shear wave speed of the surrounding medium was set to 3 m/s while the density and the longitudinal wave speed were set to be constant through the sample with values 1000 kg/m^3 and 1500 m/s respectively. The displacement field was sampled at 10 kHz rate.

For the SSI simulations, plates with a thickness ranging from 0.9 to 2.5 mm and a transverse speed from 5 to 12 m/s were investigated. The shear source was defined as a broadband signal (350 – 1400 Hz) in agreement with the experimental conditions. A two dimensional Fourier transform is applied to the displacement movie in order to obtain the dispersion curve [60].

2.5: Experimental results

2.5.1 Phantom characterization

The SSI technique was used to obtain the dispersion curves for each bulk sample. The results for each type of bulk sample are presented in Fig. 2.3. By averaging the shear wave speed over the frequency range (from 500 Hz to 1300 Hz), a mean shear wave speed of 12.1m/s, 10.2 m/s and 5.6 m/s was found for bulk samples A, B and C respectively with a corresponding standard deviation of 0.2 m/s, 0.2 m/s and 0.4 m/s. These results are summarized in Table I, σ being the standard deviation and Δc_T the mean error calculated by averaging the error of each individual shear wave speed estimation over the frequency range.

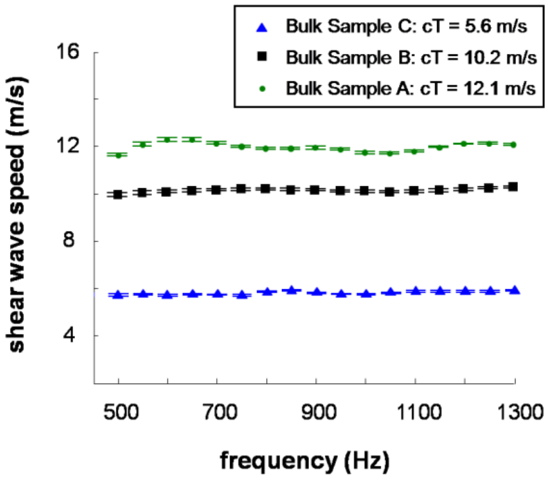

Fig. 2.3 Shear wave speed dispersion curves in bulk samples of the same material the plates were made of for phantom A (green dots), phantom B (black squares) and phantom C (blue triangles).

As explained in section 2.3.3 by using the SSI technique a shear wave is created using the radiation force of ultrasound. By focusing the ultrasonic beam on each phantom's surrounding medium a shear wave speed estimation of the material is obtained. Shear wave speed values of 3.8 ± 0.2 m/s, 4.2 ± 0.2 m/s and 1.2 ± 0.1 m/s were estimated for phantoms A, B and C surrounding material respectively. These values will be used later to calculate/simulate the “leaky" Lamb dispersion curves for the plate.

Table I

BULK SAMPLES CHARACTERIZATION

	c_T (m/s)	σ (m/s)	Δc_T (m/s)
A	12.06	0.16	0.05
B	10.22	0.19	0.06
C	5.64	0.39	0.05

2.5.2 1D Transient Elastography

Since the interest of 1D transient elastography relies on obtaining the displacement field along the piston axis, an average over the piston surface was made transforming the two dimensional displacement movie into a one dimensional seismogram. In Fig. 2.4, the corresponding displacement field obtained for 1D transient elastography experiments and the finite difference simulation for a 300 Hz central frequency excitation are presented. The longitudinal (L) as well as the shear wave (S) created by the piston are clearly visible. Note the similarity between the measured and the simulated displacement field. The plate position is marked in each figure with dotted lines. A transmitted and a reflected wave are clearly visible at the plate interface. In order to minimize boundaries reflections, a directional filter was applied by performing a two dimensional Fourier transform to the measured/simulated displacement field and eliminating the components for which the product $\omega k < 0$ [59]. This procedure filters the waves propagating along the piston axis, which are travelling "towards" the piston.

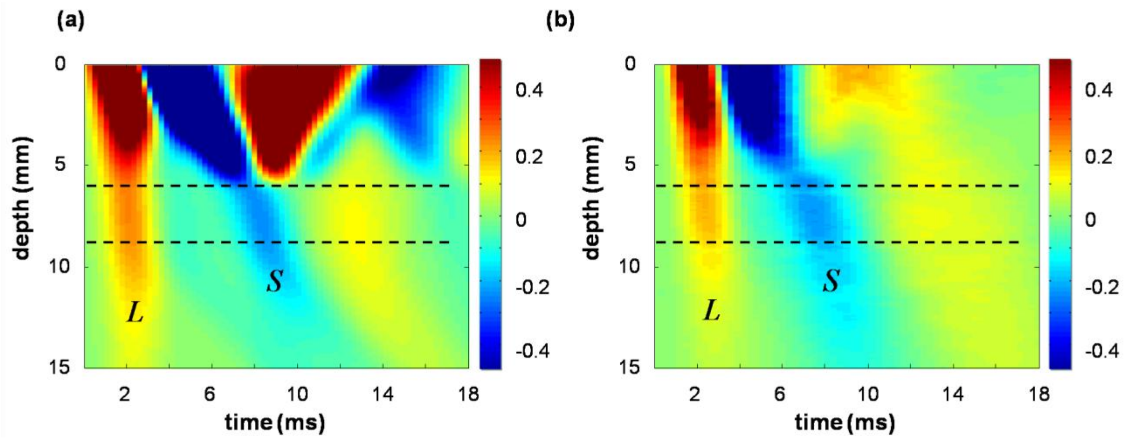

Fig. 2.4 (a) Normalized displacement field for a 300 Hz excitation obtained using finite difference simulation (ACEL). The plate shear wave speed and thicknesses are set to 10 m/s, 2.5 mm respectively. (b) Experimental normalized displacement field for a 300 Hz excitation obtained by 1D transient elastography for phantom B. The dotted line indicates the plate position. The piston position corresponds to 0 mm on the depth axis. The longitudinal (L) as well as the shear wave (S) created by the piston are clearly visible.

The transient transmitted part of the shear wave was then isolated within the plate. The phase velocity was calculated by applying a linear regression on the time of flight as a function of depth (Fig. 2.5). The time of flight was estimated from the phase estimation using a Fourier transform of the transient wave divided by the angular frequency. Finally the dispersion curves for the different phantoms were obtained by repeating this procedure for each excitation frequency (Fig. 2.6). The error provided for each individual shear wave speed estimation is the error on the linear fit.

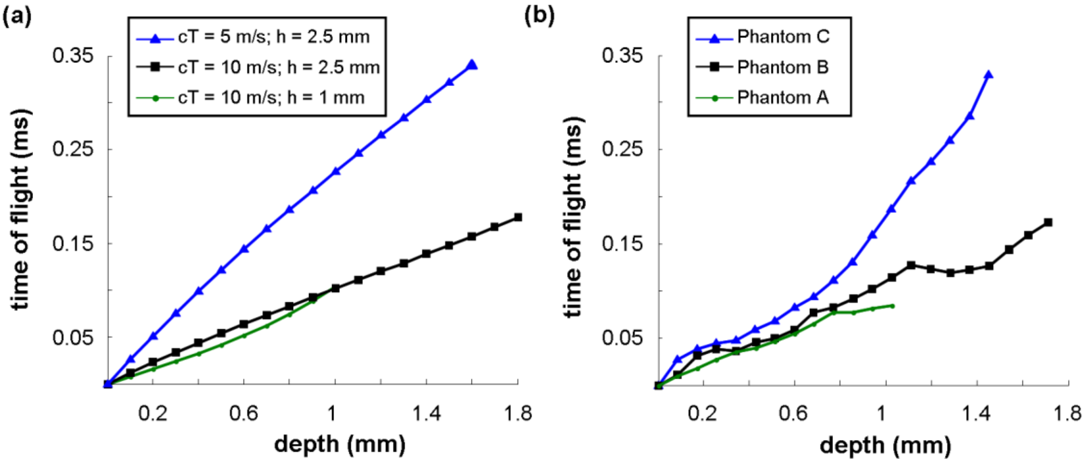

Fig. 2.5 Time of flight estimation inside the layer for a 300 Hz excitation. (a) Finite difference simulation and (b) experimental results.

Simulated dispersion curves are presented in Fig. 2.6(a). By averaging the shear wave speed over the frequency range (from 100 Hz to 400 Hz), mean shear wave speeds of 10.01m/s, 9.97 m/s and 4.79 m/s were found for the 10-m/s 1-mm-thick, 10-m/s 2.5-mm-thick and 5-m/s 2.5-mm-thick plates respectively with corresponding standard deviations of 0.50 m/s, 0.14 m/s and 0.13 m/s. The mean error (Δc_T) on each measurement was also calculated for the three cases yielding 0.58 m/s, 0.20 m/s and 0.05 m/s respectively. This error is due to numerical noise of the simulation and the computation procedure. These results are summarized in Table II.

Table II

SUMMARY OF 1D TE SIMULATIONS

Simulation Parameters		*1D Transient Elastography Simulation Results*		
c_T (m/s)	h (mm)	c_T (m/s)	σ (m/s)	Δc_T (m/s)
10	1	10.01	0.50	0.58
10	2.5	9.97	0.14	0.20
5	2.5	4.79	0.13	0.05

Performing the same calculations for the 1D transient elastography experimental dispersion curves presented in Fig. 2.6(b) a shear wave speed of 11.44 ± 0.46 m/s, 10.37 ± 0.55 m/s and 5.58 ± 0.22 m/s are found for phantoms A, B and C respectively with a mean error of 0.66 m/s, 0.39 m/s and 0.49 m/s. The results are summarized in Table III.

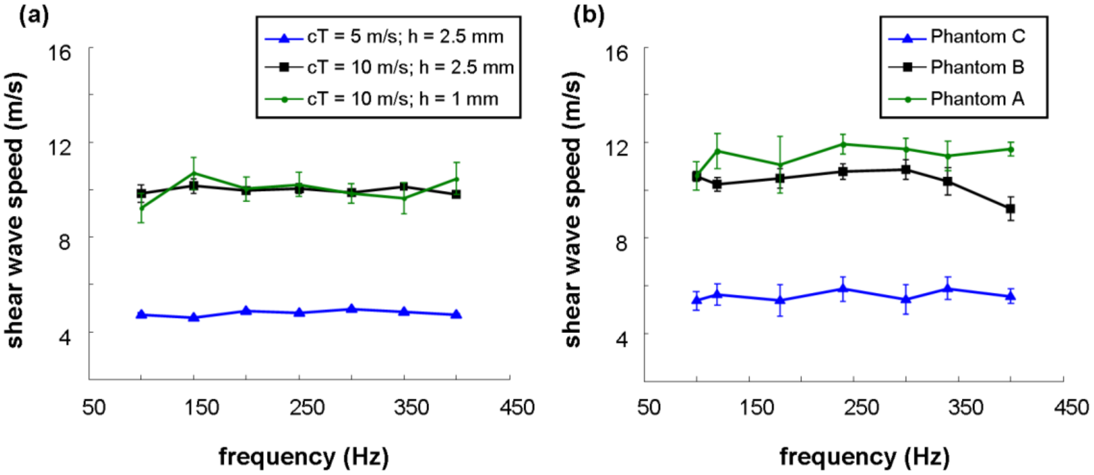

Fig. 2.6 Dispersion curves obtained applying 1D TE inside the plate (a) from finite differences simulation and (b) experimental results.

2.5.3 Supersonic Shear Imaging

The spatial-temporal displacement field obtained for a fixed depth within the layer and its corresponding 2D Fourier transform are presented in Fig. 2.7. From the 2D Fourier transform (Fig. 2.7(b)) the presence of a highly energetic mode is observed. This mode corresponds to the zero order anti-symmetric Lamb mode described by Eq. 2.19. Dispersion curves can be obtained from single acquisitions by using the concept of Shear Wave Spectroscopy (SWS) proposed by *Deffieux et al.* [61]. The dispersion curve is obtained by finding for each frequency the phase velocity at which the Fourier transform amplitude is maximal. For the final dispersion curve an average over the plate thickness is performed. The error for each individual measurement is provided by the standard deviation. The results are presented in Fig. 2.8.

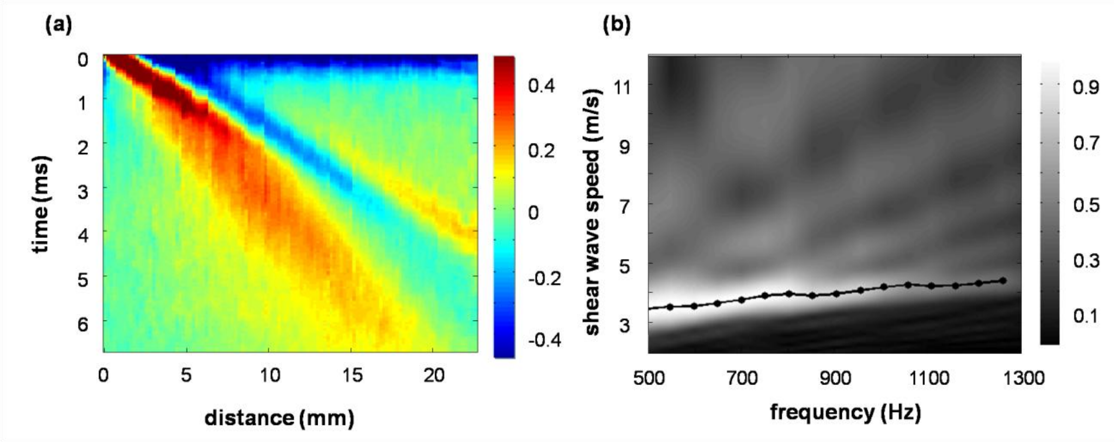

Fig. 2.7 (a) Normalized displacement field inside the plate for phantom C as function of time (ms) and distance (mm) for the SSI experience. (b) 2D Fourier transform (energy) of the displacement field in (a). The energy is normalized to one for each frequency. The extracted dispersion curve is also represented in black dots.

In Fig. 2.8 the theoretical (Fig. 2.8(a)) and simulated (Fig. 2.8(b)) dispersion curves are presented. The theoretical model was calculated, by performing a least-mean-square fit on the theoretical dispersion curves obtained through Eq. 2.19 to the experimental data (Fig. 2.8(a)). The model proposed by Eq. 2.19 has seven independent parameters: the density, the shear/longitudinal wave speed for each medium (plate and surrounding gel) and the plate thickness. Both densities and longitudinal wave speeds were assumed to be constant throughout the sample (1000 kg/m^3 and 1500 m/s respectively). With this assumption (valid for biological tissues), only three parameters can be adjusted in order to minimize the sum of squares: the shear wave speeds (c_T^g and c_T) and the plate thickness (h). While the parameter c_T was allowed to vary freely, c_T^g and h were allowed to vary between the upper and lower limit of each measured parameter by taking into account the error provided for each measurement, e.g. for Phantom A, c_T^g was allowed to vary between 3.6 m/s and 4.0 m/s while h was allowed to vary between 0.9 mm and 1.3 mm. The resulting plate shear wave speeds are 12.23 ± 0.27 m/s, 10.96 ± 0.28 m/s and 5.74 ± 0.07 m/s for phantoms A, B and C respectively. The shear wave speed error was calculated by taking into account the error on the experimental data. The results are summarized in Table III.

Table III

SUMMARY OF EXPERIMENTAL RESULTS

	Bulk Sample		*SSI on Phantom*		*1D Transient Elastography on Phantom*		
	c_T (m/s)	σ (m/s)	c_T (m/s)	Δ c_T (m/s)	c_T (m/s)	σ (m/s)	Δ c_T (m/s)
A	12.06	0.16	12.23	0.27	11.45	0.46	0.66
B	10.22	0.19	10.96	0.28	10.36	0.55	0.39
C	5.64	0.39	5.74	0.07	5.58	0.22	0.48

For the simulated dispersion curves a different approach was used: for each phantom two dispersion curves were simulated corresponding to the upper and lower limit of the shear wave speed estimation from the bulk sample and the plate thickness by taking into account the error provided for these measurements (Fig. 2.8(b)). The corresponding values of shear wave speed and thickness for phantom A are c_T = 12.33 m/s, h = 1.3 mm for the upper limit and c_T = 11.90 m/s, h = 0.9 mm for the lower limit. For phantom B the corresponding values are c_T = 10.41 m/s, h = 2.4 mm for the upper limit and c_T = 10.03 m/s, h = 2.0 mm for the lower limit. For phantom C the utilized values are c_T = 6.03 m/s, h = 2.4 mm for the upper limit and c_T = 5.25 m/s, h = 2.0 mm for the lower limit. These parameters are summarized in Table IV.

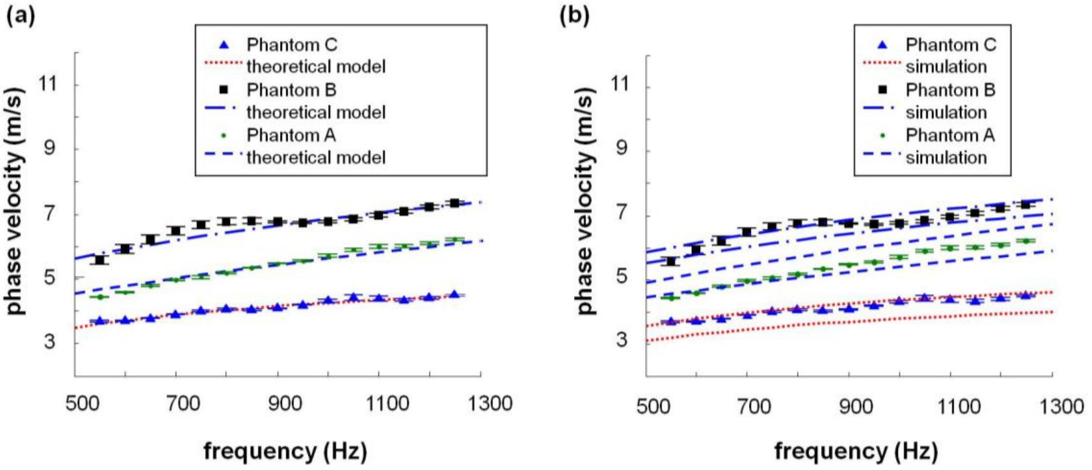

Fig. 2.8 Dispersion curves obtained by SSI. Comparison with (a) theoretical curves obtained by fitting the experimental data to the Lamb theory and with (b) curves obtained from finite difference simulation. The shear wave speed values for the simulations were obtained from the bulk sample with its corresponding error. The error in the thickness was also taken into account.

In section 2.2.5, an empirical formula for recovering the plate bulk shear wave speed from the dispersion curve was presented (Eq. 2.20). The validity of this empirical formula was discussed in the work of *T. M. Nguyen et al.* [46] in the case of thin elastic plates submerged in water. In [46], Eq. 2.20 was tested for plates thicknesses and shear wave speeds ranging between 0.5 and 1.5 mm and 5 and 10 m/s respectively, showing that the relative deviation of the empirical formula from simulated dispersion curves is as much as 15% for the thickest and softest plates. However its deviation was less than 5% for plates of 1 mm thickness whose shear wave speeds were greater than 10 m/s. Because of the above mentioned limitations, Eq. 2.20 will be used to retrieve the plate shear wave speed only for Phantom A. For Phantoms B and C, since the plate thickness is 2.5 mm and the shear wave speed is approximately less than 10 m/s, the empirical formula could not be applied to retrieve the plate shear wave speed. A bulk shear wave speed value of 12.86 ± 0.66 m/s was retrieved by fitting Eq. 2.20 in a least square sense for phantom A.

Table IV

SUMMARY OF SSI SIMULATION PARAMETERS

	Upper Limit		*Lower Limit*	
	c_T (m/s)	h (mm)	c_T (m/s)	h (mm)
Phantom A	12.22	1.3	11.90	0.9
Phantom B	10.41	2.4	10.03	2.0
Phantom C	6.03	2.4	5.25	2.0

2.6: Discussion

This Chapter presents and compares two different Transient Elastography techniques for the assessment of thin elastic layers. The main difference between both techniques (1D transient elastography and SSI) lies in the way the shear wave is generated. Whereas the vibrator used in 1D transient elastography polarizes the shear wave in such a way that it passes through the plate without being guided. Parallel the acoustic radiation force used in the SSI technique generates a Lamb wave strongly guided inside the plate. These differences in the propagation mode strongly differentiate the inverse problem used in both techniques.

By carefully comparing Fig. 2.6 and Fig. 2.8, it can be noted that no guidance of the shear wave inside the plate was observed for the 1D transient elastography contrary to the Lamb wave used in the SSI technique. A good qualitative agreement is found between the simulated and the experimental dispersion curves.

For the 1D transient elastography simulations, a general agreement within a relative deviation of 1.5% in average is found between the input and the estimated shear wave speed value (Table II). The relative deviation for a single measurement is calculated as $|c_T^{mes} - c_T|/c_T$, where c_T^{mes} is the measured shear wave speed and c_T is the shear wave speed simulation parameter. A mean relative error of 3% is found for each individual set of simulation parameters. It can be noticed that the absolute error in each measurement increases as the plate thickness decreases and the shear wave speed increases. This fact is mainly due to the following two reasons. Firstly the faster the wave propagates, the more difficult it is to isolate the transmitted transient shear wave. In this case the shear wave speed estimation is biased by reflected waves that could not be eliminated by the directional filtering along the depth axis [14]. Secondly, the thinner the plate is, the fewer points there are inside the plate for the estimation of the shear wave speed from the time of flight estimation as a function of depth (Fig. 2.5).

For the 1D transient elastography measurements (Table III) an agreement within a relative deviation of 3% in average is found between the bulk sample and the 1D transient elastography experimental shear wave speed estimation. The same behavior of the absolute error on the shear wave speed estimation as the one described in the previous paragraph for the simulation results was encountered for the 1D transient elastography experiments. This could set a limitation to 1D transient elastography making it difficult to apply in very thin and hard plates. In the case of 1D transient elastography the shear wave estimation depends on the time of flight measurement through several experimental parameters: ultrasonic frequency, temporal sampling rate, piston excitation frequency, plate thickness and elasticity. The higher the ultrasonic frequency and sampling rate are, the higher the spatial/temporal resolution on the experimental displacement field is. A higher spatial resolution will result in an increase on the number of points inside the plate for the phase estimation. On the other hand an increase in the sampling rate will help to a better isolation of the transient shear wave transmitted into the plate. Although usually an increase on the sampling rate alone is not enough to isolate the transmitted shear wave since it also depends on the shear wave frequency and wavelength, or equivalently on the plate elasticity and piston excitation frequency. The softer the plate and the higher the excitation frequency the smaller the shear wavelength is, making it easier to isolate the transient part. This has its disadvantages, since attenuation increases with frequency: for very high frequencies only very "shallow" plates can be characterized. For the configuration used in the present Chapter and based on the experience I say that the minimum thickness required to have a reliable shear wave speed estimate is 1mm for a 10 m/s propagating shear wave, although further studies need to be carried out on this point for different choices of the experimental parameters.

For the SSI experiment, a good agreement is found between the experimental measurements and the theoretical/simulated dispersion curves (Fig. 2.8). In the case of the theoretical dispersion curves, this fact is supported by a mean normalized correlation coefficient of 0.97 ± 0.03 and a mean variance of 0.02 m/s between the model and the experimental data. For the simulated dispersion curves a mean normalized correlation coefficient of 0.97 ± 0.03 and a mean standard deviation of 0.26 m/s are found. For all cases, the experimental dispersion curves lie between the error margins of the simulated curves. This confirms a good agreement between simulation and experience.

The shear wave speed of the plate for each phantom was retrieved by using the generalized Lamb wave model (Table III). An agreement within 3.5 % is found between the bulk sample and the SSI experimental shear wave estimation. The validity of the Lamb model (Eq. 2.19) was proven to be valid in plates whose thickness and stiffness ranges are corresponding to cornea, skin and vascular applications [46]. The results presented in this work confirm these findings and cross validate it with a different approach: 1D transient elastography.

For phantom A, the plate shear bulk wave speed was retrieved by fitting the empirical formula (Eq. 2.20). The validity of the empirical formula has been demonstrated in a liquid/plate/liquid configuration for very thin plates (≤ 1.5 mm) [46]. In the case of Phantom A, we are dealing with a very thin plate but in a gel/plate/gel configuration. The consequence of a non-liquid surrounding medium is an increased phase velocity at a given frequency [45]. This effect is small when the surrounding medium stiffness is small compared to plate stiffness [45]. Despite the above mentioned biases, the obtained value agrees within the margins of error with the shear wave speed obtained by fitting the Lamb model, the bulk sample estimation and 1D transient elastography.

Finally, both techniques (1D transient elastography and SSI) result in the same bulk shear wave speed estimation (and consequently stiffness) within the margins of error provided in Table III. The absolute and relative error in the bulk shear wave speed estimation is smaller for the SSI technique than for 1D transient elastography. A very good agreement within 5 % was found between the 1D transient elastography and the SSI techniques. The main advantage of 1D transient elastography stands here in its simplicity of application as the true shear wave speed is directly retrieved from a time of flight algorithm. Interestingly, the diffraction pattern of the shear wave in the near field of the generating piston is particularly well suited to such plate stiffness estimation as the wave polarization is parallel to its propagation direction and perpendicular to the plate. This well adapted geometry optimizes the wave propagation pattern that is not affected by guidance effects, at least along the ultrasonic beam. Besides, the obtained information is only one dimensional. It is probable that Lamb type modes propagating in a direction parallel to the plate are generated after the shear wave is transmitted into the plate. Further studies involving guided wave propagation inside soft solids need to be carried out.

In order to retrieve two dimensional information, the SSI technique uses a completely different propagation mode (Lamb wave) for which the inverse problem requires a much more complex acquisition sequence and post-processing analysis: dispersion effects have to be measured using shear wave spectroscopy [61] and used for the recovery of the plate stiffness.

2.7: Conclusions

In this Chapter, the use of 1D transient elastography for the assessment of the elasticity of sub-wavelength layered soft tissues is proposed. The good agreement between the 1D transient elastography shear wave speed estimations and the material shear wave speed as well as the simulations validate the use of this technique. The obtained results were also compared with the ones obtained by the SSI technique. Through both techniques the same shear wave speed estimation is obtained, although the physical wave propagation is different. The 1D transient elastography proposed technique has some advantages: it is non-invasive and low cost (only one transducer can be used). Most interestingly, thanks to optimized diffraction effects in the near field of the vibrating piston, the shear wave speed can be directly retrieved without needing a propagation model.

Chapter III

Time reversal elastography: a quantitative elasticity imaging technique

---

In previous chapters (Chapter I and II) several elastography techniques were presented. All the techniques have one thing in common: they use a controlled source (e.g. mechanical vibrator or acoustic radiation force) to generate the shear wave. In this Chapter, a completely different approach is proposed. A novel imaging modality for extracting the soft tissues shear elasticity from a complex reverberated elastic field generated by a set of uncontrolled sources is presented: Time Reversal Elastography (TRE) [2]-[4], [10]. The key concept in TRE is the use of spatiotemporal correlations interpreted in the frame of the time-reversal symmetry.

Since the fundamental idea of TRE relies on time reversal and noise correlation, I will begin this Chapter by briefly describing the time reversal principles, in particular one channel time reversal mirror and its equivalence with noise correlation. Then I will present the main features of an active shear wave one channel time reversal experiment in the volume of a soft solid and its application to elastography by summarizing the results of the pioneering works of *Catheline et al.* [2] and *Benech et al.* [3] developed in the Laboratorio de Acústica Ultrasonora (L.A.U.), Facultad de Ciencias, Universidad de la República, between 2007 and 2009. This will set the basic principles of the TRE technique.

During the last part of the Chapter, I will present the TRE technique and the main results obtained during this thesis. First, in order to demonstrate the feasibility of TRE as a quantitative elasticity imaging technique, *in vitro* experiments on bi-layer tissue mimicking phantoms were carried out. Since the idea is to extract the shear elasticity from a complex elastic field, the following two step experiment is conducted: in a first step, a complex wave field is created inside the phantom by randomly tapping it on its surface with the fingers. The displacement field is measured inside the sample by means of an ultrasonic speckle tracking technique. In a second step a virtual time-reversal experiment is performed in the computer by using cross-correlations. Shear waves will be virtually focused on each imaging point, resulting in a 2D focus. From the time reversal point of view, the shear elasticity can be obtained by two different ways: by measuring the wave speed as the wave converges or by measuring the focal width which is related to the shear wavelength through Rayleigh criteria. This Chapter is devoted to this latter approach. In order to retrieve a quantitative elasticity estimation from the focal spot size, in this thesis, the Rayleigh criteria is extended by developing an analytical expression relating the focal spot size and the shear wave speed for a vectorial wave field in the volume of an elastic solid. Finally, by locally measuring the focal size a quantitative shear wavelength tomography is conducted, resulting in shear elasticity image.

Second, to show the potential of TRE as an imaging technique, a feasibility *in vivo* study in the human liver was carried out. For this case, the complex elastic field is created by the physiological noise present in the human body due to cardiac beating and breathing. To conclude, the feasibility of the TRE technique for detecting small inclusions will be tested.

3.1: Time Reversal principles

3.1.1 Closed Cavity

One key concept in understanding TRE is time reversal. The time reversal technique is an efficient way to focus a wave back to its source. Its applications have been investigated in a wide range of areas. In a non exhaustive list it can be mentioned telecommunications [62], underwater acoustics [63], nondestructive testing [64], interactivity [65] and medical therapy and imaging [66]. The original idea was proposed in the nineties by *M. Fink et al.* [1] and is based on the time-reversal invariance of the wave equation in a lossless medium. Time reversal focusing is a two step process. In a first step, the direct wave scene is recorded: the impulse response of point A (Fig. 3.1 (a)) is measured by the set of receivers S_i forming a perfect time reversal cavity. Due to the impulsive character of the source, the recorded responses are the Green functions between point A and the observation point S_i : $G(A, S_i; t) = G_{AS_i}(t)$. In a second step, the recorded wave is time reversed $G_{AS_i}(-t)$ and reemitted into the medium through the same point S_i (Fig. 3.1. (b)). As a consequence of spatial reciprocity and the $t \to -t$ invariance of the wave equation in a lossless medium, the wave will travel the same original path but in opposite sense to focus at the original source position and then diverge. The maximum amplitude of the acoustic field will be found in A at time $t = 0$. For an ideal cavity the time reversed field can be written as:

$$RT_{AB}(t) = G_{AB}(t) - G_{AB}(-t) \tag{3.1}$$

This idealized time reversal experiment usually requires the use of multiple channel electronics to be performed and the set of receivers should form a closed surface around the source. This latter is not possible in many practical applications leading to the use of only one portion of the ideal cavity: a time reversal mirror [67]. In this case due to diffraction effects the refocalization field is deformed. An elegant way to avoid this problem is to use the so-called one channel time reversal mirror [68].

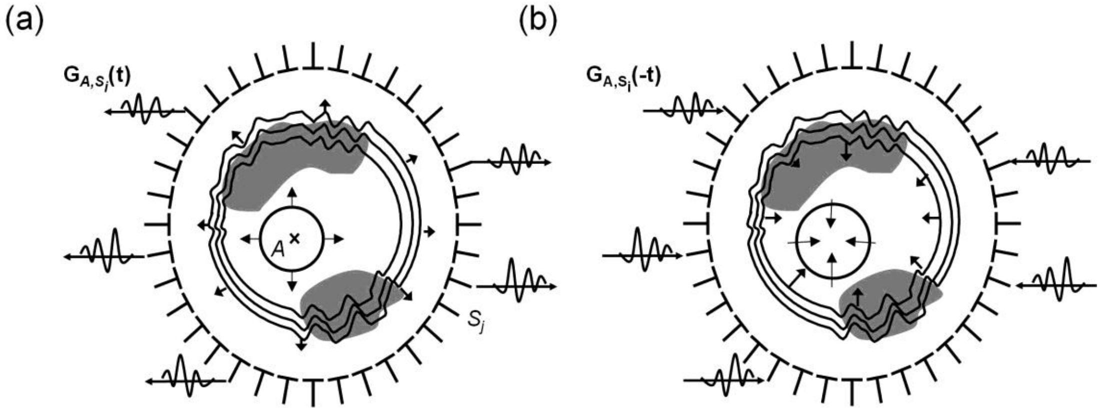

Fig. 3.1 Schematic representation of an idealized time reversal experiment. (a) The first step in a time reversal experiment consists in the observation of the forward wave scene: the impulse response of point A is measured by the set of receivers S_i forming a perfect time reversal cavity. (b) In a second step, the recorded wave is time reversed and reemitted into the medium through the same point S_i. As a consequence of spatial reciprocity and the $t \rightarrow -t$ invariance of the wave equation in a lossless medium, the wave will travel the same original path but in opposite sense to focus at the original source position.

3.1.2 One channel time reversal mirror

Theoretical and experimental time reversal works in reverberant solid cavities have led to the so-called one channel time reversal mirror where only one point source is needed to get a focusing of the wave field [68]. The idea is to replace the time reversal cavity by highly reflective boundary conditions (Fig 3.2). If the cavity is chaotic, the multiple wave paths will cover all the limiting surface. In that case the response G_{AS} in a point S contains all the necessary information due to multiple reverberations to focus back to the source A. In the reemission step of a time reversal experiment, the reemitted signal will follow the reverberation path but in the opposite sense, leading to a focalization around point A. Based on the linear system theory, an expression for the time reversed field can be found as the time-convolution product of the emitted signal and the Green function between the emitting and the receiving point.

$$RT_{AB}(t) = G_{SB}(t) \otimes G_{AS}(-t) \tag{3.2}$$

Another way to replace a perfect time reversal cavity is based on multiple diffusion. In the latter case, the time reversed field is the same as in Eq. 3.2 but instead of using reverberations due to multiple reflections, the waves will encounter a great number of diffusers, leading to a refocalization based on the same principle. The closed time reversal cavity is now replaced by multi-diffusion instead of reverberation.

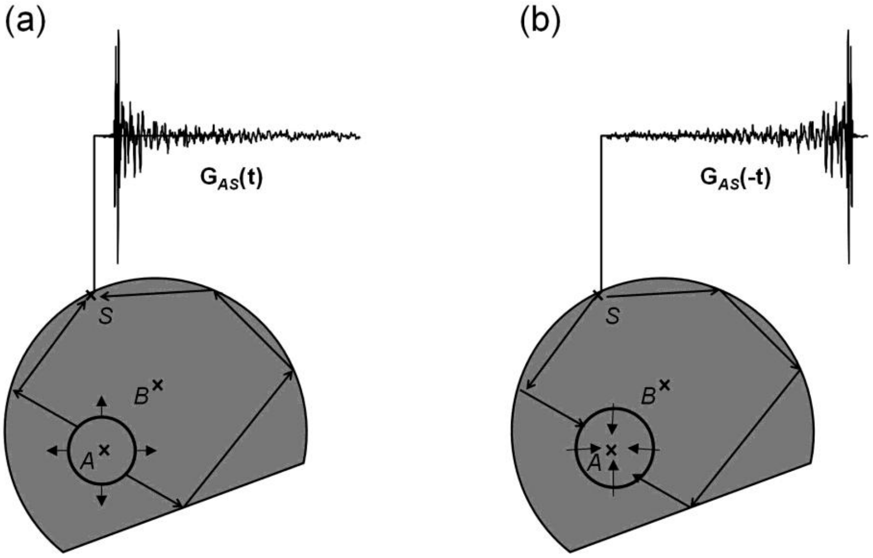

Fig. 3.2 Schematic representation of a one channel time reversal experiment. (a) Forward wave scene: a reverberated field is measured in point S due to a source in A. (b) In the reemission step of a one channel time reversal experiment, the reemitted signal will follow the reverberation path but in the opposite sense, leading to a focalization in A.

3.1.3 Relationship between time reversal and noise correlation

I have mentioned above that the key concept in TRE was noise correlation interpreted in frame of time reversal. Hereinafter, the relationship between time reversal and noise correlation will be introduced in a qualitatively way. A deeper quantitative insight on this subject will be given in section 3.3.1.

Under certain conditions the correlation between signals received in the points A and B converges towards the Green function between A and B. The goal of correlation computing is then to extract information of the medium between two receiving points without any active source, by just recording the ambient noise. By ambient noise, it means a low amplitude signal without any apparent spatial-temporal coherence. The ambient noise signals are issued of a more or less complex wave propagation and it is difficult to identify the distribution of random noise sources. This could be the case of a signal, due to multiple reverberation or diffusion. The correlation of two impulsional responses recorded in points A and B due to a source placed in S is given by the following expression:

$$C_{AB}(t) = G_{SB}(t) \otimes G_{SA}(-t) \tag{3.3}$$

The spatial reciprocity property implies that the source and receiver can be inversed: $G_{AS} = G_{SA}$, leading to an equivalence between the time reversed field and the noise correlation. From the physical point of view the noise correlation can be interpreted as the time reversal in point B of a source placed in A through a time reversal mirror formed by the randomly distributed noise sources. This spatial diversity assures the equivalence between the reverberant cavity or multi-diffusion and the ensemble of noise sources.

To conclude: time reversal is based on controlling spatially and temporally a time reversal mirror while noise correlation is an operation, which uses a time reversal mirror formed by the ambient noise sources. If ψ is the field due to an impulsional source observed in points A and B, the spatial reciprocity hypothesis assures an equivalence between time reversal and noise correlation given by:

$$RT_{AB}^{S} = \psi_{SB}(t) \otimes \psi_{SA}(-t) = C_{AB}^{S} \tag{3.4}$$

3.2: Time Reversal of shear waves in soft solids

In order to illustrate the concepts presented on the preceding section in the case of soft solids I will summarize, below, the works of *Catheline et al.* [2] and *Benech et al.* [3] in which I participate as part of my Master thesis developed in the Laboratorio de Acústica Ultrasonora between 2007 and 2009 [69]. These works set the basis of the actual TRE technique. The main result in the work of *Catheline et al.* [2] was the demonstration that it was possible to perform a one channel time-reversal experiment using shear waves in the volume of a soft solid. A second, but nevertheless important result of his work, is the observation of a direction dependent Rayleigh criteria. In the work of *Benech et al.* [3], this is exploited to extract the shear wave speed and thus the shear elasticity using the equivalence between time reversal and cross-correlation, by performing a virtual time-reversal experiment in the computer.

The experimental setup used in both works is presented schematically in Fig. 3.3. The first step of a time reversal experiment consists in measuring the forward wave scene: for this purpose, a mechanical vibrator with an attached circular piston applied at point A is employed to generate an elastic wave field in an agar-gelatin based phantom. Two cycles of sinusoid were sent in the audible range ($\sim$ 150 Hz). The z-component of the resulting displacement field was measured by means of an ultrasonic speckle technique, using a 5 MHz central frequency ultrasonic transducer and an ultrafast pulse-echo system storing 500 ultrasonic signals at 1000 Hz rate, resulting in a 500 ms signal length. The measured elastic field is shown in a seismic-like representation in Fig. 3.3. Displacements are observed at times greater than the initial pulse duration ($\sim$ 10 ms), indicating the presence of a reverberated field. It must be noted at this point, that for nearly incompressible elastic solids, the field originated by point body sources at low frequencies ($\sim$ 100 Hz) is dominated by shear waves [14].

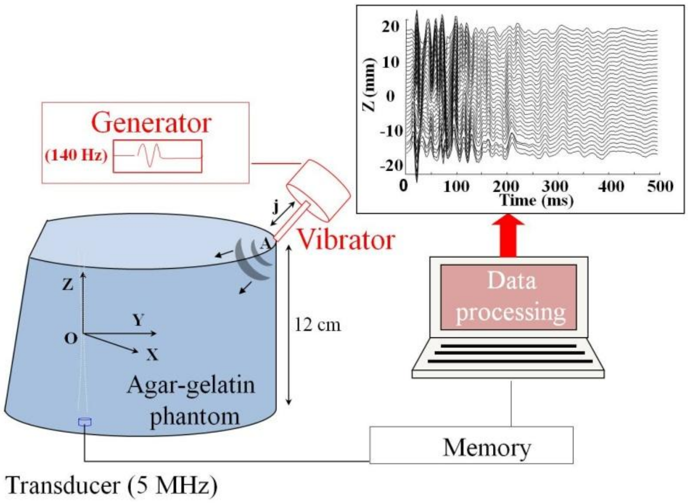

Fig. 3.3 Experimental setup used in the works of *Catheline et al.* [2] and *Benech et al.* [3] to conduct a one channel time reversal experiment inside a tissue mimicking phantom. **Source: *Catheline et al.* [2]**

Let $\psi_z(z_m,t)$ be the z component of the vectorial field at position z_m (e.g. one of the lines of the seismogram shown in Fig. 3.3). Let $e_j(A,t)$ be the temporal excitation of the source located in A and oriented towards an arbitrary direction j. From a linear system point of view, $\psi_z(z_m,t)$ can be expressed as a time-convolution product, between the excitation function $e_j(A,t)$ and the impulse response $h_{jz}(A,z_m;t)$ between the j and z component of the vectorial field between the source and receiver:

$$\psi_z(z_m,t) = e_j(A,t) \otimes h_{jz}(A,z_m,t) \tag{3.5}$$

Based on space reciprocity Eq. 3.5 can be rewritten as:

$$\psi_z(z_m,t) = \psi_j(A,t) = e_z(z_m,t) \otimes h_{zj}(z_m,A,t) \tag{3.6}$$

Therefore the measuring point z_m can be considered as a virtual source acting along the z direction. In order to perform the time reversal experiment, the source position was arbitrarily chosen to be $z_m = 0$. The resulting time-reversed field evaluated at an arbitrary position z_n can be now deduced from Eqs. 3.5 and 3.6 as:

$$\psi_z^{TR}(z_n,t) = \left(e_z(z_m,T-t) \otimes h_{zj}(z_m,A,T-t)\right) \otimes h_{jz}(A,z_n,t) \tag{3.7}$$

Where T is the total signal length.

3.2.1 Active time reversal experiment

The second step of a time reversal experiment consists in sending back to the medium the time reversed recorded signal: this is done by choosing the displacement field at z_m position (set arbitrary as zero), time reversing it and sending it back to the medium from the surface through the mechanical vibrator. The resulting time-reversed field displayed in Fig 3.4(a) is again measured by means of an ultrasonic speckle interferometry technique. The time recompression at $z = 0$ and the spatial focusing at $t = 500\, ms$ are represented at the top and right hand side of Fig. 3.4(a) respectively.

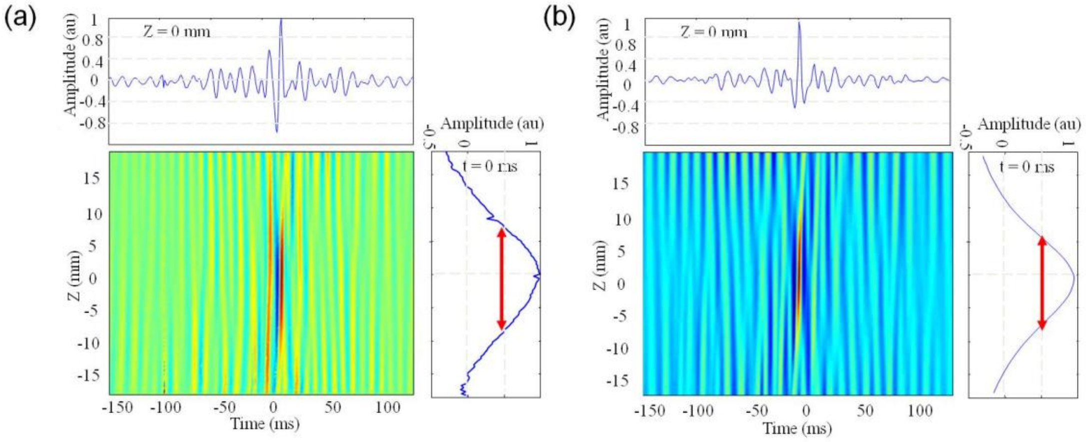

Fig. 3.4 Comparison between (a) a real time reversal experiment and (b) the correlation computation based on Eq. 3.7. **Source:** ***Benech et al.*** **[3]**

Based on these results, the shear wave speed can be retrieved by two different independent approaches using a time reversal experiment: measuring the wave speed as the wave converges or measuring the focal width at -6 dB which is related to the shear wavelength through Rayleigh criteria. Nevertheless, the above explained procedure, using a fully programmable emission electronics, remains inappropriate when thinking in real-time applications.

3.2.2 Cross correlation and time reversal

An alternative and simple way to simplify the experiment described above, is to use correlation algorithms. From the measured displacement field, the following correlation matrix can be computed:

$$\begin{aligned} &C_{zz}(z_m, z_n, t) = \psi_z(z_m, T-t) \otimes \psi_z(z_n, t) = \\ &= \left(e_j(A, T-t) \otimes h_{jz}(A, z_m, T-t)\right) \otimes \left(e_j(A, t) \otimes h_{jz}(A, z_n, t)\right) \end{aligned} \tag{3.8}$$

Is important to notice that if $e_j(A,t) = \delta(t)$ Eqs. 3.7 and 3.8 are equal to the cross-correlation between the impulse response h_{jz} evaluated at z_m and at z_n. Under this assumption, the correlation and the active time reversal experiment are strictly equal. The problem relies in real experiments: although the emission can be short when compared to the reverberation time, it cannot be regarded as instantaneous. Thus, the correlation field is related to the time reversal field through the following expression:

$$C_{zz}(z_m, z_n, t) = e_j(A,t) \otimes \psi_z^{TR}(z_n, t) \tag{3.9}$$

The correlation field is represented as function of space and time in Fig. 3.4(b). A good general agreement is obtained between the active time reversal experiment and the correlation computation. However, some differences appear when the temporal recompression is observed. While the time recompression of the active time reversal experiment has the parity of the emitted signal (Eq. 3.7), the time recompression issued from correlation necessarily results in an even function in time as expressed in Eq. 3.8.

Another important aspect, consequence of Eq. 3.9, is that the correlation field is a filtered version of the time reversal field through a convolution product with $e_j(A,t)$. In order to eliminate this dependence and to optimize the information contained in the correlation matrix, an extra step can be implemented in the post processing algorithm. This extra step is known as phase correlation.

Let $H(z,\omega)$ and $E(\omega)$ be the Fourier transform of $h_{zj}(z,A,t)$ and $e_j(A,t)$ respectively. Due to reciprocity of the elastic field $h_{zj}(z,A,t) = h_{jz}(A,z,t)$. Then, the Fourier transform of Eq. 3.8 reads:

$$\begin{aligned}\Im\left(C_{zz}(z_m, z_n, t)\right) &= E^*(\omega)\exp(-i\omega T)H^*(z_m,\omega)\exp(-i\omega T)E(\omega)H(z_n,\omega) = \\ &= \left|E(\omega)\right|^2 H^*(z_m,\omega)H(z_n,\omega)\exp(-2i\omega T)\end{aligned} \tag{3.10}$$

Where $\Im$ denotes Fourier transform and * the complex conjugate. Let $B(z,\omega)$ and $\varphi(z,\omega)$ be the amplitude and phase of $H(z,\omega)$ respectively. In a reverberant cavity, where the field can be approximated as being diffuse, one can consider that the amplitude is not a strong function of z. Under this assumption Eq. 3.10 can be written as:

$$\Im\left(C_{zz}(z_m, z_n, t)\right) = \left|E(\omega)B(\omega)\right|^2 \exp\left[i\left(\varphi(z_n,\omega) - \varphi(z_m,\omega)\right)\right]\exp\left(-2i\omega T\right) \tag{3.11}$$

Thus, the information about the spatial profile around the source position z_m is contained in the phase difference between the field evaluated at z_m and z_n. From the time reversal point of view, the interpretation is that all the incoming waves interfere constructively at the source position z_m weighted by a frequency dependent amplitude factor. When the field is evaluated at z positions other than z_m, the interference is not more constructive producing a decrease on the wave field amplitude. The frequency weighting factor of Eq. 3.11 implies that, only the most energetic frequency components of the wave field are used in constructing the spatial focus. The information contained in the spectrum of the wave field can be optimally used through a whitening process by giving the same weight factor to all frequency components. To this end, the following modified correlation matrix is computed after dividing Eq. 3.11 by its modulus and then taking the inverse Fourier transform:

$$\hat{C}_{zz}(z_m, z_n, t) = \Im^{-1}\left(\frac{|E(\omega)B(\omega)|^2 \exp\left[i(\varphi(z_n,\omega) - \varphi(z_m,\omega))\right]\exp(-2i\omega T)}{\left||E(\omega)B(\omega)|^2 \exp\left[i(\varphi(z_n,\omega) - \varphi(z_m,\omega))\right]\exp(-2i\omega T)\right|} \right) = \\ = \Im^{-1}\left(\exp\left[i(\varphi(z_n,\omega) - \varphi(z_m,\omega))\right]\exp(-2i\omega T)\right) \tag{3.12}$$

Constant phase factors depending on the signal length T can be suppressed since they only introduce a global shift in time. The final expression for the correlation matrix is therefore:

$$\hat{C}_{zz}(z_m, z_n, t) = \Im^{-1}\left(\exp\left[i(\varphi(z_n,\omega) - \varphi(z_m,\omega))\right]\right) \tag{3.13}$$

Since signal amplitude has been removed, Eq. 3.13 is referred to as phase correlation [70]. Throughout this manuscript symbol $\hat{C}$ will be used to denote phase correlation. No dependence on the emitted signal is observed. Equation 3.13 also ensures that all the information contained in the spectrum is optimally used because all the frequency components have the same weight. However, it is important to note that this approach is valid only within a given frequency bandwidth otherwise noise components will be amplified. In this work, a gate function $W(\omega_1, \omega_2)$ is used to select a desired bandwidth:

$$\hat{C}_{mn}(t) = \Im^{-1}\left(\exp\left[i(\varphi(z_n,\omega) - \varphi(z_m,\omega))\right]W(\omega)\right) \tag{3.14}$$

where W is given by:

$$W(\omega) = \begin{cases} 1 & \text{if} \quad \omega_1 \le \omega \le \omega_2 \\ 0 & \text{otherwise} \end{cases} \tag{3.15}$$

3.2.3 Application to elastography: the focal width and phase methods

As I stated earlier on this section, from the time reversal point of view, there are two independent ways of measuring the shear wave speed. The first method consists in measuring the wave speed as the wave converges, which will be called the phase method. The second method consists in measuring the focal width which is related to the shear wave length through Rayleigh criteria: the focal width method.

In the work of *Catheline et al.* [2] the two dimensional spatial-temporal focusing was observed using the same experimental setup shown in Fig. 3.3. This was done by moving the transducer along the x-axis by a 2.5 mm step. The correlation matrix was calculated using Eq. 3.8. In Fig. 3.5 four instants around the temporal focusing (chosen as origin) where selected. A converging wave at time -6 ms and a diverging wave at time +6 ms and +9 ms as well as the spatial-temporal focusing at time 0 ms are clearly visibly. It is very important to note that the focusing process does not present the same symmetric features of time reversal in scalar fields issued from a simple source: the time reversed energy is not homogeneously distributed on circles. As a result, a non axis symmetric refocusing spot is found at time 0 ms. It was found empirically that the -6 dB width along the z-axis is 1.6 time bigger than along the x-axis, this latter value being very close to the shear half a wavelength. This leads to a direction dependent Rayleigh criteria for the case of elastic fields, having direct consequences on the shear wave speed estimation through the shear wavelength estimation in the focal width method. I will come back to this issue later on this manuscript (section 3.3.1), where the exact relationship between the focal size and the shear wavelength for a given amplitude level is found based on Green function retrieval from cross-correlation of elastic fields.

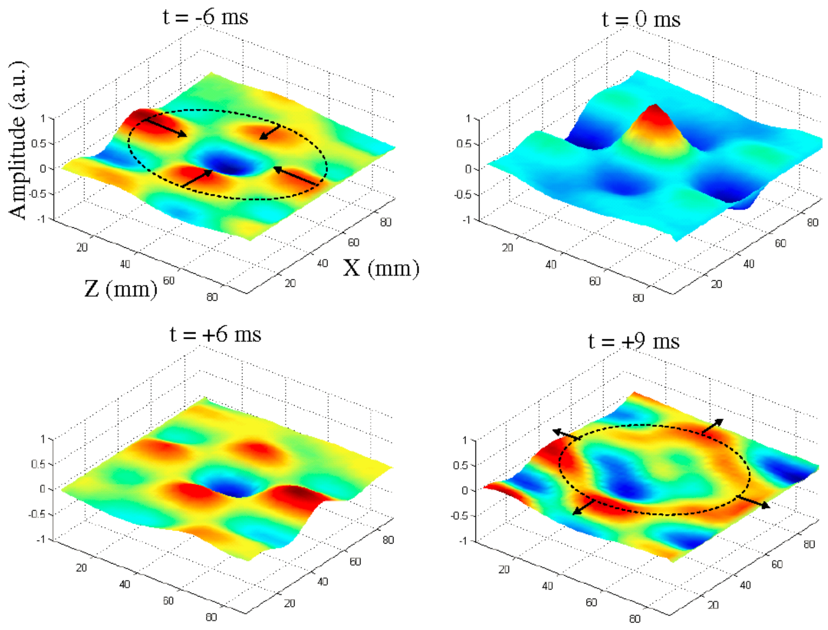

Fig. 3.5 Two dimensional focalization calculated using cross-correlation. The spatial temporal focalization is clearly visible. It is important to notice the ellipse like shape of the focal spot contrary to the scalar wave field. **Source:** ***Catheline et al.*** **[2]**

In the work of *Benech et al.* [3], the shear elasticity of an homogenous gelatin based phantom was retrieved using the phase and focal width method. An optimized use of the temporal frequencies was achieved by calculating the correlation matrix using phase correlation (Eq. 3.14). The result is the spatial-temporal refocusing field shown in Fig. 3.6. The cross like shape in Fig. 3.6 is a one dimensional representation of a converging field ($t < 0$) that focuses at $t = 0$ and then diverges ($t > 0$). The phase method consists in computing the phase of each branch of the cross shaped field of Fig. 3.6 from a Fourier transform as function of z. When divided by the angular frequency, it gives the time-of-flight of the time reversed field at that particular frequency.

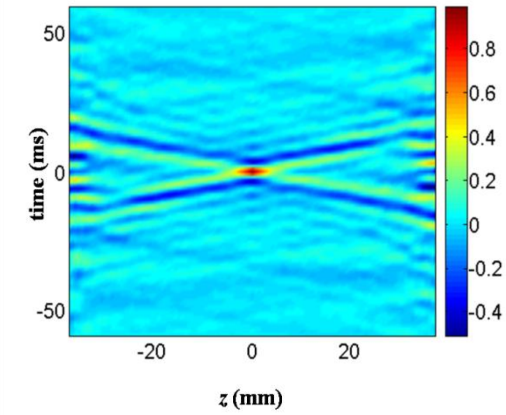

Fig. 3.6 Spatial and temporal focusing of the correlation field using Eq. 3.14. The cross indicates a converging spherical wave (t < 0) that focuses at z = 0 where a maximum amplitude is observed and then diverges (t > 0). **Source:** ***Benech et al.*** **[3]**

An alternative and independent way to estimate the elasticity value consists in measuring the -6 dB width of the spatial focusing: Δz. As described before, the Rayleigh criterion in an elastic solid is direction dependant. At -6 dB, $\Delta z \approx 1.6\Delta x \approx \lambda_s$, being λ_s the shear wavelength. Since the final objective is to calculate the shear wave speed, the following question arises: what is the temporal frequency corresponding to this measured shear wave length? In the work of *Benech et al.* [3], it was assumed that the highest frequency of the gate function corresponds to the measured shear wavelength. This assumption will be later justified at the end of section 3.3.1.

Finally through both methods, the same shear wave speed estimation was retrieved. The focal width method present two main advantages respect to the phase method: it is compatible with low sampling frequencies and it is less sensitive to low signal to noise ratio. The first advantage allows thinking of the use of standard electronics such as echographic devices (~40 Hz frame rate) for elasticity measurements. This advantage will be exploited later in section 3.3.3. The second advantage can be interpreted from a signal analysis point of view: time reversal process is a spatial-temporal matched filter and thus has the best signal to noise ratio on the source location at the refocusing time. Consequently, the refocusing is likely to emerge from the reverberant field and its -6dB width estimation is possible. Now, from a wave point of view, it corresponds to the situation of maximum energy density, when the focused wave concentrates on its source. Elsewhere, the classical $1/r$ amplitude decreasing law ($1/r^2$ for the near field shear wave) implies that the wave rapidly disappears within the fluctuation of a random phase reverberating field. As a consequence, phase measurements are not possible.

3.3: Shear elasticity estimation from noise correlation

In the previous sections, the basic concepts for TRE experiments were presented by introducing one channel time reversal elastography. In this section, a step forward is taken, since the goal is to use a very complex elastic wave field produced by a random spatial and temporal source distribution to conduct some passive elastography experiment based on the focal width approach.

First, in order to validate the technique, *in vitro* experiments on a bi-layer tissue mimicking phantom made of PVA-C are performed. The experimental setup is shown in Fig. 3.7(a). Each layer was previously characterized using 1D transient elastography. A shear wave speed of 1.4 ± 0.1 m/s and 3.7 ± 0.2 m/s was found for the top and bottom layer respectively.

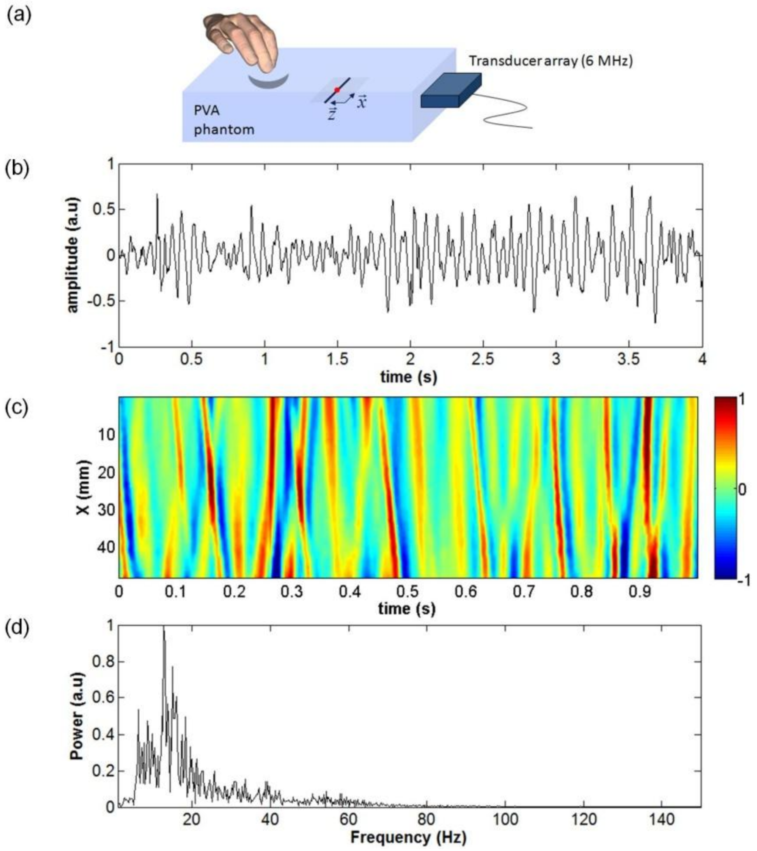

Fig. 3.7 (a) Experimental set-up for the *in vitro* experiments. A PVA-C soft solid is submitted to multiple finger impacts creating a complex elastic field. (b) Measured field as function of time at an arbitrary position (x,z) in the imaging plane. (c) A zoom of the displacement field on one line of the imaging plane where the brouhaha caused by finger impacts and reverberation is clearly visible. (d) Displacement power spectrum. The low frequencies components clearly dominate the field.

The first step in a time reversal experiment consists in recording the forward wave scene. A low-frequency random-like displacement field is generated by finger impacts given randomly all over the phantom accessible surface. One component (along z direction) of the complex elastic field on the (x, z) plane is measured by a standard speckle tracking technique using a 64 elements, 6 MHz central frequency ultrasonic linear array and an ultrafast scanner (Lecoeur Electronique, France). Two types of experiments were carried out. An "ultrafast" experiment were the acquisition rate was set to 1000 Hz and an "ultraslow" experiment with an acquisition rate of 10 Hz. This latter was carried out in order to highlight the robustness of the focal width method for low frequency elasticity imaging. In each experiment, long duration signals of approximately 5 seconds duration were acquired. This was enough time to cover most of the surface with finger impacts acting as randomly activated sources. Fig. 3.7 (b) displays the field as function of time at an arbitrary position (x, z) in the imaging plane. A zoom of the displacement field on one line of the imaging plane (Fig. 3.7 (c)) clearly shows the elastic brouhaha caused by finger impacts and reverberation.

The second step consists in selecting one line of the displacement field and correlated to the others resulting in a two dimensional focus. In Fig. 3.8(a) the B-Mode image of the bi-layer phantom is presented. The interface between both layers generates the echoes observed around z ≈ 35mm. On the right, a two dimensional representation of the normalized displacement field calculated by means of Eq. 3.14 at the focalization time $T = 0$ is presented. The focal spot obtained in the soft and in the hard part with its -6db contour are presented in Fig. 3.8 (b) and (c) respectively. Two facts are important to be noted. First, the focal spot clearly appears bigger in the hard medium, which logically follows from the elastic properties of each part. Second, there is a direction dependent Rayleigh criteria as it was described in the previous sections. In order to estimate the shear wave speed the relationship between the focal width and the shear wavelength should be established. For this purpose, it is necessary to introduce the Green's function retrieval from cross-correlation in the case of elastic fields.

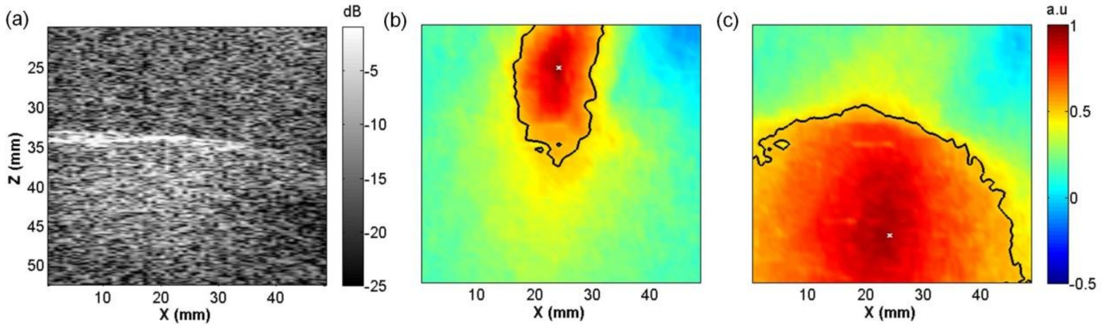

Fig. 3.8 (a) B-mode image of the bi-layer phantom. The interface between both layers is hardly visible around z ≈ 35 mm. The spatial focusing in the soft part (b) and in the hard part (a) with its -6 dB contour in black are also presented. The white cross indicates the focalization point. The focal size is bigger in the hard part which logically follows from the elastic properties of each part.

3.3.1 Towards quantitative elasticity estimation using Time Reversal Elastography

In this section, an analytical expression for the spatial focalization in the general case of a vectorial wave field in an elastic solid is derived. In a second step, based on the derived relation, an analytical formula which relates the focal spot size at a given isolevel curve, the frequency bandwidth used for phase correlation computation and the tissue's elasticity is derived in the particular case of a soft solid. This analytical expression will allow in the following sections to retrieve a quantitative shear wave speed estimation from the focal width measurement.

In section 3.2.2 the relationship between cross-correlation and time reversal was established from a liner system point of view through the impulse response $h_{jz}(t)$. However, in order to obtain the relationship between the shear wavelength and the focal width, a more physical approach is needed. The link between the linear system point of view and physics lies in the elastodynamic Green function.

Let's consider a lossless elastic medium, free of body sources, occupying a volume V enclosed by a surface S. The Green's function $G_{mn}(\vec{r}',\vec{r},\omega)$ is the displacement at $\vec{r}$ along direction n produced by a unit harmonic simple source acting at $\vec{r}'$ along direction m. By making use of the representation theorem of the correlation type for systems with time-reversal symmetry [71], [72], the imaginary part of the Green's function between two arbitrary points $\vec{r_1}$ and $\vec{r_2}$ within the volume V can be related to the boundary values of traction and displacements at the closed surface S (the ω dependence is understood and is not written in what follows):

$$-\int_S \left[G_{mj}(\vec{r}_1,\vec{R})T^*_{jn}(\vec{R},\vec{r}_2)-G^*_{nj}(\vec{r}_2,\vec{R})T_{jm}(\vec{R},\vec{r}_1)\right]dS = G_{mn}(\vec{r}_1,\vec{r}_2)-G^*_{mn}(\vec{r}_1,\vec{r}_2) \tag{3.16}$$

Where $T_{jm}(\vec{R},\vec{r_1})$ is the traction at a point $\vec{R}$ on the surface S acting along direction j produced by the a unit harmonic simple source acting at $\vec{r_1}$ along direction m. In Eq. 3.16 a volume integral is not included because a lossless medium free of body sources is assumed. The active sources are placed only on the enclosing surface S as in the case of the experimental configuration. This equation expresses a perfect time-reversal cavity for a homogeneous elastic medium within the boundary S [72]. The right-hand side can be interpreted as a superposition of the response at $\vec{r_2}$ due to a simple source at $\vec{r_1}$ and its time-reversed version in the frequency domain. If $\vec{r_2}$ is a varying point, in the time domain, Eq. 3.16 is the representation of a focusing field that converges at $\vec{r_1}$ and then diverges. Thus, the point $\vec{r_1}$ can be considered as a virtual source embedded in the medium.

Under ideal conditions, where the energy flux of the elastic field is equal in all directions, the left-hand side of Eq. 3.16 is the time derivative of the spatial average of the cross-correlation field over all sources and/or observing points [71]. A field obeying the above condition is usually termed as equipartitioned [73], [74]. The concept of equipartition is taken from statistical physics. It states that the energy of a system in thermal equilibrium is shared equally among all of its independent degrees of freedom. For example, from a classical point of view, each atom in a crystalline solid can be considered as an independent oscillator which can oscillate in three independent directions. Thus, the solid can be viewed as a system of $3N$ independent simple harmonic oscillators, where N denotes the number of atoms in the lattice. Since each harmonic oscillator has average energy k_BT, due to the equipartition principle, the average total energy of the solid is $3Nk_BT$, being k_B the Boltzmann constant and T the absolute temperature. This concept can be extended to a wave field in a cavity, where the energy is equally distributed over the different modes of vibration of the cavity.

The condition of an equipartitioned field is difficult to be ensured in practice. As it was introduced in section 3.1, in many experimental situations, there are mainly two ways to create such field. One way is the field created by a small number of sources (eventually only one) within a multiple scattering medium. After a large time, the field can be considered as being equipartitioned. The complexity of the field comes from the propagation equation since every scatterer has to be taken into account. Statistical representations are usually used to describe the wave field. Typical examples of this kind of field are the seismic coda [75] or the field inside a highly reverberating medium [76], [77].

Another way is the field generated by multiple uncorrelated random sources in a homogeneous or slowly varying medium. This latter being the case of the experiments presented in this thesis. Contrary to a multi-scattered wave field, in such case the wave equation for each source is simple and is almost composed of direct waves. The complexity of the field arises due to the interference between waves coming from the multiple uncorrelated sources. As example of this kind of field, the thermal fluctuations on a solid cavity [78] or the field created by ambient noise sources [79] can be mentioned. The field in the experiments considered in this thesis is assumed to be equipartitioned, meeting the conditions for Green's function retrieval by cross-correlation. Thus based on Eq. 3.16 the following relation between the correlation-field and the Green function can be expressed [71]:

$$i\omega\langle\tilde{C}_{mn}(\vec{r}_1,\vec{r}_2)\rangle = G_{mn}(\vec{r}_1,\vec{r}_2) - G^{*}_{mn}(\vec{r}_1,\vec{r}_2) \tag{3.17}$$

Where the average field $\langle\tilde{C}_{mn}(\vec{r}_1,\vec{r}_2)\rangle$ in our experiments is computed over a set of virtual sources located at different locations $\vec{r}_2$ based on Eq. 3.14. The tilde $\sim$ denotes the correlation-field for a given frequency component ω. In our experiments, the data is collected in the time domain, where a multiplication by $i\omega$ implies a time derivative. Taking the time derivative in experimental data is usually avoided due to the introduction of undesirable numerical noise on the signal processing. It has been shown that, for finite bandwidth signals, the correlation and its time derivative only differ from a constant phase change [80]. Thus, the correlation field will be used instead of its time derivative. Since in the experiments only the z component of the displacement field at position $\vec{r} = (x, z)$ is accessible, attention will be focused in the relationship between $\tilde{C}_{zz}(\vec{r}_1,\vec{r}_2)$ and $G_{zz}(\vec{r}_1,\vec{r}_2)$. Due to space reciprocity, the measuring point can be considered as a virtual source acting along the z direction.

Without loss of generality it can be considered $\vec{r}_1 = 0$ as the origin of the coordinate system and $\vec{r}_2 = \vec{r}$ as an arbitrary point within the volume V. Given the nature of the experiments described in the previous section, the free space Green´s function will be used as a first approximation to the problem. The Green's function for an isotropic elastic solid with shear wave speed c_T and longitudinal wave speed c_L is given by [81]:

$$\begin{aligned}G_{mn}(\vec{0},\vec{r}) &= \frac{1}{4\pi\rho {c_L}^2}\frac{\gamma_m\gamma_n}{r}e^{iqr} + \frac{1}{4\pi\rho {c_T}^2}\frac{\delta_{mn}-\gamma_m\gamma_n}{r}e^{ikr} + \\ &+ \frac{1}{4\pi\rho}\frac{3\gamma_m\gamma_n-\delta_{mn}}{r^3}\left[\frac{e^{ikr}}{i\omega}\left(\frac{r}{c_T}-\frac{1}{i\omega}\right)-\frac{e^{iqr}}{i\omega}\left(\frac{r}{c_L}-\frac{1}{i\omega}\right)\right]\end{aligned} \tag{3.18}$$

Where $q = \omega/c_L$ is the longitudinal wavenumber, $k = \omega/c_T$ is the shear wavenumber,$|\vec{r}| = r$ and $\gamma_i = \partial r/\partial x_i = x_i/r$ are the cosine directors. The first two terms of this expression are classical far-field terms. The particle motion direction of the first term is parallel to the wave propagation direction while for the second term those directions are perpendicular to each other, representing a longitudinal and a transversal wave respectively. The third term in Eq. 3.18 is termed the near-field term and it is composed of both: longitudinal and transverse motions. Due to its rapid attenuation with distance from the source, this term is usually not considered in Green's function retrieval. However, it plays an important role in spatial focalization as it will be shown below. The time reversal field of Eq. 3.16 can then be written as:

$$\operatorname{Im}\left[G_{mn}(\vec{0},\vec{r})\right]=\frac{k}{4\pi\mu}\left\{\left[\frac{\sin(kr)}{kr}+\frac{\cos(kr)}{(kr)^2}-\frac{\sin(kr)}{(kr)^3}+\left(\frac{c_T}{c_L}\right)^3\left(\frac{\sin(qr)}{(qr)^3}-\frac{\cos(qr)}{(qr)^2}\right)\right]\delta_{mn}\right\}+ \\ +\frac{k}{4\pi\mu}\left\{\left[3\frac{\sin(kr)}{(kr)^3}-\frac{\sin(kr)}{kr}-3\frac{\cos(kr)}{(kr)^2}+\left(\frac{c_T}{c_L}\right)^3\frac{\sin(qr)}{qr}\right]\gamma_m\gamma_n\right\} \tag{3.19a}$$

Or equivalently,

$$\operatorname{Im}\left[G_{mn}(\vec{0},\vec{r})\right]=\frac{k}{12\pi\mu}\left\{\begin{array}{l}\left[\left(\frac{c_T}{c_L}\right)^3\left(j_0(qr)+j_2(qr)\right)+2j_0(kr)-j_2(kr)\right]\delta_{mn} \\ +\left[3j_2(kr)-3\left(\frac{c_T}{c_L}\right)^3 j_0(qr)\right]\gamma_m\gamma_n\end{array}\right\} \tag{3.19b}$$

Where $Im[\,]$ expresses the imaginary part of the quantity between brackets. To convert Eq. 3.19(a) into Eq, 3.19(b) the following identities in terms of the spherical Bessel function of the first kind $j_n(y)$ were used:

$$\frac{\sin(kr)}{kr}+\frac{\cos(kr)}{(kr)^2}-\frac{\sin(kr)}{(kr)^3}=\frac{1}{3}\left[2j_0(kr)-j_2(kr)\right] \tag{3.20a}$$

$$\frac{\sin(qr)}{(qr)^3}-\frac{\cos(qr)}{(qr)^2}=\frac{1}{3}\left[j_0(qr)+j_2(qr)\right] \tag{3.20b}$$

Equation 3.19 represents the theoretical spatial focalization for bulk elastic waves at a fixed frequency. An alternative way of obtaining Eq. 3.19 is based on the superposition of equipartitioned plane shear and longitudinal waves coming from all directions [82]. It is worth noticing that Eq. 3.19 is not as simple as in the scalar field case. However, it can be simplified if the field and source are oriented in the same direction.

In order to compare it with the experimental correlation field, the case where $m = n = z$ will be considered. The resulting field is axis-symmetric around the z-axis, depending only on the distance r and the inclination or polar angle θ. For this case, $\gamma_m = \gamma_n = \cos(\theta)$ and $\delta_{mn} = 1$. Therefore, Eq. 3.19(b) can be written as:

$$\mathrm{Im}\left[G_{zz}(\vec{0},\vec{r})\right]=\frac{k}{12\pi\mu}\left\{\begin{array}{l}\left(\dfrac{c_T}{c_L}\right)^3\left(j_0(qr)+j_2(qr)\right)+2j_0(kr)-j_2(kr)+\\+\left[3j_2(kr)-3\left(\dfrac{c_T}{c_L}\right)^3 j_0(qr)\right]\cos^2(\theta)\end{array}\right\} \tag{3.21}$$

In Fig. 3.9 a comparison between the theoretical and the experimental correlation fields is presented. The experiment was carried out (as described earlier on this section) on a homogeneous PVA-C phantom with a shear wave speed of 2.4 ± 0.1 m/s. A longitudinal wave speed of 1500 m/s was assumed as usual for this kind of phantoms. The experimental observation plane was composed of 64 points in the x-direction and 39 points in the z-direction representing an imaging surface of 30 x 40 mm^2. The experimental correlation field was computed using phase correlation with a frequency bandwidth ranging from 20 Hz to 80 Hz. For Fig. 3.9 a spatial averaging over different focal points was performed.

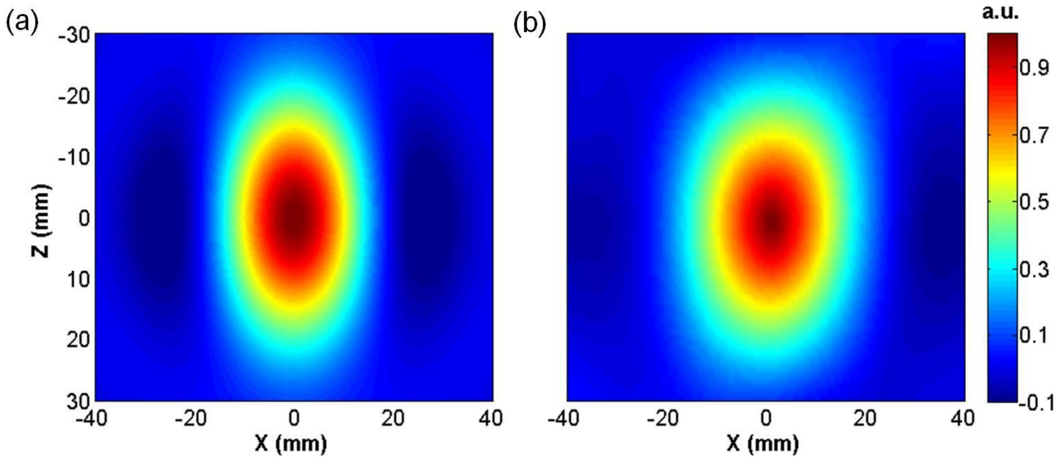

Fig. 3.9 Spatial focusing of the correlation field: (a) theory and (b) experiment. For construct the theoretical image, the shear wave speed was set to 2.4 m/s and a whitening process to give the same weight to each frequency as in the experimental case was used.

The theoretical field was constructed with the same frequency content as the experimental field and using the same whitening process. The spatial focalization for each frequency was computed using Eq. 3.21. Then they were summed up and the final result was normalized to 1. It is important to note the similarity between theory and experience. Another important aspect in Fig. 3.9 is that the spatial focalization is not symmetric with respect to the polar angle as it was already described in the work of *Catheline et al.* [2], presenting an ellipse-like shape with major axis oriented along the z direction. Thus, the original asymmetric directivity pattern of a simple source in an elastic medium is conserved in a time reversal experiment.

One way to obtain the shear wavelength from the focal width is to find the values of q and k which best fit the experimental data based on Eq. 3.21. But this procedure is very time consuming from the computational point of view. A numerically "cheaper" method is based in the knowledge that the focal spot width is limited by the shear wavelength. Thus, the goal in the following paragraphs, is to find an expression relating the isolevel curve around the focusing point with the shear wavelength. In order to study the spatial focusing analytically, the following asymptotic expressions of $j_0(y)$ and $j_2(y)$ as $y \to 0$ to second order in y will be used:

$$j_0(y) \approx 1-\frac{y^2}{6} \tag{3.22a}$$

$$j_2(y) \approx \frac{y^2}{15} \tag{3.22b}$$

Therefore, expression Eq. 3.21 becomes:

$$\chi(r,\theta)=\frac{k}{12\pi\mu}\left\{\left(\frac{c_T}{c_L}\right)^3\left[1-\frac{(qr)^2}{10}\right]+2\left[1-\frac{(kr)^2}{5}\right]+\frac{1}{5}\left[(kr)^2-\left(\frac{c_T}{c_L}\right)^3(qr)^2\right]\cos^2(\theta)\right\} \tag{3.23}$$

The field in the above expression takes a maximum value of $\chi_{\max}=\left\lfloor 2+\left(c_T/c_L\right)^3\right\rfloor k/12\pi\mu$ at $r = 0$. The interest now is to find the distance r_L from the focal point at which the field takes a fraction $L < 1$ of its maximum value. Thus:

$$\frac{k}{12\pi\mu}\left\{\left(\frac{c_T}{c_L}\right)^3\left[1-\frac{qr_L}{10}\right]+2\left[1-\frac{(kr_L)^2}{5}\right]+\frac{1}{5}\left[(kr_L)^2-\left(\frac{c_T}{c_L}\right)^3(qr_L)^2\right]\cos^2(\theta)\right\}=L.\chi_{\max} \tag{3.24}$$

After some computation and using the fact that $q/k = c_T/c_L$ it is found that:

$$r_L=\frac{\pm\lambda_s}{2\pi}\sqrt{\frac{5(1-L)\left[\left(c_T/c_L\right)^3+2\right]}{2-1/2\left(c_T/c_L\right)^5-\cos^2(\theta)\left[1-\left(c_T/c_L\right)^5\right]}} \tag{3.25}$$

As a result from Eq. 3.25 the focal size $\Delta(\theta) = 2r_L(\theta)$ is not symmetric with respect to the polar angle. This asymmetry, already observed experimentally in soft solids, is generalized here to any elastic solid. It can be quantified by introducing the asymmetry ratio R_Δ between the focal width along the z direction $\Delta_z = \Delta(\theta = 0)$ and the lateral focal width $\Delta_x = \Delta(\theta = \pi/2)$. Based on Eq. 3.25 this ratio is independent of the value of L and is given by:

$$R_\Delta = \frac{\Delta_z}{\Delta_x} = \sqrt{\frac{4-(c_T/c_L)^5}{2+(c_T/c_L)^5}} \tag{3.26}$$

The asymmetry ratio depends only on the ratio between the shear and longitudinal wave speeds, being directly linked to the Poisson's ratio ν of an elastic solid defined as:

$$\nu = \frac{1}{2}\left[\frac{1-2(c_T/c_L)^2}{1-(c_T/c_L)^2}\right] \tag{3.27}$$

Theoretical limits for the Poisson's ratio within the situation considered in this work are $\nu_{min} = 0$ corresponding to $c_T/c_L = 1/\sqrt{2}$ and $\nu_{max} = 1/2$ when $c_T/c_L \ll 1$. Therefore, the limits for the asymmetry ratio R_Δ are $R_\Delta^{min} \cong 1.32$ and $R_\Delta^{max} \cong \sqrt{2}$ respectively.

Since all the experiments carried out during this thesis were done in soft solids ($c_T/c_L \ll 1$), the attention below will be placed in estimating the shear wavelength from the experimental focal size in this particular case. To this end, Eq 3.25 is adapted to give the θ-dependence of r_L for the soft-solid case:

$$r_L(\theta) \cong \frac{\lambda_s}{2\pi}\sqrt{\frac{10(1-L)}{2-\cos^2(\theta)}} \tag{3.28}$$

This is the expression for an ellipse in polar coordinates with major and minor semi-axis a and b given by: $a = r_L(\theta = 0) = \sqrt{10(1-L)}\lambda_s/2\pi$ and $b = r_L(\theta = \pi/2) = \sqrt{10(1-L)}\lambda_s/(2^{3/2}\pi)$.

In this thesis two different approaches for retrieving the shear wave speed from the focal size will be used. The first approach consists in computing the surface enclosed by a given isolevel curve by integrating Eq. 3.28 in the polar angle and distance:

$$A_f = \int_0^{2\pi}\int_0^{r_L} r(\theta)\,dr\,d\theta = \frac{10(1-L)\lambda_s^2}{8\pi^2}\int_0^{2\pi}\frac{d\theta}{2-\cos^2(\theta)} = \frac{5(1-L)\lambda_s^2}{4\pi^2} I \tag{3.29}$$

The integral I in Eq. 3.29 can be found to be $I = \sqrt{2}\pi$. Thus, the relation between the surface enclosed by a given isolevel curve and the shear wave speed is finally:

$$A_L = \frac{5(1-L)\sqrt{2}}{4\pi}\lambda_s^2 = \frac{5(1-L)\sqrt{2}}{4\pi}\frac{c_T{}^2}{f^2} \Rightarrow c_T = f\sqrt{\frac{4\pi}{5(1-L)\sqrt{2}}A_L} \qquad (3.30)$$

The second approach consists in computing the mean radius from the focal spot to the given isolevel curve (contour measurement) as follows:

$$\bar{r}_L = \frac{1}{2\pi}\int_0^{2\pi} r_L(\theta)d\theta = \frac{\lambda_s}{(2\pi)^2}\sqrt{10(1-L)}\int_0^{2\pi}\frac{1}{\sqrt{2-\cos^2(\theta)}}d\theta = \frac{\lambda_s}{(2\pi)^2}\sqrt{10(1-L)}.I_o \qquad (3.31)$$

Where the integral I_o was numerically evaluated to be $I_o \cong 5.2441$. Finally, the following relation between mean radius and the shear wave speed is obtained:

$$\bar{r}_L = \frac{\sqrt{10(1-L)}.I_o}{(2\pi)^2}.\frac{c_T}{f} \Rightarrow c_T = \frac{4\pi^2}{I_o\sqrt{10(1-L)}}.f.\bar{r}_L \qquad (3.32)$$

The surface/mean radius given in the above expressions Eq. 3.30 and Eq. 3.32, were computed for a single frequency, however, the signals in the experiments are usually composed of multiple frequencies within the bandwidth $\Delta f = f_{max} - f_{min}$. Thus, in order to calculate the surface/mean radius related to a given isolevel curve, the resulting focalization due to the presence of multiple frequencies should be first established. For this purpose, let us consider Eq. 3.23 in the particular case of a soft solid ($c_T \ll c_L$):

$$\chi(r,\theta,\omega) = \frac{1}{12\pi\mu}\frac{\omega}{c_T}\left\{2\left[1-\frac{(\omega.r)^2}{5.c_T{}^2}\right]+\frac{1}{5}\left(\frac{\omega.r}{c_T}\right)^2\cos^2(\theta)\right\} \qquad (3.33)$$

In Eq. 3.33 the wave number k was substituted by ω/c_T being $\omega = 2\pi f$. If each frequency is weighted by a factor $\mathrm{W}(\omega)$ an average spatial focalization $\bar{\chi}(r,\theta)$ can be computed over the given frequency bandwidth as:

$$\bar{\chi}(r,\theta) = \frac{1}{\int_{\omega_{\min}}^{\omega_{\max}} \mathrm{W}(\omega)d\omega}\int_{\omega_{\min}}^{\omega_{\max}} \mathrm{W}(\omega).\chi(r,\theta,\omega).d\omega \qquad (3.34)$$

By calculating the mean surface A_L or the mean radius R_L from Eq. 3.34 a shear wave speed estimation can be obtained for the given frequency bandwidth. In the case of normalized cross-correlation, the weighting function is given by the squared power spectrum of the recorded signal (Eq. 3.10). On the other hand, for phase correlation (Eq. 3.14) each frequency has the same weight in the correlation spectrum, corresponding to a rectangular weighting function. By applying Eq 3.34 for the case of a rectangular function whose value is one within the given frequency bandwidth and zero elsewhere the following mean focalization is obtained:

$$\bar{\chi}(r,\theta) = \frac{1}{12\pi\mu}\left\{\frac{2}{\omega_{max}-\omega_{min}}\left[\frac{1}{2}\frac{\omega_{max}^2-\omega_{min}^2}{c_T} - \frac{r^2}{20c_T^3}\left(\omega_{max}^4 - \omega_{min}^4\right)\right] + \frac{r^2}{20c_T^3}\cos^2(\theta)\left(\frac{\omega_{max}^4-\omega_{min}^4}{\omega_{max}-\omega_{min}}\right)\right\} \tag{3.35}$$

Equation 3.35 corresponds to the spatial focalization obtained through phase correlation. Based on Eq. 3.35 the distance r_L from the focal point at which the field takes a fraction $L < 1$ of its maximum value can be calculated as:

$$r_L = c_T\sqrt{\frac{20(1-L)}{\omega_{max}^2+\omega_{min}^2}}\cdot\frac{1}{\sqrt{2-\cos^2(\theta)}} \tag{3.36}$$

Now, a closed formula relating the shear wave speed and the surface/radius enclosed for a given contour level L can be expressed by integrating Eq. 3.36 in the polar angle θ:

$$c_T = \sqrt{\frac{4\pi}{5(1-L)\sqrt{2}}\mathrm{A}_L}\cdot\sqrt{\frac{f_{\max}^2 + f_{\min}^2}{2}} \tag{3.37}$$

$$c_T = \frac{4\pi^2}{\sqrt{10(1-L)}I_o}R_L\sqrt{\frac{f_{\max}^2 + f_{\min}^2}{2}} \tag{3.38}$$

The above expressions will be used in the following sections and Chapters for retrieving a quantitative shear wave speed estimation from a time reversal experiment when using phase correlation. The difference between Eqs. 3.37 and 3.38 and Eqs. 3.30 and 3.32 (which are for a single frequency) is that the frequency in Eqs. 3.30 and 3.32 is substituted by an effective frequency equal to $\sqrt{f_{\max}^2 + f_{\min}^2}/\sqrt{2}$. Thus, for phase correlation the spatial focalization can be interpreted as being dominated by only one effective frequency component which takes into account the effect of having multiple frequency components in our time reversed field. This effective frequency corresponds to the frequency root mean square as it will be shown below.

The root mean square (RMS), also known as quadratic mean, is a statistical measure of the magnitude of a varying quantity. RMS is used in various fields, most commonly from its application in electrical engineering for calculating the effective voltage, intensity or power. The frequency root mean square is defined in general as:

$$f_{eff}^2 = \int_{f_{min}}^{f_{max}} f^2\, g(f)df \tag{3.39}$$

Where $g(f)$ is a normalized weighting function, i.e. $\int_{f_{min}}^{f_{max}} g(f)df = 1$. From Eq. 3.33, which corresponds to the spatial focalization for a unique frequency, it can be observed that each spatial focalization is multiplied by the frequency f, which can be interpreted as a "natural" weight. Higher frequencies will have a higher amplitude, contributing more to the average focalization. Thus, the following normalized weighting function is proposed for phase correlation:

$$g(f) = 2\frac{f}{f_{max}^2 - f_{min}^2} \tag{3.40}$$

By combining Eq. 3.39 and Eq. 3.40, a frequency root mean square of $\sqrt{f_{\max}^2 + f_{\min}^2}/\sqrt{2}$, which corresponds to the effective frequency defined by Eqs. 3.37 and 3.38, is obtained.

Under the assumption that $f_{max} \gg f_{min}$, the effective frequency defined from Eqs. 3.37 and 3.38 can be expressed as $f_{max}/\sqrt{2}$. Thus, in the presence of a large frequency band, the spatial focalization computed through phase correlation can be considered as dominated by the highest frequency of the band. This corroborates the aforementioned assumption made by *Catheline et al.* [2] and *Benech et al.* [3] where, in order to retrieve the shear wave speed from the focal width method, the highest frequency of the chosen band for phase correlation was used.

To conclude, depending on the experiment either Eq. 3.37 or Eq. 3.38 will be used. The main advantage in computing the mean surface rather than the mean radius is the use of all the spatial information available in the two dimensional focus. This procedure is more robust to noise than the radius computation estimation, however, it results in an underestimation on the shear wavelength near the imaging plane boundaries. The enclosed surface by a given isolevel curve for a focal point lying in the imaging plane boundary will be half the enclosed surface of focal point lying in the middle of the imaging plane. Thus, a reduction of the surface occurs the closer to the imaging plane boundary the focal point is. The distance in which this effect is appreciable will depend on the shear wavelength as well as the level L for which Eq. 3.37 is computed given a fixed bandwidth.

3.3.2 "Ultrafast" shear wavelength tomography

For the "ultrafast" experiment the displacement field created by finger impacts was imaged at 1000 Hz sampling frequency. One line of the displacement field at (x, z) is selected and correlated to the others. In this section the shear wave maps obtained by means of normalized correlation (Eq. 3.10) and phase correlation (Eq. 3.14) will be compared and discussed. For the results presented in this section, the mean radius will be used to retrieve the shear wave speed from the contour measurement.

- Shear wave speed map from normalized cross-correlation

In Fig. 3.10 the focal spots obtained using normalized cross-correlation (Eq. 3.10) are presented as well as the 0.9 contour level in black. It is worth noticing that the contour clearly appears bigger in the hard medium which logically follows from the elastic properties of each part.

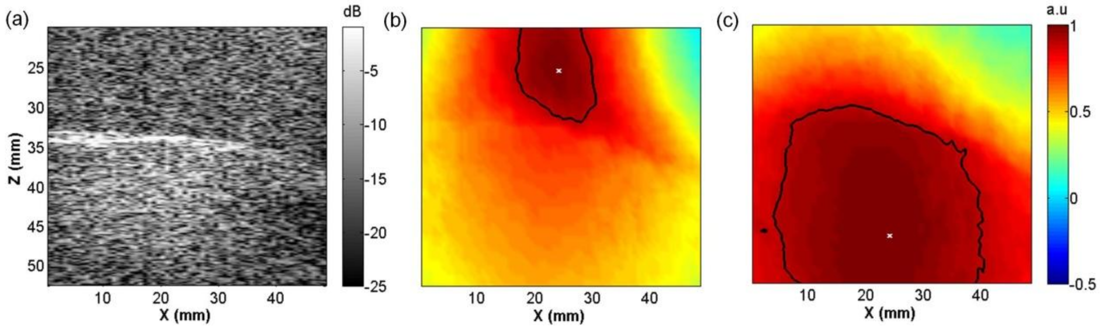

Fig. 3.10 (a) B-mode image of the bi-layer phantom. The interface between both layers is hardly visible around z ≈ 35 mm. The spatial focusing computed using normalized correlation and its 0.8 contour level in black are presented in (b) for the soft part and in (c) for the hard part. The white cross indicates the focalization point. Again the focal part is bigger in the hard part which logically follows from the elastic properties of each part.

In order to retrieve the shear wave speed from the spatial focalizations presented in Fig. 3.10 the relation between the mean radius and the shear wave speed should be established for the case of normalized correlation. For this purpose, the theoretical focalization was numerically computed by means of Eq. 3.34, for a fixed shear wave speed value, using as weighting function the square of the experimental spectrum presented in Fig. 3.7 (d). The choice of such a weighting function is justified in Eq. 3.11 by the fact that the normalized correlation spectrum depends on the square of the displacement spectrum. As spatial focalization for a given frequency, the exact expression for $\chi(r,\theta,\omega)$ given in Eq. 3.21 was used. Once the theoretical focalization is calculated, the mean radius is obtained for contour levels ranging from 0.8 to 0.99. The procedure is then repeated for different shear wave speed values.

The obtained relation between the mean radius and the shear wave speed is presented in Fig. 3.11 for different contour levels: 0.8, 0.9, 0.95 and 0.99 in triangles, squares, crosses and points respectively. A linear dependence is observed between the shear wave speed and the mean radius for a given contour level, depending the slope on the level chosen. Thus, by fitting a linear model the proportionality constant can be obtained and the shear wave speed can be retrieved given a measured mean radius. However, the latter calibration depends on the experimental spectrum. Thus, for different experiments different proportionalities constant could be expected. On the other hand, such a calibration for each experimental spectrum is very time consuming. Thus, is it possible to find an approximate empirical formula which relates the shear wave speed with the mean radius?

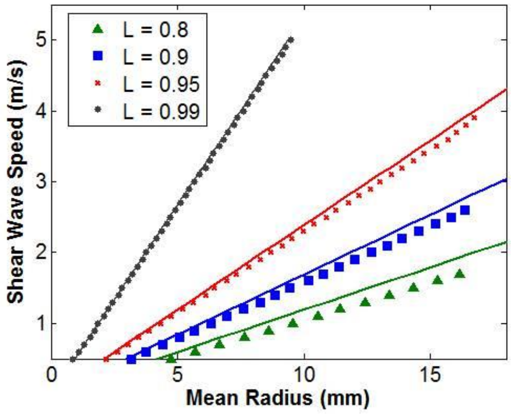

Fig. 3.11 Relationship between the shear wave speed and the mean radius computed from cross-correlation for different contour levels. The full lines represent the empirical model described by Eq. 3.41.

Inspired by the same reasoning used in deriving Eq. 3.32 for phase correlation, the following empirical formula is proposed for normalized correlation:

$$c_T = \frac{4\pi^2}{\sqrt{10(1-L)I_o}}.\overline{R}_L.f_{eff} \tag{3.41}$$

Where f_{eff} is an effective frequency which, as it will be shown in what follows, equals the frequency root mean square. However, since cross correlation is used, a different weighting function than the one proposed in Eq. 3.40 must be utilized. The proposed weighting function should take into account the fact that for normalized cross correlation, based on Eq. 3.11, the correlation spectrum depends on the square of the displacement spectrum. Thus, the following normalized weighting function is proposed:

$$g(f) = \frac{f.P(f)^2}{\int f.P(f)^2} \tag{3.42}$$

Where $P(f)$ is the mean displacement power spectrum. By combining Eqs. 3.39 and 3.42 an effective frequency of 22 Hz was numerically calculated for Fig. 3.11. The full straight lines presented in Fig. 3.11 were calculated for each contour level based on Eq. 3.41 using the calculated effective frequency. A good agreement between the proposed empirical formula and the computed data is observed. Again, this fact can be interpreted, in the case of normalized correlation, as the spatial focalization being dominated by only one effective frequency component corresponding to the frequency root mean square. In Fig. 3.11 a small relative deviation of up to 10% is observed for the lower contour levels and higher shear wave speed values. This can be explained based on the fact that Eq. 3.41 is only valid in the vicinity of the focal point, since for its deduction the asymptotic expressions of the spherical Bessel functions were used. The real focus is approximated by a parabola, being this approximation valid only near the focusing point or equivalently at higher contour levels.

For the experiments presented in this section, Eq. 3.41 will be used to construct the shear wave speed map from the mean radius measurement from normalized correlation. The measured effective frequency corresponds to 28.8 Hz for the experimental spectrum presented in Fig. 3.7(d). In Fig. 3.12 the shear wave speed maps obtained for different contour levels from 0.8 to 0.99 are presented. In all four cases, the two layers are clearly visible. Mean shear wave speed values of 1.75 ± 0.29 m/s and 3.75 ± 0.08 m/s, 1.59 ± 0.24 m/s and 3.85 ± 0.07 m/s, 1.49 ± 0.15 m/s and 4.00 ± 0.10 m/s , 1.22 ± 0.03 m/s and 3.86 ± 0.27 m/s were found for the top and bottom layer for a 0.8, 0.9, 0.95 and 0.99 contour level respectively. All the presented values agree within the error margin with the 1D transient elastography estimation.

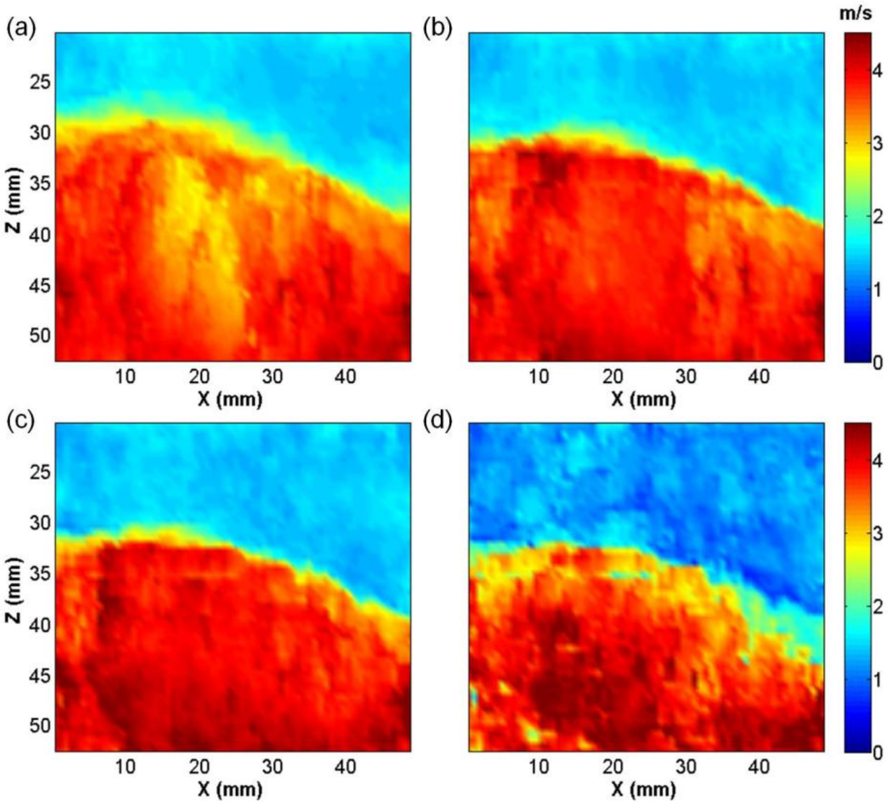

Fig. 3.12 Shear wave speed maps obtained using normalized correlation using different contour levels (a) 0.8 (b) 0.9 (c) 0.95 and (d) 0.99.

The final result is presented in Fig. 3.13 along with the B-mode image on the left. An average over all four contour levels was performed. Mean shear wave speed values of 1.51 ± 0.16 m/s and 3.87 ± 0.12 m/s were found for the top and bottom layer respectively again in good agreement with 1D transient elastography estimations. The border between both medium appears a little bit deeper in the B-Mode image than in the shear wave speed map. This can be explained based on the algorithm used in order to retrieve de shear wave speed from the mean radius measurement. A more detailed explanation of this phenomenon is given in Chapter IV, section 4.3.3.

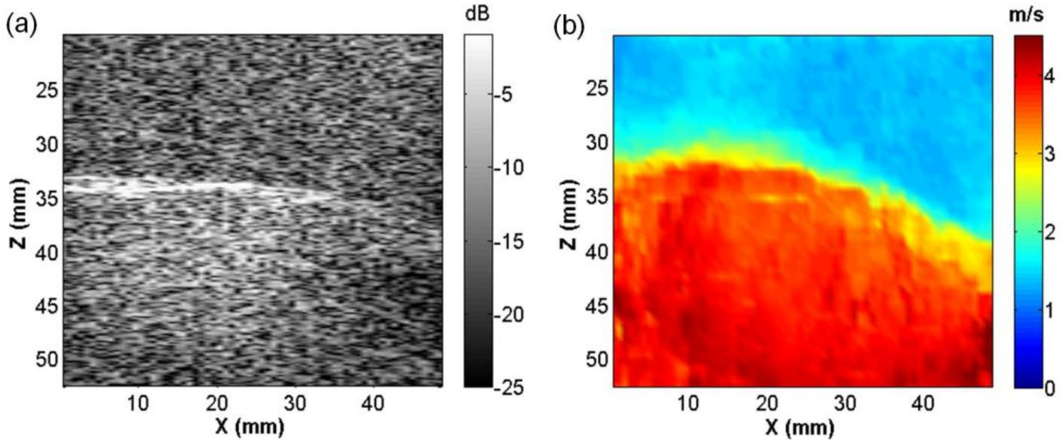

Fig. 3.13 Shear wave speed map from the focal width method using normalized cross correlation. The hard and the soft part are clearly visible in good agreement with the sonogram on the left. The obtained mean shear wave speed values for each part coincide with the ones obtained by transient elastography.

- Shear wave speed map from phase correlation

In this section, the shear wave speed maps will be retrieved through phase correlation by using Eq. 3.38. To compute the phase correlation, a frequency band between 10 to 70 Hz was chosen. The shear wave speed maps obtained for different contour levels from 0.6 to 0.8 are presented in Fig. 3.14 (a), (b) and (c) respectively. In all four cases the two layers are clearly visible. Mean shear wave speed values of 1.69 ± 0.08 m/s and 4.18 ± 0.08 m/s, 1.52 ± 0.02 m/s and 3.81 ± 0.07 m/s, 1.35 ± 0.03 m/s and 3.46 ± 0.13 m/s were found for the top and bottom layer for a 0.6, 0.7 and 0.8 contour level respectively. All the values agree within the error margins, with the independent transient elastography estimation and the obtained values through normalized cross-correlation. However, a small increment on the mean shear wave speed for each layer is observed as the contour level decreased.

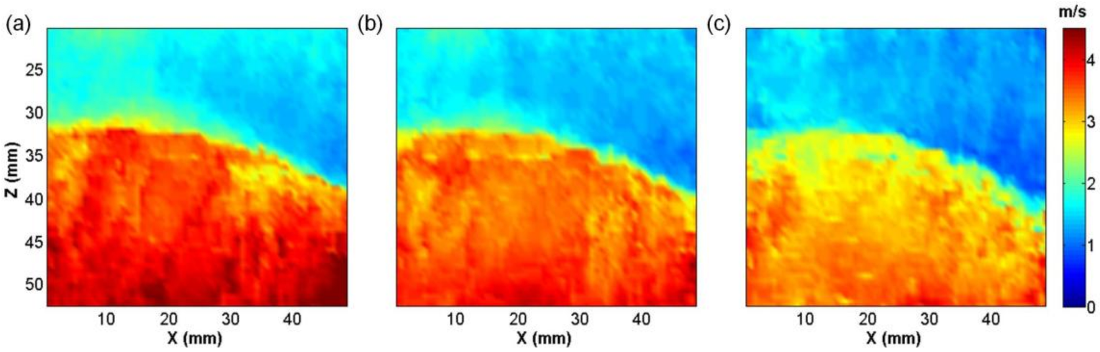

Fig. 3.14 Shear wave speed maps obtained using phase correlation for different contour levels (a) 0.6 (b) 0.7 (c) 0.8.

This overestimation on the shear wave speed for low contour levels can be attributed to the fact that Eq. 3.38, used to calculate the shear wave speed from the mean radius, is deduced from an approximate expression (Eq. 3.23) of the spatial focalization given in Eq. 3.21. In Eq. 3.23 the theoretical spatial focusing is approximate by a two dimensional parabola, based on the assumption that $r \to 0$, which is equivalent to higher contour levels. To evaluate the magnitude of this overestimation, the theoretical spatial focus was calculated by summing up the spatial focus for each frequency given by Eq. 3.21. The theoretical spatial focalization was constructed using the same frequency band as the experimental spatial focus. Then, the retrieved shear wave speed value through Eq. 3.38 was compared to the shear wave speed value used to calculate the theoretical spatial focalization. In Fig 3.15, the relative deviation is presented as a function of the contour level. The relative deviation is calculated as $(c_T^{mes} - c_T)/c_T$, where c_T^{mes} is the shear wave speed retrieved using Eq. 3.38. A relative deviation of ≈ 6% from the expected value is observed for the 0.6 contour level. Thus, if lower levels are used in order to retrieve the shear wave speed, this error should be taken into account.

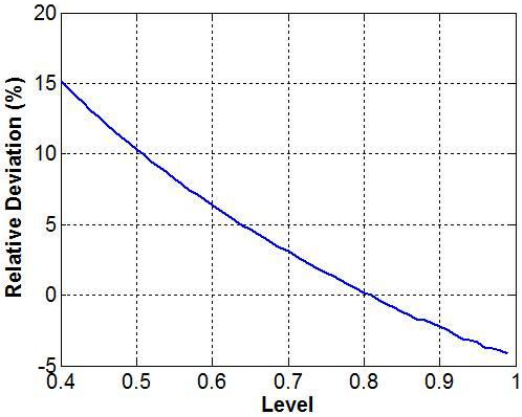

Fig. 3.15 Relative deviation of the obtained shear wave speed value from Eq. 3.38 from the expected value as a function of the contour level.

For the final result presented in Fig. 3.16 along with the B- mode image on the left, an average over the different contour levels was performed. A good general qualitatively agreement is found with the B-mode image and the shear wave speed map. An average shear wave speed of 1.52 ± 0.05 m/s and 3.81 ± 0.08 m/s was found for the top and bottom layer respectively. The obtained speed values are in good agreement with alternative shear wave speed measurements through transient elastography.

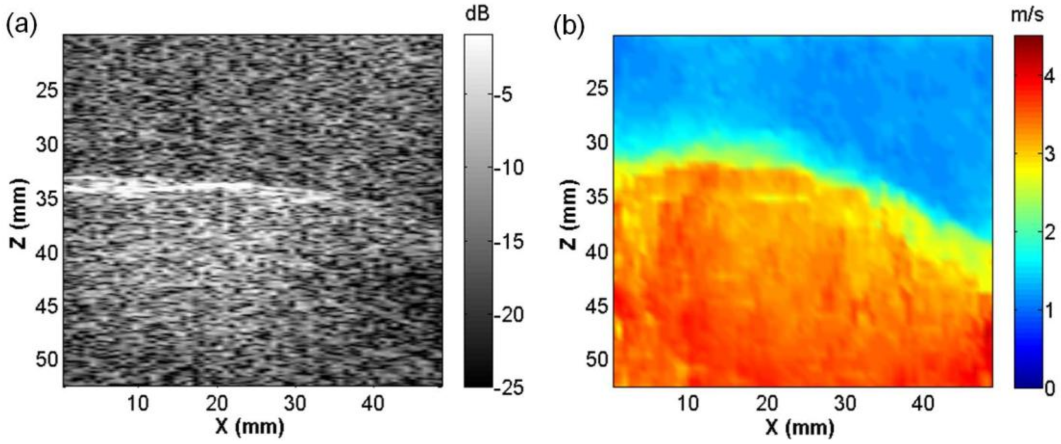

Fig. 3.16 Shear wave speed map from the focal width method by using phase correlation. The hard and the soft part are clearly visible in good agreement with the sonogram on the left. The obtained mean shear wave speed values for each part coincide with the ones obtained by transient elastography.

3.3.3 "Ultraslow" shear wavelength tomography

In this section, the same experiment described before is performed but instead of using a 1000 Hz frame rate, an "ultraslow" 10 Hz rate is used. In this section, the words "ultrafast" and "ultraslow" refer to the sampling rate of the ultrasonic scanner, not to the shear wave speed. Thus, in the "ultraslow" experiment, the sampling rate of the imaging system is well beneath the Nyquist limit: our shear waves are under sampled, thus the time information is lost, but the spatial information is still there and related to the shear wavelength. This is clearly apparent on the correlation field shown in Fig. 3.17. Due to the lack of time information, instead of using phase correlation, the correlation field will be calculated using the normalized correlation given by Eq. 3.8 evaluated at $t = T$. The typical cross observed in a time reversal experiment is no more apparent in Fig. 3.17. There is a total decorrelation in time except at the focalization time, which corresponds to the autocorrelation. This is the same result obtained if each time measurement is independent from each other, as for random-like signal. As far as space focalization, this latter is not true and the spatial decorrelation is clearly visible in Fig. 3.17 still related to the shear wavelength. Consequently, the loss of time information, due to the slowness of the imaging device, is not an obstacle for the focal width method as it was already observed in the work of *Benech et al.* [3].

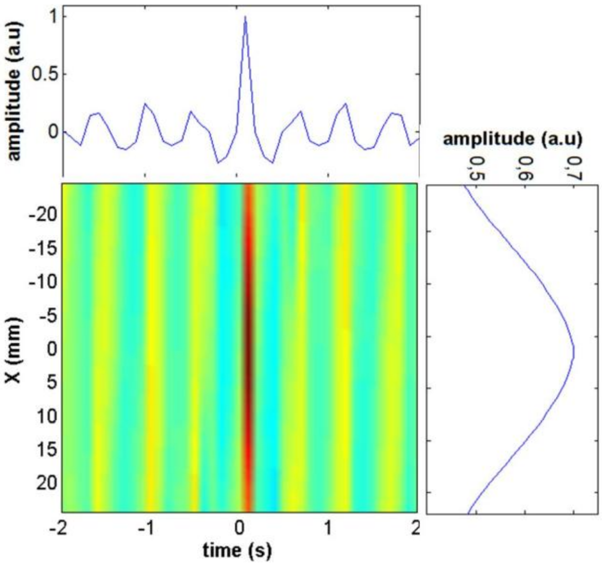

Fig. 3.17 Correlation field for the "ultraslow" experiment. The typical cross observed in a time reversal experiment is no more apparent. There is a total decorrelation except in time, except at time t=0, which is the autocorrelation. As far as space is concerned, this is not true and the spatial decorrelation visible remaining related to the shear wavelength.

"Ultraslow" experiments in the same phantom as the "ultrafast" experiment were carried out. In Fig. 3.18(a) the B-Mode image of the bi-layer phantom for this experiment is shown. On the right, a two dimensional representation of the normalized displacement field at the focalization time is presented. The focal spot obtained in the soft and in the hard part with its 0.9 level contour in black are also presented (Fig. 3.18 (b) and (c) respectively). Again the focal spot clearly appears bigger in the hard medium which logically follows from the elastic properties of each part.

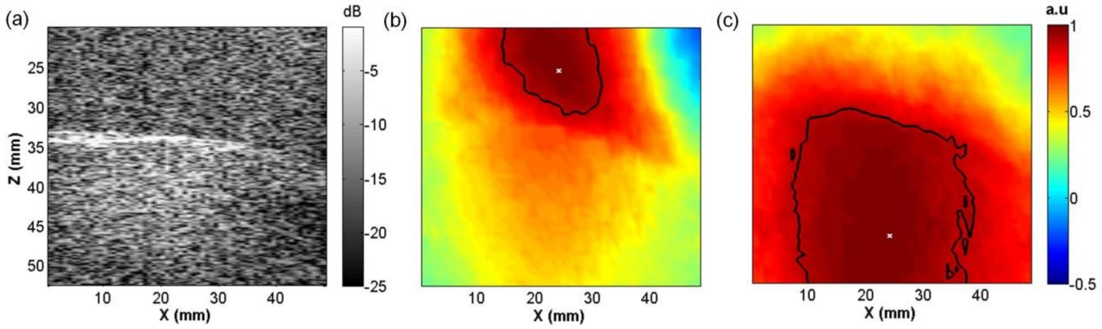

Fig. 3.18 (a) B-mode image of the bi-layer phantom. The spatial refocusing along with its 0.9 contour is presented in (b) the soft and in (c) the hard part.

By locally measuring the mean radius for different contour levels the images presented in Fig. 3.19 were obtained. It is important to notice that the two mediums are clearly visible in each image, despite the very low frequency rate, in good agreement with the phantom's B-mode image. Each image correspond to a given contour level between 0.8 and 0.99. Based on Eq. 3.34, the mean radius to a given isolevel curve is proportional to shear wave speed. However, due to the lack of information on the frequency content of the elastic field, is not possible to convert the mean radius images presented in Fig. 3.19 into shear wave speed maps.

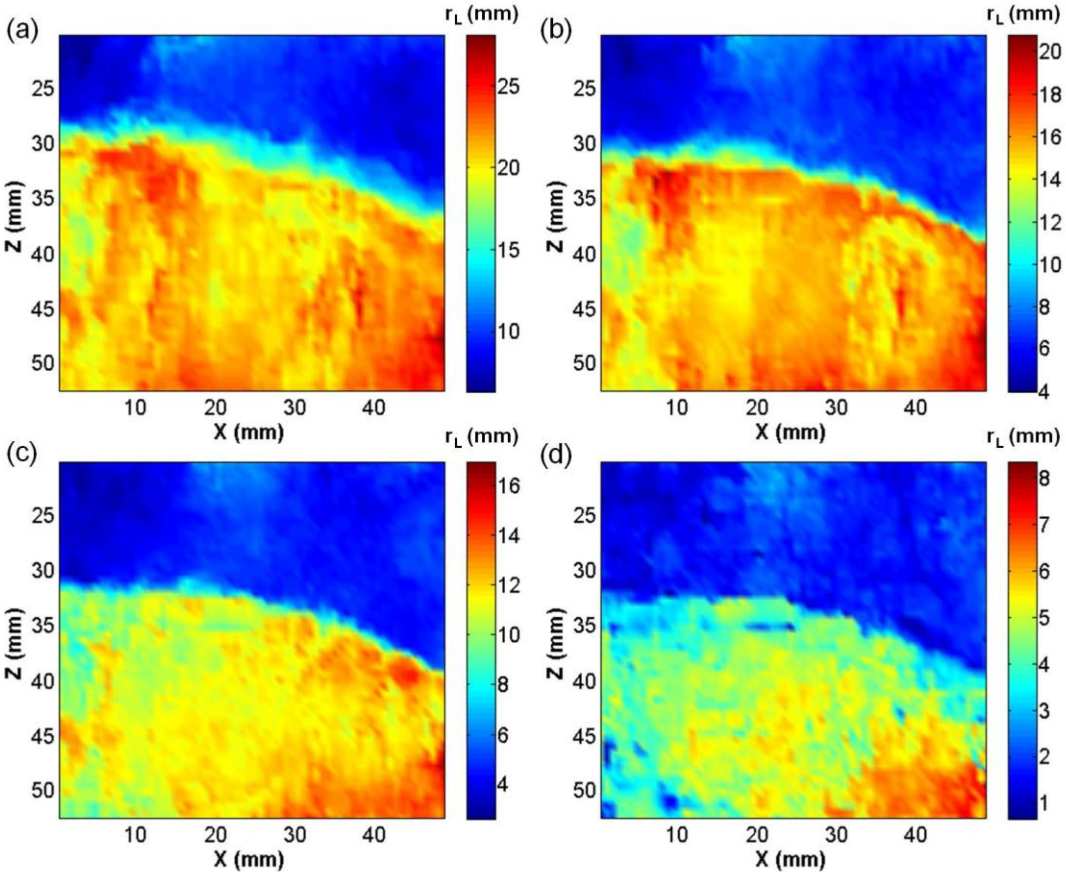

Fig. 3.19 "Ultraslow" experimental results using different contour levels (a) 0.8 (b) 0.9 (c) 0.95 and (d) 0.99. The color scale is set by $\bar{r}_L$ since due to the lack of information on the frequency components no conversion to shear wave speed is possible. Thus the images are proportional to the shear wave speed through Eq. 3.34.

By assuming the same frequency content as in the "ultrafast" experiment, the mean radius images could be converted into shear wave speed maps. The result is presented in Fig. 3.20. For the presented shear wave speed map an average over all contour levels was performed. A mean shear wave speed of 1.60 ± 0.20 m/s and 3.38 ± 0.06 m/s was found for the top and bottom layer respectively. The obtained speed values are in good agreement with alternative shear wave speed measurements through transient elastography and the "ultrafast" experiment.

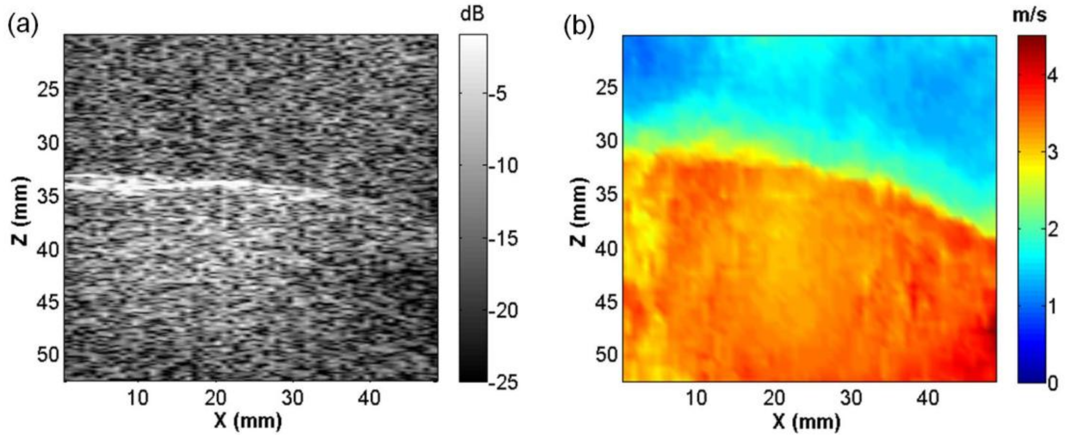

Fig. 3.20 "Ultraslow" experimental results converted to shear wave speed assuming the same frequency content as in the "ultrafast" experiment.

3.3.4 In Vivo "Ultrafast” wavelength tomography in the liver

In this section, in order to test the potential of TRE as passive elasticity imaging technique, an *in vivo* "ultrafast" experiment was carried out in the liver of one male, 27 years old, healthy volunteer. Some of the results and concepts presented in this section are part of the article entitled "Passive elastography: shear wave tomography from physiological-noise correlation in soft tissues" published in TUFFC-IEEE [10].

A schematic representation of the acquisition procedure is shown in Fig. 3.21. The elastic field generated by heart beating, breathing and muscular activity is measured in the belly muscle/liver by means of an ultrafast ultrasound scanner. In Fig. 3.21 a representation of the elastic field along a line of the imaging plane as function of time is presented. Displacements due to cardiac beats (red vertical lines) and motions due to breathing (blue vertical lines) can be observed. The displacement amplitude is quite small ($\sim 10\mu m$) when compared to the sensitivity of the ultrasonic speckle correlation technique given by Cramer-Rao limit ($\sim 1\ \mu m$) [83]. For this latter reason, the focal width method is used since is robust for low signal to noise ratio experiments.

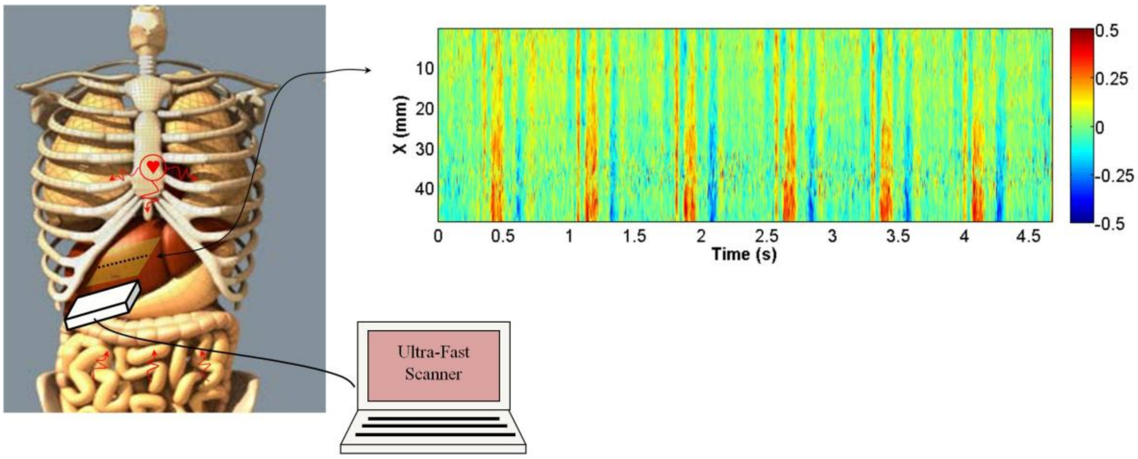

Fig. 3.21 Representation of the elastic field along a line for the *in vivo* experiment carried on in the liver. Displacements due to cardiac beats (red vertical lines) and motions due to breathing (blue vertical lines) can be observed.

For retrieving the shear wave speed map phase correlation with a whitening process between 5 Hz and 80 Hz was used. For the final result presented in Fig. 3.22, an average over different contour levels ranging from 0.4 to 0.7 was performed. For comparison the B-mode image is presented in Fig. 3.22(a), where the top zone is the belly muscle and the rest is occupied by the liver which is softer. On the shear wave speed map (Fig. 3.22(b)) belly muscle and liver are clearly apparent. As in the *in vitro* experiments, the interface between both medium appears at little bit deeper when compared to the B-mode image.

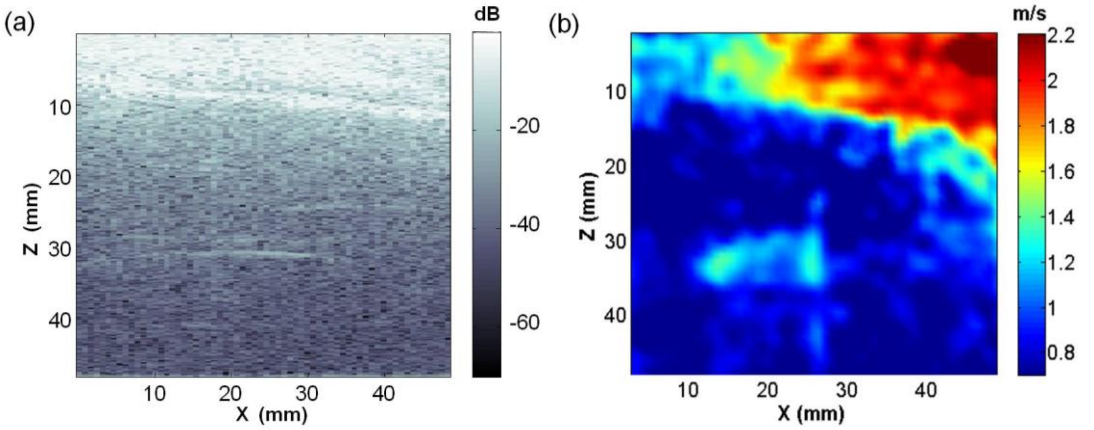

Fig. 3.22 Shear wave speed map obtained in the *in vivo* experiment compared to the B-mode image on the left. In the B-mode image the top zone is the belly muscle and the rest is occupied by the liver which is softer. On the shear wave speed map these two types of tissue are apparent. The obtained shear wave speed were around 2 m/s in the muscle and between 0.5 and 1 m/s in the liver, in good agreement with reported values in the literature.

A mean shear wave speed value of 0.78 ± 0.04 m/s was found for the liver in agreement with the reported results in the literature. Using an MRI scanner *Huwart et al.* [26] measured a shear wave speed of 0.86 ± 0.21 m/s at 65 Hz for the liver of five healthy volunteers (mean age 27 ± 5.7 years), while with the SSI technique [38] and the FibroScan [41] shear wave speed values of 1.18 ± 0.18 m/s and 1.06 m/s were respectively retrieved at 50 Hz for healthy volunteers.

To measure the shear wave speed in muscle is much more controversial than in the case of the liver, depending the latter on anisotropy as well as on the level of muscular contraction. In [61], it was found that for a relaxed biceps, shear wave speed values range from 0.5 m/s to 2 m/s depending on the fiber orientation respect to the shear wave propagation direction. In [61], it was also shown that the shear wave speed value depends on the muscular level of contraction, being approximately two times bigger for a biceps submitted to a 4 kg load than for a relaxed one. In the present experiment, the level of contraction as well as the wave polarization are difficult to determine. A mean value of 1.41 ± 0.13 m/s was found for the belly muscle in good agreement with the different reported results. A variation between 1 m/s (top left corner of Fig. 3.22(b)) to 2.4 m/s (top right corner of Fig. 3.22(b)) is observed. This variation could be explained based on the aforementioned problem of anisotropy and muscular contraction. However, there might be another source of error which can be affecting the shear wave estimation: the directionality of the noise field. For the present experiment, noise field mainly comes from the heart and breathing, being highly directional. Thus, instead of dealing with a perfect time reversal cavity, we have a time reversal mirror, resulting in a deformed spatial focalization due to diffraction effects. A deeper insight on this problem will be given in the next section.

3.3.5 From bi-layer mediums to inclusion detection using Time Reversal Elastography

In the previous sections, a method for extracting the shear elasticity of soft tissues from a complex reverberated elastic field, using spatiotemporal correlations interpreted in the frame of the time-reversal symmetry, was presented. By measuring the shear wavelength from the focal width as the wave converges, a shear wave speed map was obtained. The feasibility of TRE as an imaging technique was tested *in vitro* and *in vivo* in bi-layer mediums. In this section a step forward is taken to detect small inclusions embedded in a larger medium.

Thus, the experiment is the same as described before: a complex elastic field is created inside the sample by randomly tapping it on the surface. The displacement field was measured by means of ultrasound using an ultrafast scanner (Lecoeur Electronique, France) at a 1000 Hz frequency rate. As a sample, a tissue mimicking phantom made of PVA-C was used. The phantom contained two cylindrical inclusions, also made of PVA-C. One inclusion was submitted to five cycles while the other only underwent one. The background gel underwent two cycles. As a result a phantom containing two inclusions, one harder (≈ 10 mm diameter) and one softer (≈ 14 mm diameter) than de BG was obtained. A final shear wave speed of 2.2 ± 0.3 m/s, 4.1 ± 0.3 m/s and 2.9 ± 0.3 m/s was found for the soft inclusion, the hard inclusion and the BG respectively, by applying an independent transient elastography technique. A schematic representation of the experimental configuration is presented in Fig. 3.23 along with the sample's B-mode image, where the hard and soft inclusion are hardly visible as small echoes around ≈ 10 mm and ≈ 30 mm depth respectively.

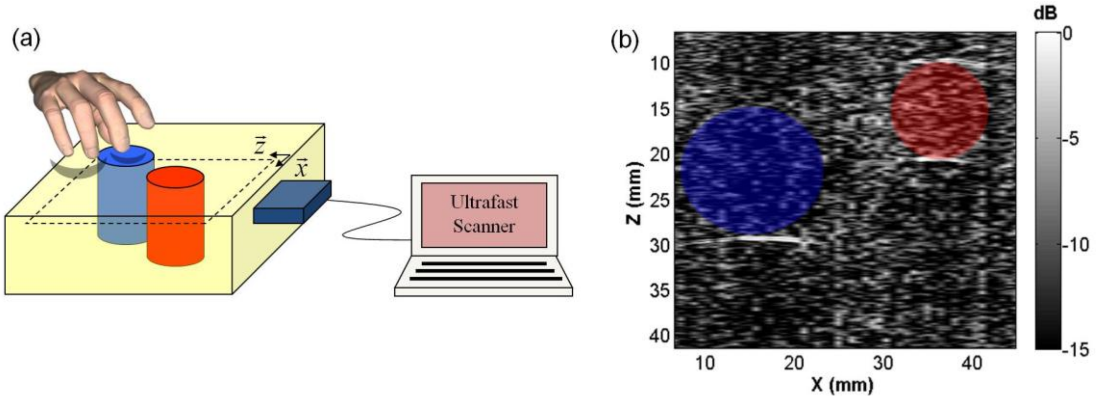

Fig. 3.23 (a) Schematic representation of the experimental setup. (b) Sample's B-mode image. The red and blue circles indicates the hard and the soft inclusion position respectively.

To construct the shear wave speed map, normalized correlation and phase correlation were applied to the displacement field as described in the previous section. For the normalized correlation speed map no inclusions were visible at any contour level. This can be explained due to the low frequency content of our correlation field, which was prohibitive for obtaining the desired spatial resolution. For the soft inclusion at a 30 Hz central frequency a shear wavelength of approximately 70 mm is estimated, which is seven times bigger than the inclusion diameter.

In order to increase the high frequency content of our correlation field, phase correlation was used with a whitening process between 90 Hz to 150 Hz. The obtained shear wave speed map is shown in Fig. 3.24 along with its B-mode image. For computing the shear wave speed from the correlation field, the surface enclosed by a given isolevel curve was used (Eq. 3.37), instead of the mean radius used in the previous section. As stated earlier, this procedure is more robust to the presence of noise than the radius computation estimation. For the final shear wave speed map presented in Fig. 3.24(b), an average over different contour levels ranging from 0.5 to 0.9 was performed. The inclusions position is marked with a black dotted line. A mean shear wave speed of 1.6 ± 0.1 m/s, 3.5 ± 0.1 m/s and 2.7 ± 0.1 m/s was found for the soft inclusion, the hard inclusion and the BG respectively.

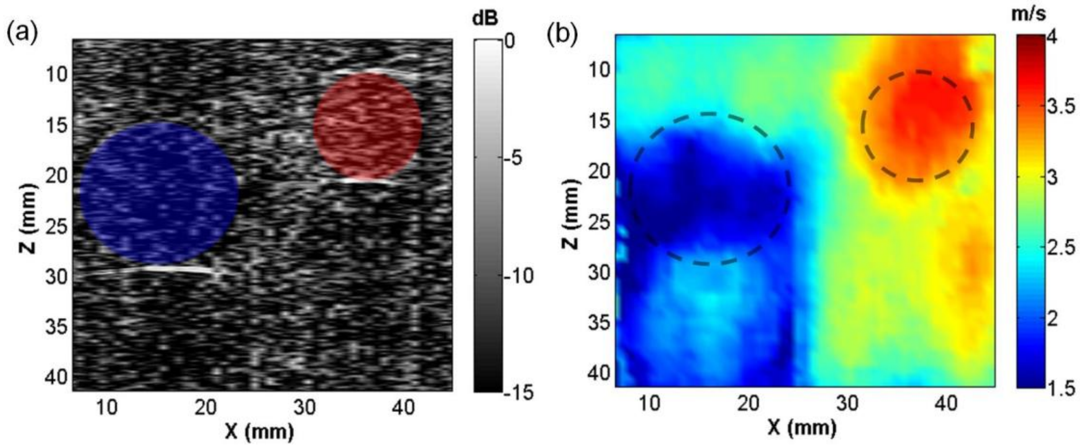

Fig. 3.24 (a) Sample's B-mode image. The red and blue circles indicates the hard and the soft inclusion position respectively. (b) Shear wave speed map obtained through a whitening process between 90 Hz to 150 Hz. An average for levels ranging from 0.6 to 0.9 was performed. The inclusion position is marked with a black dotted line.

Although shear wave speed estimations obtained by TRE lie beneath the values obtained through transient elastography, a general quantitative agreement within 10% was found between the different measurements of shear wave speed for the inclusions and the BG. The underestimation on the shear wave speed has already been observed in [10] and it can be attributed to the fact that the time reversed field is not isotropic because the source distribution is not isotropic either. The focalization movie which illustrates this problem is presented in Fig. 3.25. The black arrow at -4 ms indicates the wave front propagation direction. In a perfect time reversal cavity, during the focalization step, the converging wavefront enwraps the focal point as it schematized in Fig. 3.1 and in Fig. 3.5 for the case of soft solids. This is clearly not the case for the phase/normalized correlation experiments where the wave front mainly propagates along a given direction (Fig. 3.25). Thus, we are dealing with a time reversal mirror instead of a time reversal cavity: our source distribution is not homogeneously distributed in space. As a consequence of this problem the inclusions boundaries could not be resolved leading to several image artifacts visible in Fig. 3.24: firstly, the inclusion boundaries do not coincide exactly with the ones showed on the B-Mode image. Both inclusions appears to be deformed when compared to the B-mode. Secondly, there exist some image artifacts on the imaging plane limit (down right and left corner of Fig. 3.24), leading to a poor resolved soft inclusion. In the next Chapter the problem of an anisotropic time reversed field will be attacked by adapting the inverse filter to the particular case of a passive source configuration.

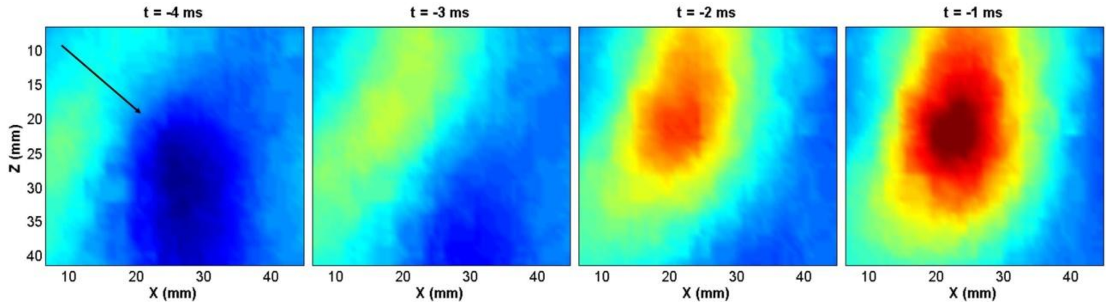

Fig. 3.25 Focalization movie using phase correlation. Four instants before the focalization time set equal to zero are presented. The black arrow at -4 ms indicates the wave front propagation direction.

3.4: Conclusions

In this chapter the feasibility of TRE as a quantitative imaging technique was studied in the cases of a bi layer mediums (e.g. phantom and muscle-liver) and of a phantom containing two cylindrical inclusions. In the case of the bi layer phantom the shear wave speed images were calculated using two different approaches: normalized and phase correlation. For both approaches the both layers were clearly visible and the obtained shear wave speed values coincide within the error margins with the 1D transient elastography estimations.

For the normalized correlation, in order to have good resolved images, it was necessary to measure the mean radius for higher contour levels (0.8 to 0.99). The main drawback of this technique is the knowledge of the frequency content for a given contour level in order to convert the mean radius into shear wave speed estimation. One way for solving this problem is to perform a calibration as the one presented in Fig. 3.11 based on the experimental spectrum. However, this procedure can be very time consuming in practical applications. In order to solve this problem an empirical formula is proposed (Eq. 3.41). This empirical formula can be interpreted as the focalization being dominated by one effective frequency which equals the mean root square frequency of the spectrum. By using this empirical formula the obtained shear wave speed maps were in good agreement with the B-mode images and the 1D transient elastography estimations. The main advantage of normalized correlation is its compatibility with "ultraslow" imaging devices, such as standard two-dimensional and three-dimensional ultrasound and magnetic resonance devices, placing this approach as a promising imaging technique.

In order to avoid the problem of frequency incertitude, phase correlation is introduced as a way to assure the frequency content at any contour level of the time reversed field. An analytical formula which relates the mean radius/surface for a given isolevel curve and the frequency bandwidth used in the whitening process with the shear wave speed is given in Eqs. 3.37 and 3.38. The higher the contour level is, the more valid the analytical formula is. A relative deviation on the shear wave speed estimated value from Eq. 3.38 of up to 10% is found for a 0.5 contour level. Despite this fact, a good agreement was found for shear wave speed maps obtained in the *in vitro* experiments when compared to the B-mode images and the obtained results through normalized correlation.

Finally the potential of the TRE technique was tested in an *in vivo* experiment and for the inclusion detection. In the *in vivo* experiment, it is important to note that while other elastography techniques suffer from the physiological noise in the human body, TRE takes advantage of this permanent elastic field. Passive elastography might be an alternative for elasticity imaging in deep organs or barely accessible regions where high-power ultrasound needed for radiation force is difficult to use. The obtained results with TRE for the *in vivo* experiment completely agree with the ones reported on the literature.

For the case of the inclusion detection, despite a good agreement in the obtained shear wave speed estimations through TRE, a high variability is observed in the shear wave speed map. This variability is also observed in the *in vivo* experiment in the belly muscle. The variability of the shear wave speed maps presented in Figs. 3.20 and 3.22 is believed to be related to the anisotropy of the shear-wave time reversal field. Indeed, it is well established in seismology that the flux resulting from a diffuse field [84], [85] can be responsible for bias in the tomography. From a time reversal point of view, we are dealing with a time reversal mirror instead of a time reversal cavity, due to the fact that the source distribution is not homogeneously distributed in space. Thus, the focal spots are deformed due to diffraction effects. As a consequence, the inclusions could not be satisfactory resolved, leading to several image artifacts visible in Fig. 3.24: firstly, the inclusion boundaries do not coincide exactly with the ones showed on the B-Mode image. Both inclusions appears to be deformed when compared to the B-mode. Secondly, there exist some image artifacts on the imaging plane limit (down right and left corner of Fig. 3.24), leading to a poor resolved soft inclusion.

In order to solve this problem, one possible solution is to use a completely diffuse field with a more homogeneous source distribution. An example of this kind of field is the noise created due to thermal fluctuations [78]. But to be able to measure the displacement field created by thermal fluctuations by means of ultrasound in tissue mimicking phantoms, the ultrasonic precision should be increased 100 times. A second possible solution, is to use in an optimal way the information conveyed by the field in order to minimize the anisotropy effects. In the next Chapter, a solution to this problem will be proposed by adapting the technique known as inverse filter to particular case of a passive source configuration: the passive inverse filter.

Chapter IV

The passive inverse filter

In the previous Chapter, a method for constructing a shear wave speed map of soft tissues from a complex reverberated elastic field, using spatiotemporal correlations interpreted in the frame of time-reversal, was developed. The potential of Time Reversal Elastography as a quantitative imaging technique was shown *in vitro* and *in vivo* in bi-layer mediums. However, the main drawback of this technique arises when trying to image small inclusions. Due to the sources in the noise experiments are not homogeneously distributed over the phantom surface, the resulting time reversed field is not isotropic. Instead, it has privileged propagation direction. From a time reversal point of view, instead of a perfect time reversal cavity, we are dealing with a time reversal mirror, leading to deformed focal spots due to diffraction effects. As a consequence, the inclusions could not be satisfactory resolved leading to several image artifacts.

In this Chapter, a solution to this problem is proposed based on the technique known as inverse filter. The inverse filter was first developed in optics to correct blurred images. In the late nineties *Tanter et al.* [86] adapt it to acoustics. By using an ultrasonic array as a set of active controlled sources and the inverse filter *Tanter et al.* [86] were able to focalize ultrasonic waves through aberrating and absorbing media. When compared to a time reversal experiment, a higher signal to noise ratio in the spatial-temporal focalization was achieved by using the inverse filter. As stated in the previous Chapter, in a passive source configuration (without controlled sources), the cross correlations can be interpreted as a time reversal operation through a virtual time reversal mirror made of noise sources. Thus, if the inverse filter is an improved version of a time reversal experiment in the case of controlled sources, could it be possible to adapt it to the case of a passive source configuration, in order to improve our noise correlation experiments? The answer to this question is the technique proposed in this Chapter, named as passive inverse filter. With such passive inverse filter, not only the signal to noise ratio in the spatial focalization is improved, but the spatial distribution of noise sources is made homogeneous. As a result better resolved images were obtained or in other words a better Green's function reconstruction, when compared to the standard cross correlation, was achieved.

To present the passive inverse filter, I will begin this Chapter by introducing the classic inverse filter, which is based on the inversion through a single value decomposition of the propagation operator relating an array of transducers to a set of control points. Then, I will present the passive inverse filter. In particular, I will discuss how to determine what is the number of singular values that have a physical meaning and therefore should be taken into account in the inversion. To conclude, I will present how the passive inverse filter corrects for the anisotropy of the time reversed field in the particular case of the elastography experiments presented throughout this thesis. The obtained shear wave speed maps for the bi-layer medium, inclusions and *in vivo* passive elastography will be presented and compared to the ones obtained by normalized/phase correlation.

4.1: The classic inverse filter

The spatial-temporal inverse filter developed by *Tanter et al.* [86] is based on the matrix formalism of the propagation operator H between a set of controlled sources and receivers, as represented in Fig. 4.1(a). Let $h_{ij}(t)$ be the impulse response for each pair (i,j) comprising a control point and a source, such that $h_{ij}(t)$ is the signal received on the receiver j after a temporal delta function is applied on the source i. This response takes into account all of the propagation effects within the medium, as well as the acousto-electric responses of sources and receivers.

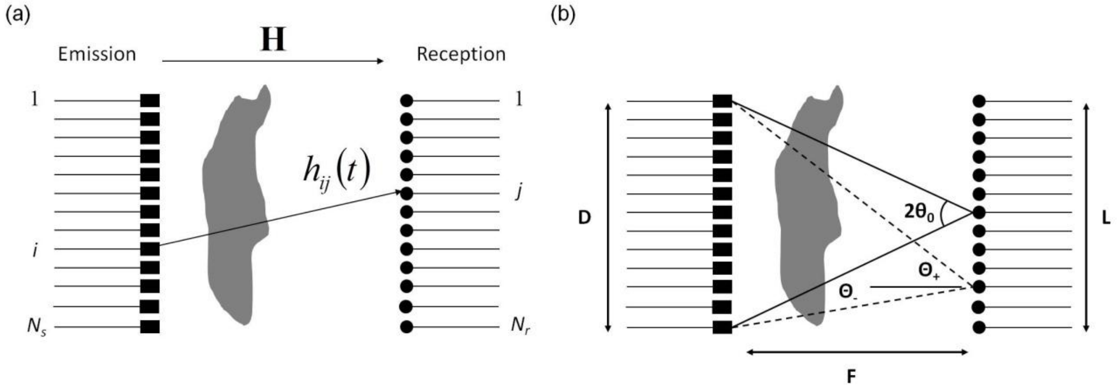

Fig. 4.1 (a) The propagation operator H relates a linear array of sources with a control line of receivers. (b) Schematic representation of the experimental configuration used in [86]. The limited aperture of the array set a limit to the number of eigenvalues used during the inversion. **Source: *Tanter et al.* [86]**

From a linear system point of view, the response $r_j(t)$ on a receiver j for a set of emitted signals $e_i(t)$,$1 \leq i \leq N_s$, where N_s is the number of sources, can be written as the following convolution product between the emissions (inputs) and the impulse responses $h_{ij}(t)$:

$$r_j(t) = \sum_{i=1}^{N_s} h_{ij}(t) \otimes e_i(t), \qquad 1 \leq j \leq N_r \tag{4.1}$$

A temporal Fourier transform to Eq. 4.1 leads to the following relation,

$$R_j(\omega) = \sum_{i=1}^{N_s} H_{ij}(\omega) E_i(\omega), \qquad 1 \leq j \leq N_r \tag{4.2}$$

Where $R_j(\omega)$ and $E_i(\omega)$ are the Fourier transform of the response and the emission respectively and N_r is the number of receivers. Equation 4.2 can be expressed in matrix form as follows:

$$R(\omega) = H(\omega)E(\omega) \tag{4.3}$$

Where $E(\omega)$ is the vector of the emitted signals and $R(\omega)$ is the vector of the received signals. The transfer matrix $H(\omega)$ describes the propagation through the medium from the set of emitting points for a single frequency ω. From now on, the ω dependence will be understood. The goal is then, to focalize at a given receiver position, e.g. j_o. Typically the target pattern is taken to be a spatial delta function, thus it can be written as:

$$R^{ideal} = \begin{array}{ccccc} (0 & \ldots & 1 & \ldots & 0) \\ 1 & \ldots & j_o & \ldots & N_r \end{array} \tag{4.4}$$

Where the number 1 corresponds to the j_o position. Based on Eq. 4.3 the ideal emission is then given by:

$$E^{ideal} = H^{-1}R^{ideal} \tag{4.5}$$

As in the case of all inverse problems, the inversion of H is ill-conditioned, meaning that the solution to the inversion does not depend continuously on the data, but rather small errors in the data produce very large errors in the reconstructed field. Thus, a regularization of the problem is introduced by computing a singular value decomposition before the inversion. The propagation matrix can be decomposed as,

$$H = UD\tilde{V} \tag{4.6}$$

Where D is a diagonal matrix of singular values arranged in decreasing order and U and V are unitary matrices. The symbol $\tilde{}$ in Eq. 4.6 denotes transpose and conjugate of the matrix V. As proposed by *Tanter et al.* [86], the matrix inversion is only applied to the main singular vectors of the singular value decomposition, giving rise to a noise filtered matrix $\widehat{H}^{-1}$ of H^{-1}. Based on Eq. 4.6 the filtered matrix $\widehat{H}^{-1}$can be written as:

$$\widehat{H}^{-1} = V\widehat{D}^{-1}\widetilde{U} = V\begin{bmatrix} \lambda_1^{-1} & 0 & \ldots & \ldots & \ldots & 0 \\ 0 & \ddots & 0 & & & \vdots \\ \vdots & 0 & \lambda_N^{-1} & & & \vdots \\ \vdots & & & 0 & & \vdots \\ \vdots & & & & \ddots & \vdots \\ 0 & \ldots & \ldots & \ldots & \ldots & 0 \end{bmatrix}\widetilde{U} \tag{4.7}$$

Where N is the number of physically relevant singular values that should be taken into account in the inversion. Later on this section, I will come back on how the number N can be physically interpreted and thus selected. Once the ideal target is chosen, the ideal emission is given by Eq. 4.5, thus combining Eq. 4.5 with Eq. 4.7 the focalization by the inverse filter is given by:

$$R^{IF} = HE^{ideal} = H\hat{H}^{-1}R^{ideal} = U\begin{bmatrix} 1 & 0 & \dots & \dots & \dots & 0 \\ 0 & \ddots & 0 & & & \vdots \\ \vdots & 0 & 1 & & & \vdots \\ \vdots & & & 0 & & \vdots \\ \vdots & & & & \ddots & \vdots \\ 0 & \dots & \dots & \dots & \dots & 0 \end{bmatrix}\tilde{U}R^{ideal} \tag{4.8}$$

Equation 4.8 shows that R^{IF} corresponds to the projection of the ideal target on the N main eigenvectors of the singular value decomposition of H. Thus, once the propagation matrix is acquired, the inverse filter focusing R^{IF} can be easily calculated by applying Eq. 4.8. However, to perform a proper inversion trough Eq. 4.8, the number N of physically relevant singular values should be determined.

4.1.1 Determination and interpretation of the number N of singular values

In this section, the problem of determining the number N of physically relevant singular values for the classic inverse filter will be addressed. Based on the configuration presented in Fig. 4.1 two sources of spatial information loss can be mentioned. If the control plane is placed in the emitter's far field, the irreversible loss of the evanescent waves through propagation sets a bound to the effective spatial information conveyed by the field. In the angular spectrum formalism, it results in a cutoff frequency in the angular spectrum components [87]. Another source of spatial information loss, is the limited aperture of the control point array: the array intercepts only a limited part of the wave field radiated by any point source in the medium, defining a bundle of plane waves included within a cone relating the control point to the array aperture (Fig. 4.1(b)). This bundle of plane waves consists of the angular spectrum components of the field radiated by the array that can be received at the control point location.

From a matrix point of view, the eigenvalue distribution divides the space into two subspaces: the kernel of H which is related to noise and the rank of H. The rank of H, which is equal to the number of non zero singular values, is related to the minimum number of parameters necessary to define the field that can be created by the array in the control plane. Using a plane wave decomposition of the field, this number equals the number of angular spectrum components achievable by the array in the control plane. Following an argument of Von Laue [88], which was further developed by Gabor [89], [90], this minimum number N of independent parameters represents the spatial number of degrees of freedom of the wavefield. Hereinafter, the number N will be calculated for the configuration presented in Fig. 4.1(b).

In the case of Fig. 4.1(b), for a given control point the cone defining the bundle of plane waves is limited by the angles θ_+ and θ_-. The spatial frequency bandwidth B, that can potentially be generated by the source array at the control point location, is given by:

$$B = f_+ - f_- = \frac{sin\theta_+ - sin\theta_-}{\lambda} \tag{4.9}$$

The latter frequency bandwidth depends on each control point, being maximum for the central control point. In that case, B can be calculated based on Fig. 4.1(b) as follows:

$$B_{max} = f_o - (-f_o) = 2\frac{sin\theta_0}{\lambda} = 2\sin\left(\tan^{-1}\frac{D}{2F}\right)/\lambda \tag{4.10}$$

According to Shannon's sampling theorem, the optimal spatial resolution δ_x in the control plane is given by:

$$\delta_x = \frac{1}{B_{max}} = \frac{1}{2}\lambda/\sin\left(\tan^{-1}\frac{D}{2F}\right) \tag{4.11}$$

Thus, an overestimation of the number N of spatial degrees of freedom, necessary to define the field received in the control plane, is given by the ratio between the width L of the control plane and the resolution δ_x required to sample the spatial distribution of the field in the control plane:

$$N = \frac{L}{\delta_x} = \frac{2L}{\lambda}\sin\left(\tan^{-1}\frac{D}{2F}\right) \tag{4.12}$$

Equation 4.12 is valid in the near field as well as in the far field of the source array. However, it can be simplified in the far field under the Fraunhofer assumption, when $D/2F \gg 1$, the number of eigenvalues can be calculated as:

$$N \cong \frac{DL}{\lambda F} \tag{4.13}$$

It is worth noticing, that in the far field approximation, N can be seen as the number of independent focal spots that the array is able to generate in the aperture L of the image plane. Equation 4.13 is a consequence of the loss of spatial information, due to the limited aperture of the array and due to evanescent waves. In the case of a perfect time reversal cavity, is important to notice, that no cutoff frequency due to the limited aperture of the array is present. Instead, of a cone defined by the angular spectrum components at each control point, a sphere containing all the angular spectrum components is defined. Thus, the cutoff frequency is due to the loss of information through the evanescent waves (far field approximation) and is given by Rayleigh diffraction limit: $\lambda/2$, leading to $N = L/(\lambda/2)$. This fact can be qualitatively explained based on Eq. 4.12 making $D = 2\pi R$ and $F = R$ where R is the cavity radius. Substituting in Eq. 4.12 N can be calculated as: $N = 0.95\frac{L}{\lambda/2} \approx \frac{L}{\lambda/2}$.

The noise experiments presented in this manuscript clearly differentiate from the classic inverse filter experiment. While for the classical inverse filter each source is completely controlled, in the noise experiments, sources are randomly activated on the sample's surface. The displacement field is then recorded in a two dimensional control plane (imaging plane), instead of a control line. Thus the question is the following: how can the previous concepts presented in the frame of the classic inverse filter be extended to the noise experiments presented in this manuscript? The answer to this question is the passive inverse filter technique.

4.2: The passive inverse filter

In the previous section, the classic inverse filter, which assures an optimal use of the spatial-temporal information was presented. In its present form, the classic inverse filter relates a linear array of sources to a control line. Consequently, in order to apply it to the noise experiments the classic inverse filter should be adapted to a passive source configuration. Hereinafter, such adaptation will be presented: the passive inverse filter.

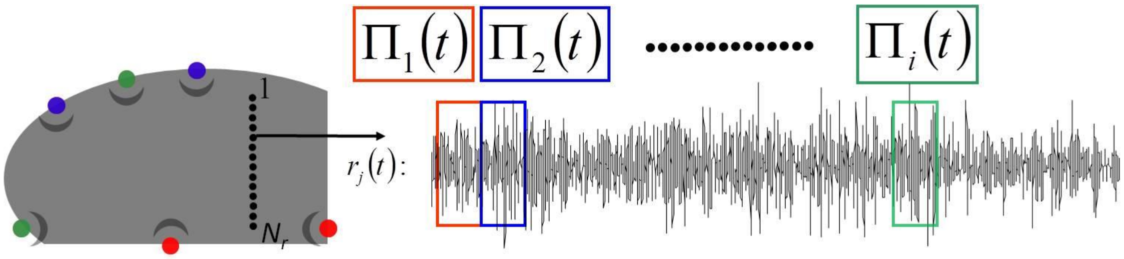

Fig. 4.2 Schematic representation of the passive inverse filter. Randomly activated sources generate a complex reverberated wave field which is measured on the control plane R. By windowing the recorded signals a new transfer matrix $\breve{H}$ is constructed.

Let us consider a cavity, as the one presented in Fig. 4.2, where sources are randomly activated on its surface as in the case of the experiments presented along this manuscript. The complex wavefield is measured in a control plane R inside the volume of the cavity. The typical signal measured by one of the sensors is presented on the right of Fig. 4.2. A modified transfer matrix $\breve{H}$ is constructed by windowing this noise-like signal. The idea behind this construction is the following: the first window will contain the response of some set of randomly activated sources represented in red in Fig. 4.2, the second window the response of some other set of sources represented in blue, etc. Thus, each window contains the response of some set of randomly activated sources, which cannot be located nor controlled. The response of this set of unknown sources, named $\check{h}_{ij}(t)$, can be written as the product of the ith window with the measured signal in the jth control point:

$$\check{h}_{ij}(t) = r_j(t).\Pi_i(t) \tag{4.14}$$

Where $\Pi_i(t)$ is defined as: $\Pi_i(t) = \begin{cases} 1, & t_i \leq t \leq t_i + \Delta t \\ 0, & elsewhere \end{cases}$

Being t_i the initial windowing time and Δt the window length. The window length is chosen in a way that, on average, each window contains at least two impulse responses. The difference between $h_{ij}(t)$ and $\check{h}_{ij}(t)$ is, while h_{ij} represents the response of one active source, $\check{h}_{ij}$ represents the responses of some unknown set of randomly activated sources which contribute to the given time window $\Pi_i(t)$. Consequently, the measured $r_j(t)$ signal can be written as a convolution product between the emission of a set of sources, which we are not able to control neither to locate, with an impulse response $\check{h}_{ij}(t)$ which is measured in each window:

$$r_j(t) = \sum_{i=1}^{N_s} \check{h}_{ij}(t) \otimes e_i(t) \tag{4.15}$$

Based on Eq. 4.15, it is possible to use the inverse filter on the new transfer function $\check{h}_{ij}(t)$ as if it was possible to control all these pseudo-sources:

$$R^{IF} = \check{H}E^{ideal} = \check{U}\begin{bmatrix} 1 & 0 & \dots & \dots & \dots & 0 \\ 0 & \ddots & 0 & & & \vdots \\ \vdots & 0 & 1 & & & \vdots \\ \vdots & & & 0 & & \vdots \\ \vdots & & & & \ddots & \vdots \\ 0 & \dots & \dots & \dots & \dots & 0 \end{bmatrix}\widetilde{\check{U}}R^{ideal} \tag{4.16}$$

Equation 4.16 is the passive inverse filter. With the construction of the modified propagation operator $\check{H}$, it will be possible to use the inverse filter to optimize the wave field spatial-temporal degrees of freedom, resulting in a much more homogeneous focalization as it will be demonstrated in section 4.3.1 for the case of the noise experiments presented in this thesis. However, to conduct a proper inversion the number N of physically meaningful eigenvalues should be established.

4.2.1 Determination of the number N of singular values in the case of the passive inverse filter

In section 4.1.1, the problem of determining the number of useful eigenvalues was presented for the experimental setup proposed by *Tanter et al.* [86] in the classic inverse filter: a linear array of sources and a control line. In this section, a more general situation will be considered: a surface of sources and a two dimensional control plane. This configuration is more suitable to the passive inverse filter configuration presented in this thesis. However, the basic concepts for each one of the cases remain the same. *Gabor* [90] has shown for an homogeneous medium, that the number N of degrees of freedom of a wavefield $U(\vec{r})$ produced by a source's surface on a control point is given by:

$$N = \left(\frac{\Delta x}{\delta_x}\right)\left(\frac{\Delta y}{\delta_y}\right) = \frac{A}{\delta_x.\delta_y} = \frac{A\Delta p\Delta q}{\lambda^2} = \frac{A\Delta\Omega}{\lambda^2} \tag{4.17}$$

Where $\Delta\Omega = \iint_{\phi_-,\theta_+}^{\phi_+,\theta_+} cos\theta.sin\theta d\theta d\phi = \Delta p\Delta q$ is the element of solid angle in a cone about the z-axis. This cone constitutes the bundle of all possible directions of propagation with directional cosines p, q and m of the plane wave components of $U(\vec{r})$, such that $p^2 + q^2 \leq M$, M being a real constant such that $M \leq 1$. By taking into account the angular spectrum representation of $U(\vec{r})$ and according to Shannon sampling theorem, the propagating wavefield $U(\vec{r})$ is completely specified at any transversal plane z = constant from its sampling values at points of this plane at the Nyquist frequency, i.e. forming a grid with separation interval $\delta_x = \lambda/\Delta p$ along the x-direction and $\delta_y = \lambda/\Delta q$ along the y-direction. Hence, in a surface $A = \Delta x\Delta y$ the number of degrees of freedom is given by Eq. 4.17.

Equation 4.17 can be seen as a two dimensional generalization of Eq. 4.12, which relates the number of the degrees of freedom N to the control plane length L, the array aperture D, the distance between array and control line F and the ultrasonic wavelength λ, for the experimental configuration used by *Tanter et al.* [86]. In Eq. 4.17, it suffices to substitute $\Delta x = L$ and $\delta_x = \frac{1}{2}\lambda/\sin\left(\tan^{-1}\frac{D}{2F}\right)$ to retrieve Eq. 4.12. Equation 4.17 can be extended for the case of a three dimensional cavity and a control plane, as it was done in section 4.1.1 with Eq. 4.12 for a two dimensional cavity. Thus, the number of degrees of freedom for 3D cavity and a 2D control plane can be estimated as:

$$N = A_{imag}/A_{focus} \tag{4.18}$$

Where A_{imag} is the surface of the imaging plane and A_{focus} is the surface of the focal spot at -6 dB given by the diffraction limit. In Chapter III, it was demonstrated that the focal spot shape in the case of an elastic wavefield in an homogeneous soft solid at -6dB is approximately given by an ellipse with major and minor semi-axis $a = \sqrt{5}\lambda_s/2\pi$ and $b = \sqrt{5}\lambda_s/2\sqrt{2}\pi$ (L = 0.5 in Eq. 3.30). Thus, the number of degrees of freedom can be estimated as:

$$N = \frac{4\pi\sqrt{2}}{5}\frac{A_{imag}}{\lambda_s^2} = \frac{4\pi\sqrt{2}}{5}\frac{A_{imag}}{c_s(f)^2}f^2 \qquad (4.19)$$

Where in the second equality $c_s(f)$ is the shear wave speed and f is the temporal frequency. Equation 4.19 sets an apparent limitation to the applicability of the passive inverse filter for elastography, since a prior estimation of the shear wave speed is needed, in order determine the correct number of degrees of freedom for the inversion. There are two possible solutions to this problem: one possible solution is to perform a first estimation of the shear wave speed using phase correlation or normalized correlation as showed in Chapter III. A second possible solution may be given by the singular value distribution. In order to determine the possible ways for solving this problem, a closer look on the eigenvalue distribution in the case of the passive inverse filter will be given in the following section by using finite difference simulation.

4.2.2 Eigenvalue distribution for the passive inverse filter

The eigenvalue distribution divides the space into two subspaces: the kernel of H which is related to noise and the rank of H, which is equal to the number of eigenvalues. *Gabor's* expansion theorem [89] asserts that the number of degrees of freedom of a propagating wavefield is associated with the number of eigensolutions of the homogeneous Helmholtz equation. A proof of this theorem was first given by *Toraldo di Francia* [91]. In his work entitled "*Degrees of Freedom of an Image*" he demonstrated that all band-limited operators have the property that the eigenvalues λ_n drop to zero, often in a step-like form, for n larger than certain value N which is equal to the number of degrees of freedom of the wave field.

This behavior was observed by *Tanter et al.* [86] while focusing ultrasound through water. However, not for all experimental cases the latter behavior is true. For example, when trying to focus ultrasound through an aberrating or reverberant media [92] the single value distribution is modified due to the presence of the medium not dropping to zero in a step-like form. As a consequence it is difficult to determine N from the singular value distribution. As a solution to the problem, in [92], all the singular values up to a given noise level were used for the inversion, depending the noise level chosen on the particular experiment. Hereinafter, in order to determine a possible criteria for selecting N, the single value distribution for the passive inverse filter will be studied in the case of an homogeneous reverberating medium through simulation.

Two finite difference simulations were performed in a two dimensional cavity: sound propagating in water (scalar wave field) and an elastic wavefield in a soft solid cavity.

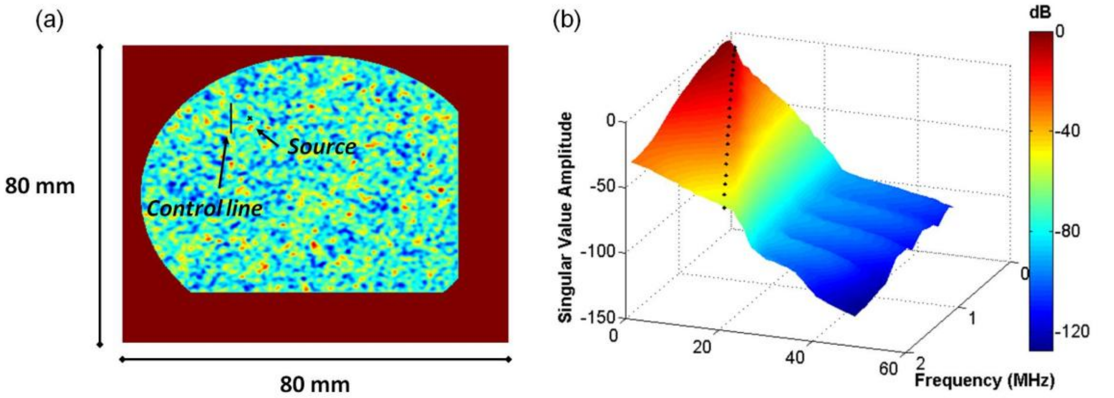

Fig. 4.3 (a) Representation of the scalar wavefield simulation. A source indicated by a black point is excited with two sinusoid cycles of 0.5 MHz central frequency. The reverberated field is recorded at a 5 MHz sampling frequency during 1 ms on a $L = 7.7$ mm control plane (spatial pitch = 0.11 mm). The propagating medium was set as water, whose sound speed is 1480 m/s. (b) Singular value distribution obtained using the passive inverse filter. The window length was set to 0.02 ms. In black dots the number of eigenvalues is calculated as $2L/\lambda$.

A representation of the scalar wavefield simulation is presented in Fig. 4.3(a). The propagating medium was set as water, whose sound speed and density were set to 1480 m/s and 1000 kg/m^3 respectively. A source, indicated by a black point, is excited with two sinusoid cycles of 0.5 MHz central frequency. The 1 ms reverberated field is recorded at a 5 MHz sampling frequency on a 7.7 mm length control line (spatial pitch = 0.11 mm). In Fig. 4.3(b) the spatial-temporal singular value distribution obtained for the passive inverse filter computed with a window length of 0.02 ms is presented. The number N of useful eigenvalues can be calculated as explained previously in section 4.1.1 as:

$$N(f) = \frac{L}{\lambda/2} = \frac{2L}{c} f \tag{4.20}$$

Where c stands for the sound speed and f for the frequency. Equation 4.20 is valid for a scalar field in a 2D cavity with a 1D control line, which is a particular case of Eq. 4.19, developed for a an elastic field in 3D cavity and a 2D control plane. In Fig. 4.3(b) the number N calculated from Eq. 4.20 is presented in black dots. In order to further clarify, the singular value distribution for 0.6 MHz and 1.2 MHz is presented in blue full line in Fig. 4.4 (a) and (b) respectively. The red dot in each figure indicates the predicted number N of eigenvalues calculated from Eq. 4.20. It is important to notice that, as predicted by *Toraldo di Francia* [91], an abrupt change in slope on the singular value distribution occurs when reaching the number N of degrees of freedom (red dot). This fact verifies that Eq. 4.20 can be used for estimating N if the wave speed is known. Contrary, if the wave speed is unknown, as in the case of the elastography experiments, the change in slope (if observable) could be used to predict N.

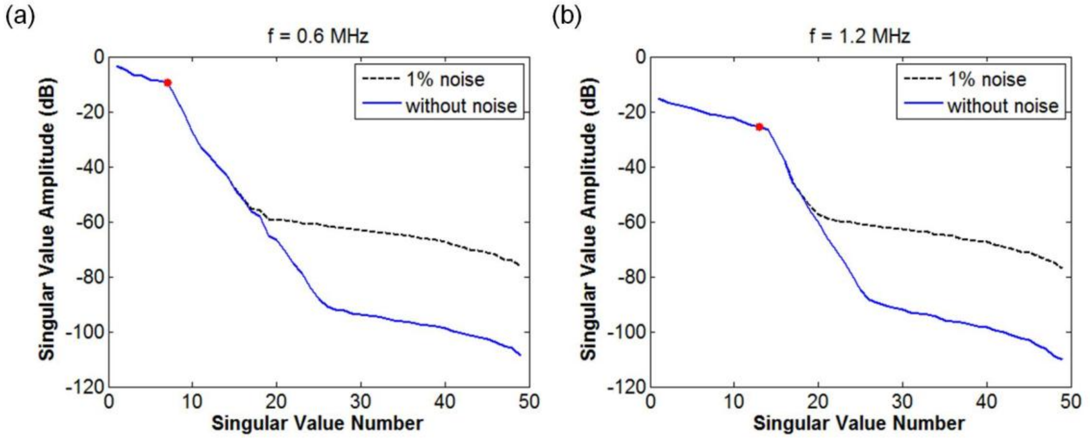

Fig. 4.4 Singular value distribution for (a) 0.6 MHz and (b) 1.2 MHz for the case of a scalar wavefield. The full blue line is the singular value distribution obtained from the passive inverse filter from the simulated displacement field. The dashed black line is the singular value distribution obtained from the passive inverse filter from the simulated displacement field affected by noise within 1% in amplitude.

In order to verify that the observed change in slope, while reaching the maximum number of eigenvalue is not only due to the scalar nature of the wavefield and that can be extended to the elastography experiments presented in this thesis, a second finite difference simulation was carried out using ACEL software [58]. A representation of the instantaneous wave field is presented in Fig. 4.5(a). The propagating medium was set as an elastic soft solid with a shear wave speed, longitudinal wave speed and density of 2 m/s, 1500 m/s and 1000 kg/m^3 respectively. Triangular, rectangular and round sections were cut off in order to avoid symmetry effects. The sources were randomly distributed and activated on the simulation grid surface as in the case of the noise experiments. Each source was excited with two sinusoid cycles ranging from 20 Hz to 200 Hz central frequency. The vertical component (z-component) of the displacement field was acquired at 1000 Hz sampling rate on a 24.4 mm length control line (0.4 mm spatial pitch).

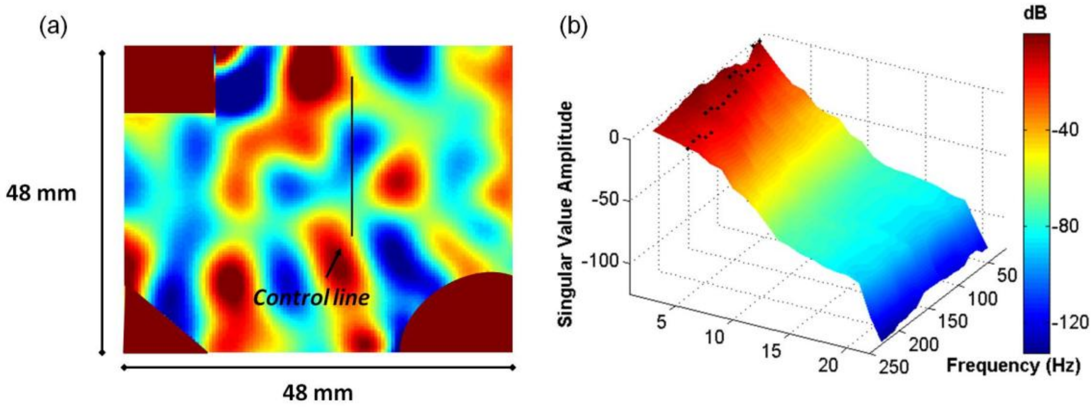

Fig. 4.5 (a) Representation of the instantaneous wave field. The propagating medium was set as an elastic soft solid with a shear wave speed, longitudinal wave speed and density of 2 m/s, 1500 m/s and 1000 kg/m3 respectively. Triangular, rectangular and round sections were cut off in order to avoid symmetry effects. The sources, excited with two sinusoid cycles ranging from 20 Hz to 200 Hz central frequency, were randomly distributed and activated on the simulation grid surface. The vertical component of the displacement field was acquired at 1000 Hz sampling on the control plane indicated by a black arrow. (b) Singular value distribution obtained using the passive inverse filter in the case of a vectorial field. The window length was set to 50 ms. In black dots the number of eigenvalues for a given frequency is calculated base on Eq. 4.21.

In Fig. 4.5(b) the spatial-temporal singular value distribution obtained for the passive inverse filter with a window length of 50 ms is presented along with the number N of eigenvalues in black dots. This number was calculated, as explained previously, as the number of independent focal spots on the control line. As a result from Eq. 3.28 the focal size for $\theta = 0$ (along z −direction) and a fraction of 0.5 (-6dB) is given by: $\Delta_z = 2\, r_{0.5}(\theta = 0) = \lambda_s\sqrt{5}/\pi$, where λ_s denotes the shear wave length. Thus, the number of eigenvalues is given by:

$$N = \frac{L\pi}{\sqrt{5}\,\lambda_s} = \frac{L\pi}{\sqrt{5}\,c_s} f \tag{4.21}$$

For better clarity, the singular value distributions for 60 Hz and 120 Hz are presented in Fig. 4.6 (a) and (b) respectively in blue full line. The red dot indicates the number N of eigenvalues calculated from Eq. 4.21 for each case. Again, an abrupt change in the slope on the singular value distribution is observed when reaching the number N of degrees of freedom. This verifies the fact that the number of useful eigenvalues can be deduced from the number of independent focal spots on the control line/plane no matter the nature of the wave field. This is the main principle on which Eq. 4.19 is based.

However, when carefully comparing the scalar and the elastic wavefield simulations, a difference between both situations can be noticed: the number of useful eigenvalues is much smaller in the case of the elastic field. This is due to the difference in frequencies, wave speeds and control plane size involved each simulation. From Eqs. 4.20 and 4.21 it can be observed that the number of useful eigenvalues depends basically on the ratio between the control plane length and the wavelength involved, being this ratio four times bigger for the scalar field in comparison to the elastic field. As a consequence, there are seven useful eigenvalues for 0.6 MHz and thirteen for 1.2 MHz (Fig. 4.4), while there are only two useful singular values for 60 Hz and three for 120 Hz (Fig. 4.6). When thinking on elastography experiments, in order to determine N, a change in slope will be very hard to detect due to the small number of useful eigenvalues, being a consequence of the shear wavelength, control plane size and frequency bandwidth (10 Hz to 150 Hz) involved in the experiments.

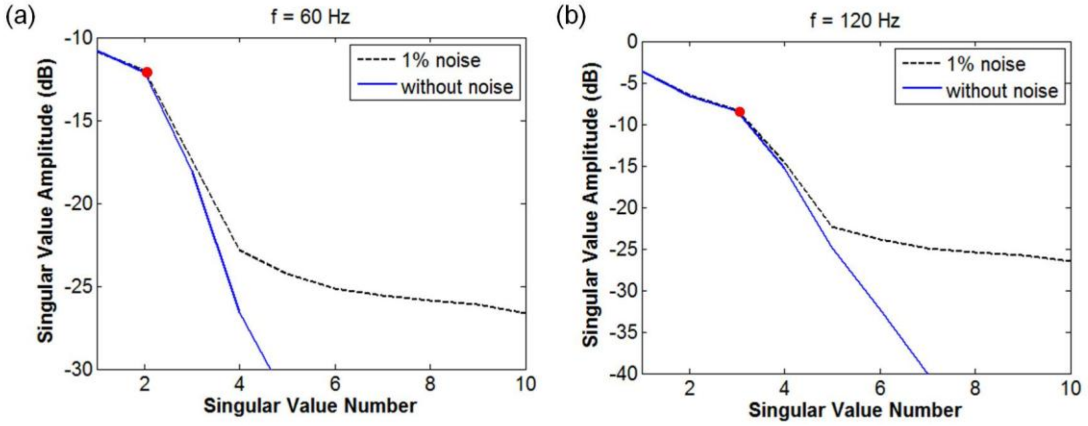

Fig. 4.6 Singular value distribution for (a) 60 Hz and (b) 120 Hz for the case of a vectorial wavefield. The full blue line is the singular value distribution obtained from the passive inverse filter from the simulated displacement field. The dashed black line is the singular value distribution obtained from the passive inverse filter from the simulated displacement field affected by noise within 1% in amplitude.

Another aspect that can make things more difficult, is the presence of noise in the experimental displacement field. To study the effect of noise, a random like signal was added to the simulated displacement field with an amplitude of 1% compared to the mean amplitude of the simulated displacement field. The effect of noise is observed in Figs. 4.4 and 4.6 as a rise in the singular value amplitude for the singular values associated to noise. The combined effect of a small number of useful singular values and the presence of noise will make even more difficult to distinguish between both slopes in the experiments. Thus, a preliminary estimation on the shear wave seems as the most adapted solution to determine N.

4.3: Application of the passive inverse filter to the elasticity imaging from complex reverberated field

In this section, the passive inverse filter will be applied for the shear wave speed tomography in the case of soft solids. Firstly, the use of the passive inverse will be presented in the simplest case of an homogeneous soft solid. Its advantages when compared to normalized/phase correlation and the problem of the eigenvalue number determination in such simple case will be discussed. Second, a more complex scenario will be considered: the use of passive inverse filter for elasticity imaging of heterogeneous media. The potential of the passive inverse filter for such application will be demonstrated for the same experiments presented in Chapter III: bi-layer solid, inclusion detection and *in vivo* passive elastography. For each experiment, the obtained results through passive inverse filter will be discussed and compared to the ones obtained through normalized/phase correlation.

4.3.1 Passive inverse filter in an homogeneous soft solid

The experiment is the same as described in Chapter III, section 3.3. An homogeneous PVA phantom is submitted to finger impacts during 9 seconds. The displacement field was recorded by means of ultrasound at a 1000 Hz sampling rate. The imaging plane consists of 35 points along z-axis spaced by 0.83 mm and 64 points along the x-axis spaced by 0.77 mm (Fig. 4.7(a)), resulting in an imaging surface A_{imag} equal to 1.41 x 10^3 mm^2. The phantom was previously characterized by 1D transient elastography resulting in a shear wave speed estimation of 1.4 ± 0.1 m/s.

For the passive inverse filter a window length of 100 ms was used. Then for computing the ideal focusing Eq. 4.16 was used. It is important to point that Eq. 4.16 is for a given frequency. Thus the temporal frequency dominating the spatial focalization in the case of the passive inverse filter is known. The result of having a monochromatic focalization, can be explained by the fact that the passive inverse filter enables to control the pseudo-sources represented by each window, although during the experiment the real sources were not controlled. This is a great advantage when compared to normalized/phase correlation where the computed time reversed field is composed of multiple frequencies. The frequency control through passive inverse filter will be exploited in Chapter V for spectroscopy experiments. In Fig. 4.7(a) the focalization for a 60 Hz frequency is presented along with its -6dB contour in black. In Fig. 4.7(b) the singular value distribution obtained for 60 Hz is presented. The red dot indicates the number $N = 10$ of singular values used to compute the inversion. This number was estimated based on Eq. 4.19 using the 1D transient elastography shear wave speed estimation, the imaging surface A_{imag} and assuming a non dispersive medium. As it was done in Chapter III, from the -6 dB contour the shear wave speed can be estimated by using Eq. 3.32, which relates the mean radius to the shear wave speed for a single frequency. A mean shear wave speed estimation of 1.52 ± 0.03 m/s is obtained by averaging the shear wave speed estimation from the -6 dB contour over the imaging plane. The result is in good agreement with the 1D transient elastography estimation.

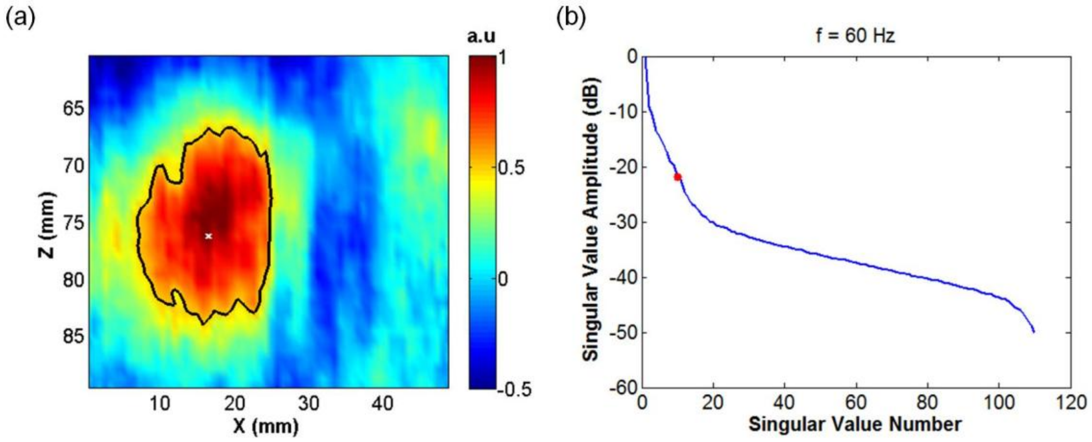

Fig. 4.7 (a) Focalization using passive inverse filter for a 60 Hz frequency in an homogeneous phantom using 10 singular values. The -6dB contour in black is also presented. (b) Experimental singular value distribution obtained for a 60 Hz frequency. The red dot indicates the number N = 10 of chosen eigenvalues.

When comparing the experimental singular value distribution (Fig. 4.7(b)) to the simulated singular value distributions (Figs. 4.4 and 4.6) no strong plateau is observed before arriving to the number N. The experimental singular value distribution does not decrease in a strong step-like form when arriving to N, instead it decreases linearly. This fact can be attributed to noise present in the acquired displacement field as shown in Fig. 4.6 (black dashed line), making it very difficult to distinguish between the image and the kernel of the transfer matrix $\breve{H}$. On the other hand when computing N through Eq. 4.19 a prior estimation on the wave speed is needed, which is usually affected by error, resulting in an uncertainty in N. Thus, the following question arises: what are the consequences, on the shear wave speed estimation, of a misleading estimation on the number N of useful eigenvalues ?

The relative error on the shear wave speed estimation can be related to the relative error on the eigenvalue number through Eq. 4.19 as follows:

$$\Delta N/N = 2\Delta c/c \tag{4.22}$$

Based on the transient elastography estimation, the relative error on the shear wave speed estimation is approximately 7%, leading to relative error on N of 14%, thus $N \cong 10 \pm 2$ for a 60 Hz frequency. By averaging the shear wave speed estimation from the -6 dB contour over the imaging plane, mean shear wave speed estimations of 1.52 ± 0.03 m/s, 1.38 ± 0.03 m/s, 1.67 ± 0.02 m/s were found for 10, 12 and 8 singular values respectively. Thus, the variability on the shear wave estimation due to an error on the determination of the singular value number, is greater than the variability of the local shear wave speed estimation. This variability can be estimated in this case to be approximately 0.15 m/s. Then, the final shear wave speed estimation for a 60 Hz frequency is 1.52 ± 0.15 m/s in complete agreement with the transient elastography estimation. This variability of 10 % due to a possible error on the determination of N remains approximately constant for the frequency range in the experiments presented along this manuscript. Thus, each shear wave speed estimation through passive inverse filter will be considered to be affected by approximately 10% of error due to an uncertainty in N.

The temporal frequency control of the spatial focalization is not the only advantage of the passive inverse filter when compared to normalized/phase correlation. Another consequence of the pseudo-source control through the passive inverse is the spatial isotropy of the time reversed field. In Chapter III, section 3.3.5, it has been observed, for the time reversed field computed using correlations, that the converging wavefront in the focalization step propagates along a given direction, instead of enwrapping the focal point as it is expected for a perfect time reversal experiment (Fig. 3.25). This is a consequence of sources in the noise experiments are not homogeneously distributed over the phantom's surface. From a time reversal point of view, instead of having a perfect time reversal cavity, we have a time reversal mirror.

It has already been shown that the passive inverse filter corrects the anisotropy in the case of seismic data [93]. In [93] for the computed time reversed fields a spatial average over the different focal points was performed. Below, I will demonstrate that the problem of anisotropy is also locally corrected (without spatial average) in the case of the elastography noise experiments. Thus, for the passive inverse filter diffraction effects will practically be eliminated leaving only the near field effects present in any time reversal experiment involving shear waves. As a consequence, the spatial resolution of the shear wave speed maps will be increased, leading to a better detection of inclusions embedded in a larger medium as it will be demonstrated in section 4.3.3.

In Fig. 4.8 the focalization movie using phase correlation (Fig. 4.8(a)) and passive inverse filter (Fig. 4.8(b)), for the homogeneous phantom, are presented. For the passive inverse computation, a summation over a frequency bandwidth ranging from 40 Hz to 120 Hz was performed. For each frequency component Eq. 4.19 was used to estimate the number of useful eigenvalues. For the phase correlation computation the frequency band chosen is the same as for the passive inverse filter computation. Six different instants are presented in Fig. 4.8, where the focalization time is set equal to zero. The black arrows indicate the wavefront main propagation direction. It is clearly observed for the field computed through the passive inverse filter how the wavefront enwraps the focal point (indicated with a white cross). Contrary, for the field computed trough phase correlation (Fig. 4.8(a)), the wave front propagates mainly along a given direction.

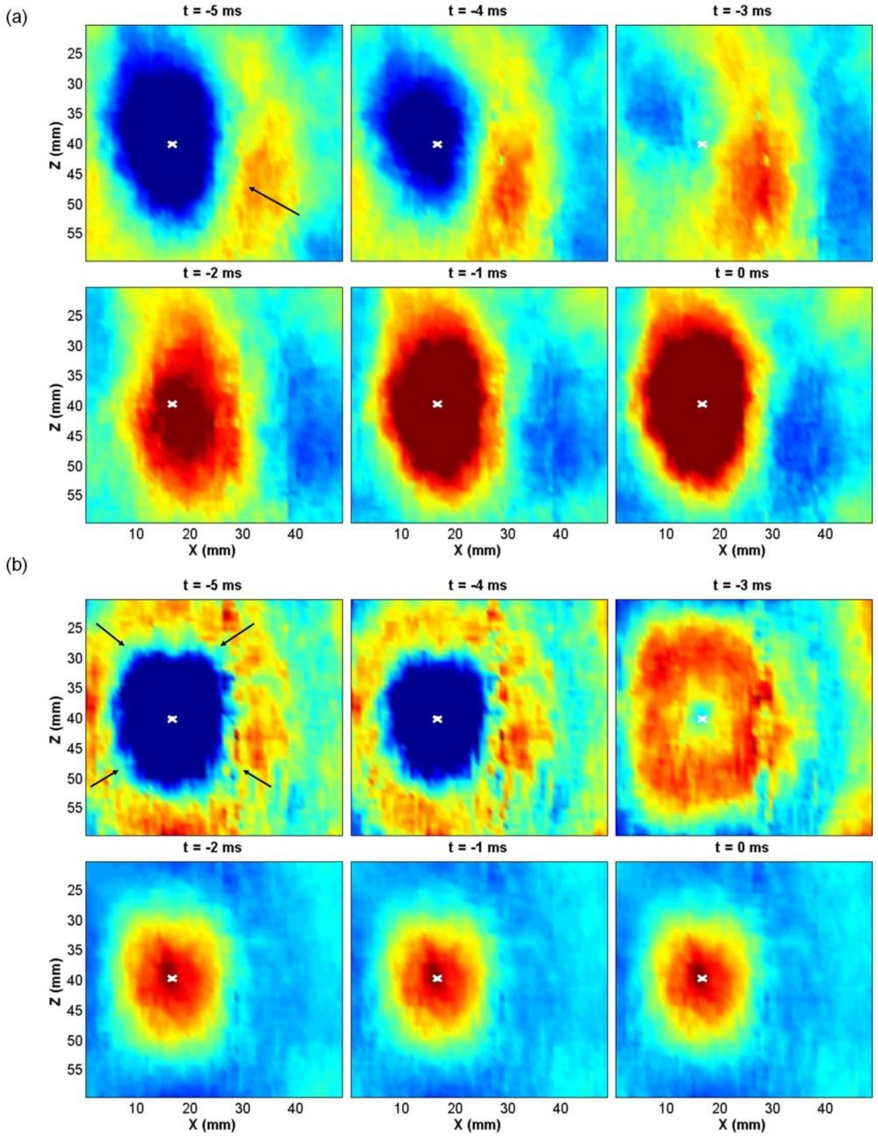

Fig. 4.8 Focalization movie using (a) phase correlation and (b) passive inverse filter. Five instants before the focalization time set equal to zero are presented. The black arrows at -5 ms indicate the wavefront main propagation direction. It is clearly observed how the wavefront enwraps the focal point indicated with a white cross for the case of the passive inverse filter.

In this section, the two main advantages of the passive inverse filter compared to normalized/phase correlation where presented: the frequency and spatial control of the time reversed field. The frequency control will be exploited in Chapter V to conduct passive shear wave spectroscopy experiments. The spatial control, which results in a more isotropic focalization, will be exploited below for shear wave speed tomography of heterogeneous media.

4.3.2 Passive inverse filter in an heterogeneous bi-layer medium: the effective shear wave speed

In this section, the passive inverse filter will be applied in the case of an heterogeneous bi-layer phantom for shear wave speed imaging purposes. The experiment as well as the recorded displacement field are the same as in section 3.3.2. In the previous section, the number N of useful eigenvalues was established through Eq. 4.19, valid only in the case of an homogeneous medium. Thus, for an heterogeneous medium how is it possible to determine the number N?

Let us assume that the medium we would like to image is composed of two layers as the phantom used in the experiment: a hard and a soft layer. Based on the interpretation that the total number of useful eigenvalues N_T is given by the number of independent focal spots on a given surface, the number N_T can be written, in a first approximation, as the sum of the number of independent focal spots in the hard and soft layer:

$$N_T \approx N_H + N_S \tag{4.23}$$

Where N_H and N_S are the number of independent focal spots in the hard and soft medium respectively. By combining Eq. 4.19 and Eq. 4.23 the number of degrees of freedom can be expressed as:

$$N_T \approx \frac{4\pi\sqrt{2}}{5}\left(\frac{A_H}{c_H^2} + \frac{A_S}{c_S^2}\right)f^2 = \frac{4\pi\sqrt{2}}{5}\frac{A_{imag}}{c_{eff}^2}f^2 \tag{4.24}$$

Where A_H, c_H and A_S, c_S are the shear wave speed and the surface occupied by the hard/soft phantom respectively, A_{imag} is the total imaging surface and c_{eff} is an effective shear wave speed. The effective shear wave speed, defined on the second equality in Eq. 4.24, can be interpreted, as the shear wave speed of an homogeneous equivalent medium should have to obtain N_T focal spots on a surface A_{imag}.

For the bi-layer phantom, based on the B-mode image of the medium (Fig. 3.10(a)) the surfaces occupied by the hard and soft layer are approximately 803 mm^2 and 667 mm^2. From the shear wave speed estimations through transient elastography and Eq. 4.24, an effective shear wave speed of $c_{eff} \approx$ 1.8 m/s is calculated. In Fig. 4.9, the shear wave speed maps obtained using passive inverse filter with a window length of 200 ms at a 60 Hz frequency for different contour levels are presented. The number N_T was calculated from Eq. 4.24 using a c_{eff} = 1.8 m/s. Since for the passive inverse filter the frequency is known, in order to retrieve the shear wave speed from the mean radius measurement Eq. 3.32 is used. In Fig. 4.9 (a) - (c), the shear wave speed maps obtained from a 0.4, 0.6 and 0.8 contour level are respectively presented. In all the cases, the two layers are clearly visible in agreement with the images obtained through normalized/phase correlation. Mean shear wave speed values of 1.36 ± 0.13 m/s and 3.69 ± 0.09 m/s, 1.29 ± 0.05 m/s and 3.71 ± 0.10 m/s, 1.35 ± 0.13 m/s and 4.11 ± 0.26 m/s were found for the top and bottom layer for the 0.4, 0.6 and 0.8 contour level respectively. In Fig. 4.9 (d) the final result for 60 Hz is calculated as an average of the shear wave speed maps over different contour levels ranging from 0.4 to 0.8 by a 0.1 step. A mean shear wave speed values of 1.32 ± 0.08 m/s and 3.80 ± 0.09 were found for the top and bottom layer respectively. All the presented values agree within the error margin with the 1D transient elastography estimation, as well as with the estimation through normalized/ phase correlation.

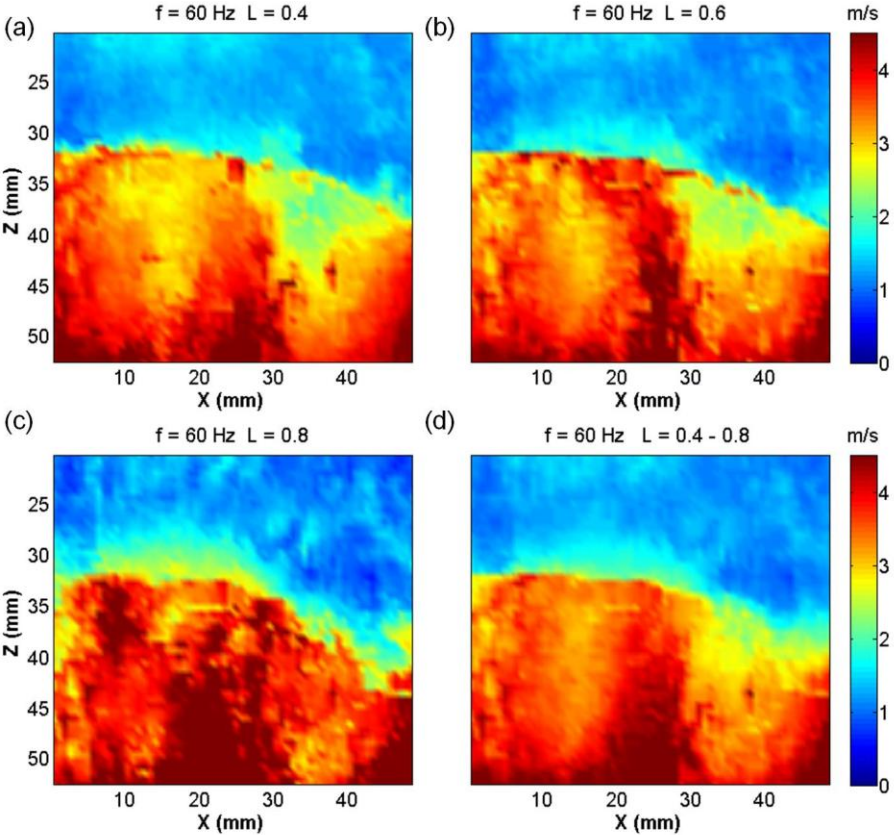

Fig. 4.9 Shear wave speed maps at 60 Hz obtained using passive inverse filter with a $c_{eff} = 1.8$ m/s for different contour levels (a) 0.4 (b) 0.6 (c) 0.8. For (d) an average on the obtained shear wave speed maps using different contour levels (from 0.4 to 0.8) was performed.

However, the different contour levels is not the only information that can be used with the passive inverse filter for constructing shear wave speed maps. Since the temporal frequency is controlled leading to a monochromatic focalization, a shear wave speed map for each frequency component can be obtained. In Fig. 4.10 (a)-(c) the shear wave speed maps obtained using passive inverse filter for different frequencies ranging from 50 Hz to 90 Hz are presented. For each shear wave speed map an average over different contour levels was performed. It is important to note that the higher the frequency is, the noisier the images are. This behavior is expected since in the noise experiments it is very difficult to achieve high frequencies, thus at 90 Hz a noisier image is obtained due to the lack of energy. Mean shear wave speed values of 1.37 ± 0.13 m/s and 3.44 ± 0.08 m/s, 1.25 ± 0.07 m/s and 3.70 ± 0.17 m/s, 1.10 ± 0.08 m/s and 3.82 ± 0.20 m/s were found for the top and bottom layer for 50 Hz, 70 Hz and 90 Hz respectively.

In Fig. 4.10 (d) the final result is calculated as an average of shear wave speed maps over different contour levels (from 0.4 to 0.8 by a 0.1 step) and the different frequencies (from 40 Hz to 100 Hz with a 10 Hz step). For the final result mean shear wave speed values of 1.21 ± 0.09 m/s and 3.83 ± 0.12 were found for the top and bottom layer respectively. By taking into account the error due to a miss-estimation on the number N of useful eigenvalues, the final results can be expressed as 1.2 ± 0.1 m/s and 3.8 ± 0.4 m/s for each layer respectively. Again the obtained values agree within the error margin with the 1D transient elastography estimation as well as with the estimation through phase/normalized correlation.

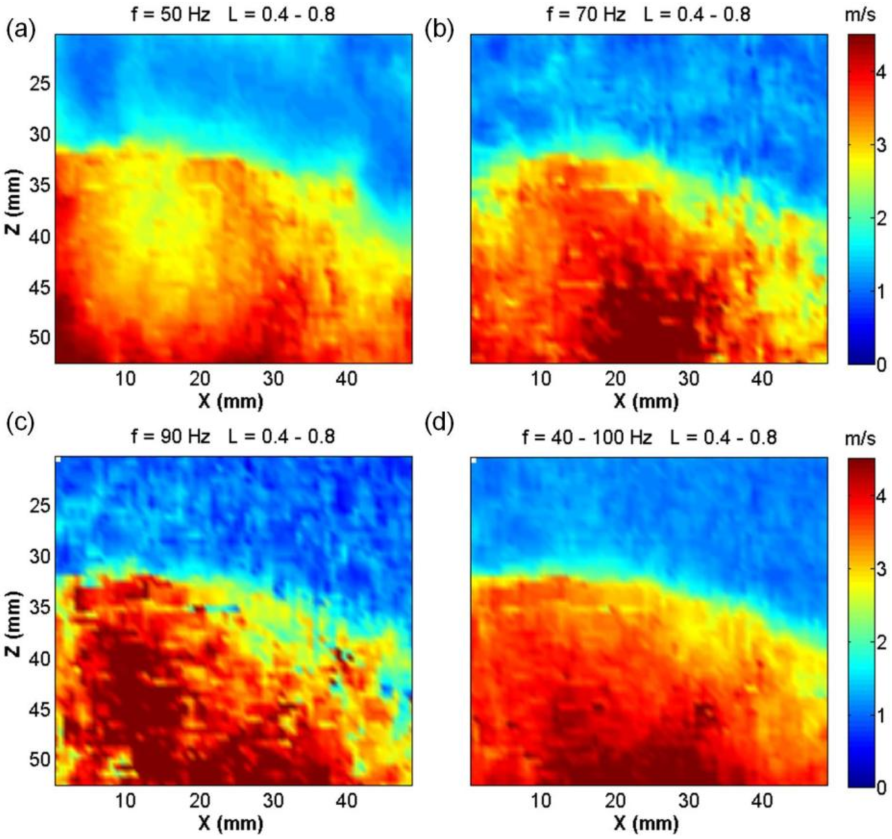

Fig. 4.10 Shear wave speed maps obtained using passive inverse filter with a $c_{eff} = 1.8$ m/s for different frequencies (a) 50 Hz (b) 70 Hz (c) 90 Hz. For the final result (d) an average over a frequency range from 40 Hz to 100 Hz was performed. For all the shear wave speed maps an average over different contour levels (from 0.4 to 0.8) was also performed.

In this section, the potential of the passive inverse filter for elasticity imaging of a bi-layer medium was demonstrated. The main drawback of the technique for a quantitative elasticity estimation lies in the determination of c_{eff}, depending the latter through Eq. 4.24 on the size, as well as on the shear wave speed value of each layer. Thus, in the case of the elastography experiments, an estimation of c_{eff} will imply a complete prior knowledge of the problem. In practical applications a possible solution for estimating c_{eff} is to combine the information present on the B-mode image and some prior elasticity estimation, which can be obtained through phase/normalized correlation, 1D transient elastography or from the available literature. In the worst scenario, where no prior information is available, neither from the echographic image nor from a previous shear wave speed estimation, the passive inverse filter has a free parameter which can be changed until the desired result is obtained. This different approaches will be tested in the followings sections in order to retrieve quantitative shear wave speed maps.

However, despite an estimate of c_{eff} is necessary for retrieving a quantitative elasticity image, this latter is not necessary for obtaining a relative elasticity image. In Figs. 4.11 (a) and (b) the shear wave speed maps obtained for the bi-layer solid using a c_{eff} = 2.5 m/s and 1.5 m/s are respectively presented. The ratio between the mean shear wave speeds in the soft and hard part of Fig. 4.11 are 3.0 ± 0.3 and 2.8 ± 0.3 m/s which agree within the margins of error with the 2.7 ± 0.3 value calculated from the 1D transient elastography estimation

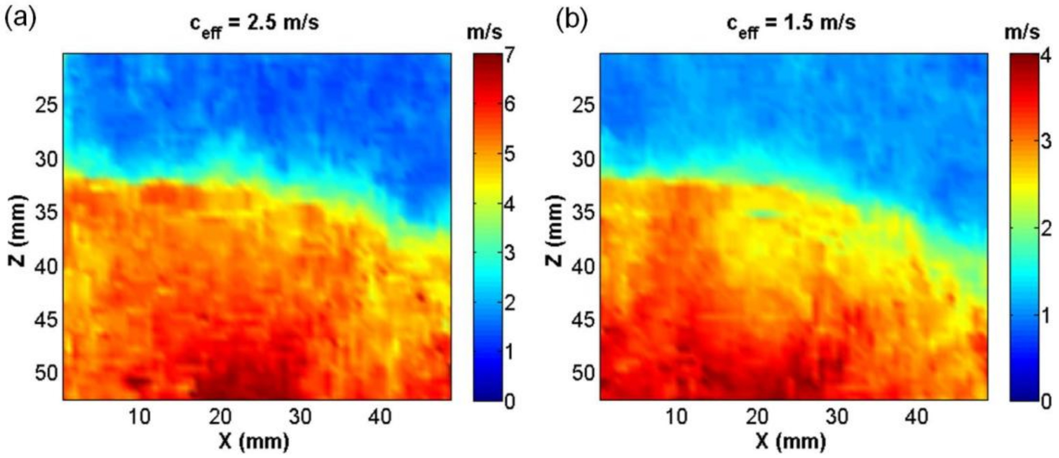

Fig. 4.11 Relative shear wave speed maps obtained from passive inverse filter (a) c_{eff} = 2.5 m/s and (b) c_{eff} = 1.5 m/s.

To conclude this section the results obtained through passive inverse filter will be compared to the ones obtained through normalized/phase correlation. In Fig. 4.12 the shear wave speed maps obtained through normalized correlation, phase correlation and passive inverse filter are presented. Despite that for normalized/phase correlation the hard part of the bi-layer phantom is more homogeneously imaged than in the case of the passive inverse filter, no big differences are observed between the different shear wave speed maps. Thus, the anisotropy of the time reversed field computed through correlation is not prohibitive for elasticity imaging of a bi-layer medium. This will be not the case, when imaging small inclusions embedded in a larger medium as it will be demonstrated below.

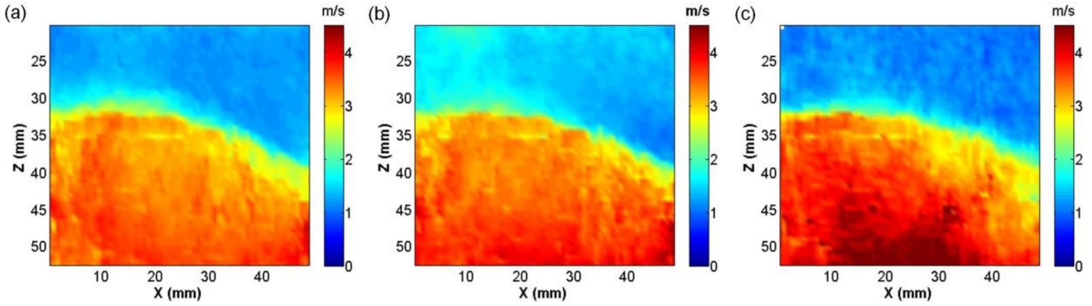

Fig. 4.12 Comparison between the shear wave speed maps obtained through (a) normalized correlation, (b) phase correlation and (c) passive inverse filter in the case of a bi-layer medium.

4.3.3 Inclusion imaging with the passive inverse filter

In section 4.3.1 it has been observed, for the case of the time reversed field computed using correlations, that the converging wavefront in the focalizing step propagates along a given direction instead of enwrapping the focal point as it is expected for a perfect time reversal cavity. As a consequence of this problem the inclusions in section 3.3.5 could not be satisfactory resolved leading to several image artifacts in Fig. 3.24(b). In section 4.3.1 it was demonstrated that the problem of an anisotropic focalization is corrected by using the passive inverse filter. As a consequence the spatial resolution of the shear wave speed maps will be increased as it will demonstrated below, while using the passive inverse filter to image small inclusions embedded in a larger medium.

The experiment is the same as described in section 3.3.5. The phantom used in the experiment contained two cylindrical inclusions, one harder (≈ 10 mm diameter) and one softer (≈ 14 mm diameter) than de background (BG). A final shear wave speed of 2.2 ± 0.3 m/s, 4.1 ± 0.3 m/s and 2.9 ± 0.3 m/s were found for the soft inclusion, the hard inclusion and the BG respectively by applying an independent transient elastography technique.

Previously, when retrieving the shear wave speed maps in the case of the bi-layer phantom, the effective shear wave speed needed in order to estimate N, was calculated based on prior available information: layer sizes and shear wave speeds. In order to test the applicability of the passive inverse filter as an independent elastography technique, a different approach will be used in this section. Let us assume that no prior information on the inclusions size and shear wave speeds is available, as it is usually the case for elastography. This leaves c_{eff} as an independent parameter in the passive inverse filter. The effective shear wave speed is then varied between 1.5 m/s to 4 m/s with a 0.1 m/s step. For each c_{eff} value a shear wave speed map was retrieved. In Fig. 4.13, the obtained images for c_{eff} = 1.8 m/s and 3.5 m/s are presented. A 200 ms window length was used for the passive inverse filter computation. To retrieve the shear wave speed from the spatial focalization, the surface enclosed by a given isolevel curve at a fixed frequency was used (Eq. 3.30) instead of the mean radius used previously. For the final shear wave speed map, an average over different contour levels ranging from 0.5 to 0.7 and different frequencies (90 Hz - 150 Hz) was performed.

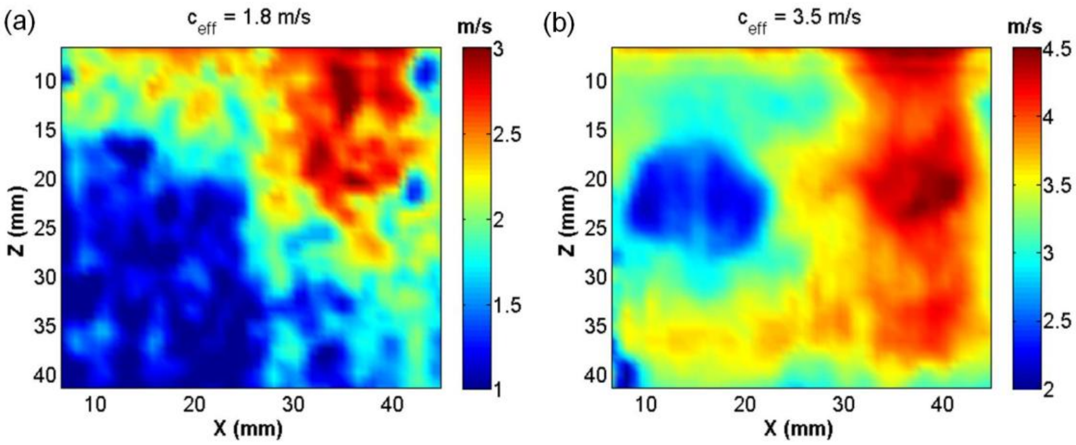

Fig. 4.13 Shear wave speed maps computed through passive inverse filter for the inclusion detection experiment for an effective shear wave speed of (a) 1.8 m/s and (b) 3.5 m/s.

For the shear wave speed map obtained using a c_{eff} = 1.8 m/s (Fig. 4.13(a)), the hard inclusion is visible, while the soft inclusion is not well defined. Contrary, in the shear wave speed map obtained using a c_{eff} = 3.5 m/s (Fig. 4.13(b)) the soft inclusion clearly emerge from the background while the hard inclusion appears more diffuse. It is worth noticing, that for both shear wave speed maps the ratio between the shear wave speed value of the inclusions and background remains approximately the same, no matter the effective speed value. Thus, despite a miss estimation in c_{eff} a good relative shear wave speed map is obtained. This fact was already observed in the case of the bi-layer medium. However, for the present case all the available degrees of freedom should be used in order to have both inclusions simultaneously well defined.

The criteria used in order to select the final image, was to observe both inclusion simultaneously with the highest spatial definition possible. Thus, based on Fig. 4.13, one should expect that both inclusions will be visible for a c_{eff} lying between 1.8 m/s and 3.5 m/s. Best results were found for a $c_{eff} = 2.6$ m/s. The obtained shear wave speed map as well as the sample's B-mode image are presented in Fig. 4.14. The inclusions positions are marked with a black dotted line. Both inclusions clearly emerge from the background in Fig. 4.14(b). Mean shear wave speed of 2.1 ± 0.2 m/s, 3.8 ± 0.4 m/s and 3.0 ± 0.3 m/s were found for the soft inclusion, the hard inclusion and the BG respectively in good agreement with the independent transient elastography estimations. For the errors margins provided, an error of 10 % in misestimating N due to a misestimation on c_{eff} was assumed.

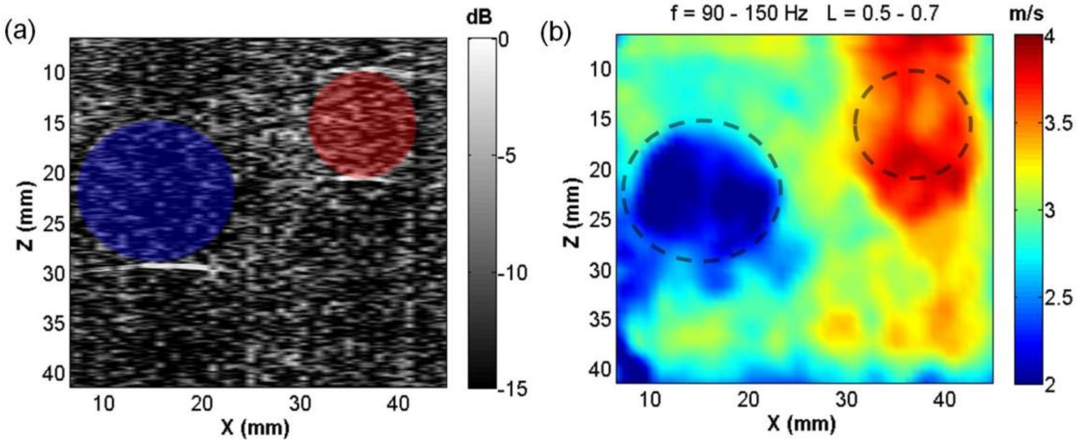

Fig. 4.14 (a) Sample's B-mode image. The red and blue circles indicate the hard and the soft inclusion position respectively. (b) Shear wave speed map obtained through passive inverse filter with $c_{eff} = 2.6$ m/s and a frequency band between 90 Hz to 150 Hz. An average for levels ranging from 0.5 to 0.7 was performed. The inclusion position is marked with a black dotted line.

When looking at the positions of the inclusions in Fig. 4.14(b), the soft inclusion position coincides with the position predicted in the B-mode image. However, a small deviation is observed for the upper part (≈ 15 mm depth) when compared to the expected position (marked in black dashed black line). The soft inclusion appears ≈1 mm deeper than it should be expected. For the hard inclusion, stronger deviations in the boundary determination of ≈ 3 mm when compared to the echographic image are observed. These deviations on the boundary determination were already observed in the bi-layer phantom for the shear wave speed maps obtained through normalized/phase correlation and passive inverse filter (Figs. 3.13, 3.16 and 4.12). For those cases, the boundary between both layers appeared ≈ 3 mm deeper in the echographic image than in the shear wave speed map. This miss-determination on the boundaries can be explained based on the algorithm used to extract the shear wave speed from the mean radius or surface. The situation is schematized in Fig. 4.15(a). When arriving from a soft medium with the focal point (marked with a white cross) the spatial focalization "senses" the hard medium. However, the influence of the hard medium remains unappreciable in the mean radius/surface computation until a given critical distance (middle Fig. 4.15(a)), where although the focal still lies in the soft part, some of it lies in the hard part. This influences the mean radius/surface measurement, leading to a higher mean radius/surface estimation than expected. This results in an overestimation on the shear wave speed. The effect is more appreciable the higher the shear wave speed contrast between both mediums is. This is the reason, why this effect is more appreciable in the hard inclusion than in the soft inclusion. In Fig. 4.15 (b) the experimental situation is presented for the case of phase correlation applied to the bi-layer medium. The black contour corresponds to a 0.6 isolevel curve.

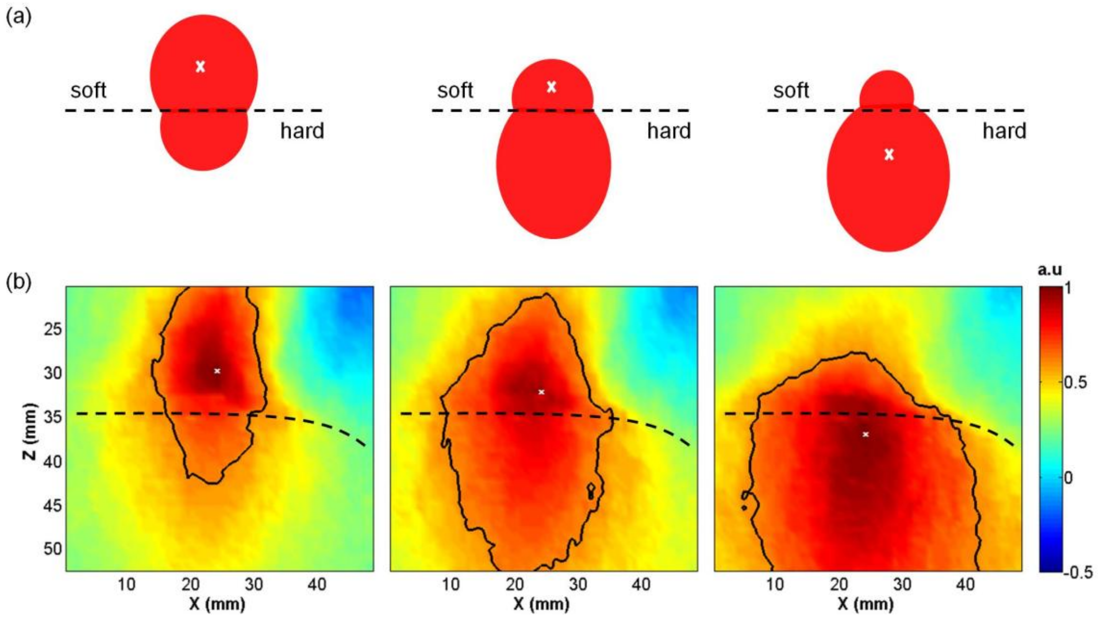

Fig. 4.15 (a) Schematic representation of the effect of focalizing through an heterogeneous medium. The focal point is indicated by a white cross while the focal surface for a given level is indicated in red. The spatial focalization senses the hard medium when coming from the soft medium. However this effect is not appreciable until a given distance which depends on the shear wavelengths involved. (b) Experimental situation when using phase correlation in the bi-layer phantom. The 0.6 isolevel curve is indicated in a black full line. The border between both layers is indicated in a black dashed line.

To conclude this section the results obtained through passive inverse filter will be compared to the ones obtained through normalized/phase correlation. As stated in section 3.3.5, inclusion detection was prohibitive when using normalized cross correlation due to the combined effects of the low frequency content and the anisotropy of the time reversed field. Using phase correlation higher frequency components can be enforced, however, this alone was not enough to have an acceptable image spatial resolution. In Fig. 4.16 the images obtained through phase correlation (Fig. 4.16(a)) and passive inverse filter (Fig. 4.16(b)) are presented. In both cases the shear wave speed values retrieved agree with the ones obtained by transient elastography, however, in the image obtained through phase correlation several image artifacts appear resulting in a poor resolved soft inclusion. As a consequence of this image artifacts, it is difficult to deduce the presence of only two inclusions from Fig. 4.16(a). One may think that three inclusions are present: a very well defined hard inclusion and two softer inclusions, one at $z \approx$ 15 mm depth and another one at $z \approx$ 30 mm depth. This is not the case for the shear wave speed map obtained through passive inverse filter where the presence of two inclusions is clearly visible. Thus, when thinking in practical medical applications, the image obtained through passive inverse filter is better, since only two inclusions are identified, although the hard inclusion is less defined than in the phase correlation shear wave speed map.

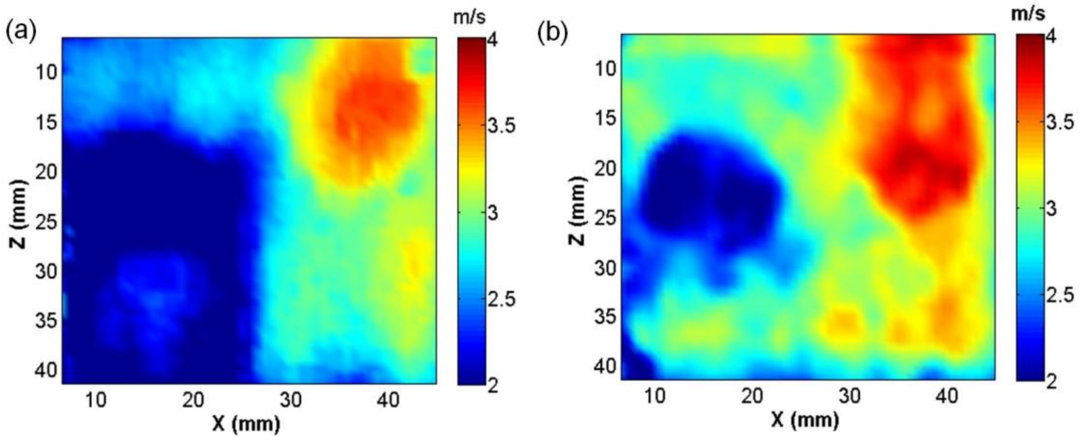

Fig. 4.16 Comparison between the shear wave speed maps obtained through (a) phase correlation and (b) passive inverse filter in the case of inclusions embedded in a larger medium.

4.3.4Passive inverse filter using physiological noise: a performance test in the liver.

To conclude this section, the performance of the passive inverse filter will be tested for the same passive elastography experiment described in section 3.3.4. For the passive computation a window length of 200 ms was used. In order to estimate the effective shear wave speed (Eq. 4.24), a combination between the information conveyed by the B-mode image and the literature was used. While the surface occupied by the muscle and the liver was estimated from the echographic image (Fig. 3.22), the shear wave speeds for muscle and liver were estimated from [61] and [38] respectively. An effective shear wave speed of c_{eff} = 1.2 m/s was obtained, very close to the shear wave speed value for the liver. This can be explained since the imaging plane is mostly occupied by the liver. In Fig. 4.17 (a) and (b) the spatial focalization using passive inverse filter is presented in the muscle and in the liver respectively along with its 0.6 isolevel curve in black. The white cross indicates the focal point.

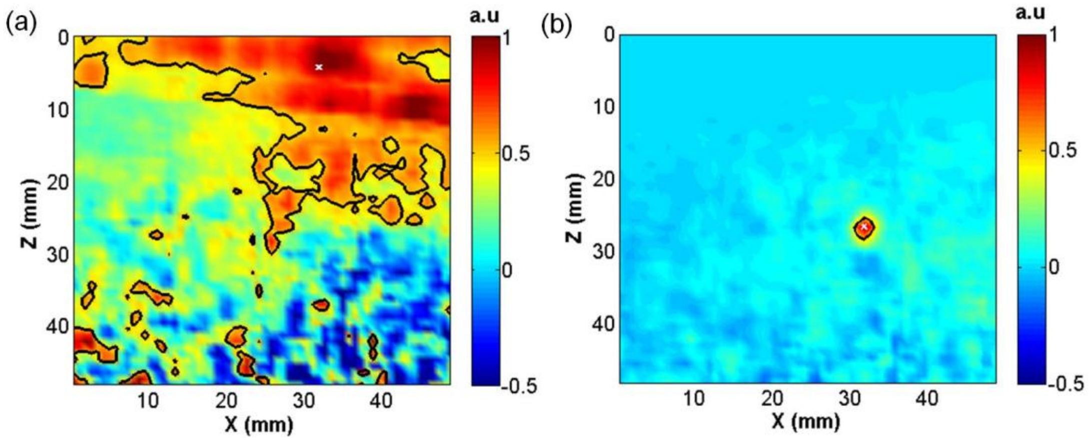

Fig. 4.17 Spatial focalization using passive inverse filter in (a) muscle and (b) liver for the passive elastography experiment. The 0.6 isolevel curve is presented in black full line. The focal point is indicated by a white cross.

From Fig. 4.17. while focusing in the liver results in a good defined focus, the focus in the muscle is very noisy. As a consequence, the boundary between liver and muscle is not good resolved in the shear wave speed maps and an overestimation on the muscle shear wave speed is obtained. A possible solution to this problem is to increase the level chosen for the shear wave speed retrieval, however, this problem persists on higher contour levels. Thus, an alternative way to measure the shear wave speed near the focal point is needed.

In order to solve this problem, let recall the analytical expression for the spatial focus for a single frequency in the case of a soft solid approximation (Eq. 3.33) :

$$\chi(r,\theta,\omega) = \frac{1}{12\pi\mu}\frac{\omega}{c_T}\left\{2\left[1-\frac{(\omega.r)^2}{5.c_T{}^2}\right]+\frac{1}{5}\left(\frac{\omega.r}{c_T}\right)^2\cos^2(\theta)\right\} \tag{4.25}$$

From Eq. 4.25 the normalized spatial focalization along the x - axis ($\theta = \pi/2$) and z - axis ($\theta = 0$) are given by Eqs. 4.26a and 4.26b respectively.

$$\chi(x,\omega) = 1-\frac{1}{5}\left(\frac{\omega}{c_T}x\right)^2 \tag{4.26a}$$

$$\chi(z,\omega) = 1-\frac{1}{10}\left(\frac{\omega}{c_T}z\right)^2 \tag{4.26b}$$

As it is expected, for both axis the obtained focalization profile corresponds to the one of a parabola but with different curvatures. Thus, by fitting a parabola in the vicinity of the focal point a direct estimation of the shear wave speed can be obtained from the quadratic coefficient of the fit. Let S_x and S_z be that coefficient for the x - axis and z - axis respectively, then the shear wave speed can be derived from Eq. 4.26 as:

$$c_T = 2\pi f\sqrt{-\frac{1}{4.S_x}} \tag{4.27a}$$

$$c_T = 2\pi f\sqrt{-\frac{1}{10.S_z}} \tag{4.27b}$$

The coefficients S_x and S_z correspond to the second derivate in space of Eq. 4.26. Based on this observation, two equivalent interpretations can be given to the aforementioned coefficients. From a geometrical point of view, they are equal to the spatial focalization curvature evaluated at the focal point set as zero. Based on this interpretation, obtaining S_x and S_z will be referred as a curvature measurement throughout this manuscript. From a wave field point of view, the coefficients S_x and S_z can be interpreted as the Laplacian of the time reversed field evaluated at the focal point position. Thus, in order to solve the inverse problem from the time reversed field the square root of the inverse of the Laplacian should be computed. This can be interpreted as inverting the wave equation in order to solve for the shear wave speed.

The obtained shear wave speed map through Eq. 4.27a is presented in Fig. 4.18 along with its echographic image. For the quadratic fit eight points around the focal point were used. An average over a frequency range from 50 Hz to 150 Hz was performed for the final result.

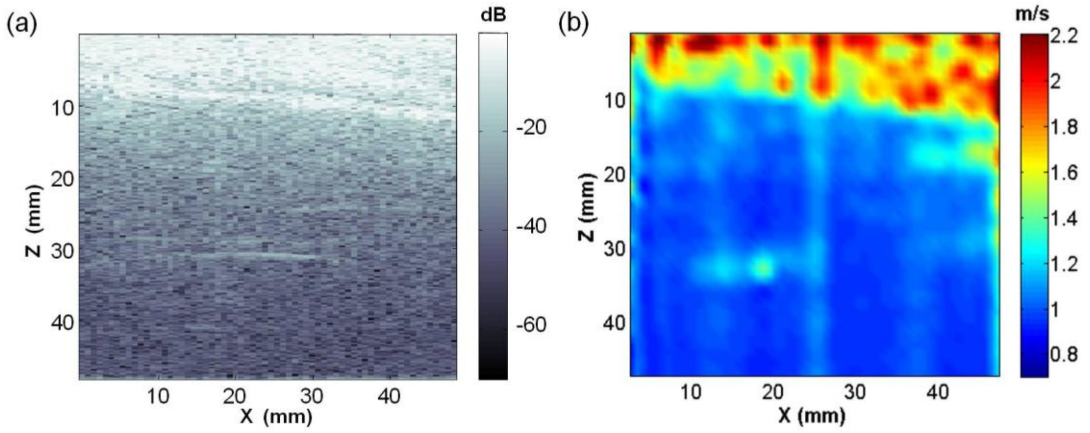

Fig. 4.18 Shear wave speed map obtained through passive inverse filter in the *in vivo* passive elastography experiment, compared to the B-mode image on the left. On the shear wave speed map, muscle and liver are clearly apparent. The boundary between both tissues coincides with the one observed in the echographic image.

On the shear wave speed map (Fig. 4.18(b)), belly muscle and liver are clearly apparent. Mean shear wave speed values of 0.95 ± 0.03 m/s and 1.54 ± 0.06 m/s were found for the liver and muscle respectively, in agreement with the reported results in the literature and the obtained values through phase correlation.

Another important aspect to notice in Fig. 4.18(b) is that the boundary between both tissues coincides perfectly with the one observed in the echographic image. No error in the boundary determination is observed as in the case of the *in vitro* experiments. This verifies that the cause of error in the boundary determination was in fact the algorithm used, as explained in the preceding section. By measuring the curvature on the focal point, a more local estimation of the shear wave speed is obtained, leading to better spatially resolved images.

4.4: Conclusions

In this Chapter, a novel technique, based on an adaptation of the inverse filter to a passive source configuration was presented: the passive inverse filter. This novel technique presents two main advantages when compared to normalized/phase correlation: it corrects for the anisotropy of the time reversed field and the temporal frequency dominating the spatial focalization is controlled. The main drawback of this technique for quantitatively elasticity estimation lies in the determination of the number N of useful eigenvalues, or equivalently in the determination of c_{eff}. Throughout this Chapter several strategies were presented in order to estimate c_{eff}. For the bi-layer phantom the effective shear wave speed was estimated using combined information from the B-mode image and prior shear wave speed estimations. For the passive elastography experiment c_{eff} was estimated by using the echographic B-mode image and the reported shear wave speed values for the liver and muscle. Finally for the inclusion detection no prior information was used to estimate c_{eff}. For obtaining the final shear wave speed map c_{eff} was changed until a well resolved shear wave speed map was retrieved. In the worst scenario where the effective shear wave speed is miss-estimated a relative shear wave speed map is obtained. and the quality of the image can be controlled through c_{eff} without losing the image contrast.

When imaging bi-layer mediums (*in vitro* or passive elastography experiment) no big differences were observed between the retrieved shear wave speed maps through the passive inverse filter and normalized/phase correlation. However, for the passive elastography experiment, the passive inverse filter resulted more sensitive to noise present in the displacement field than phase correlation.

Contrary to what happens in bi-layer medium, big differences were observed between the shear wave speed maps obtained from passive inverse filter and phase correlation when trying to image small inclusions. Since the passive inverse filter corrects for the anisotropy of the time reversed, both inclusions could be satisfactory resolved, which was not possible through phase correlation.

In the following Chapter the frequency control on the spatial focalization through passive inverse filter (monochromatic spatial focalization) will be exploited to conduct a wave spectroscopy experiment.

Chapter V

Passive wave spectroscopy using the passive inverse filter

Wave dispersion most often refers to frequency-dependent effects in wave propagation. One observable effect when dispersion is present, consists in the wave phase velocity dependence with frequency (dispersion curve). Dispersive effects may have two main causes: geometric boundary conditions, as it is the case for guided wave propagation, or by interaction between the waves and the propagating medium, e.g. viscosity effects.

Several applications involve guided wave propagation to estimate different characteristics of the propagating medium. For example, in modal methods used for non destructive testing, ultrasonic waves are guided within plates and pipes in order to retrieve the mechanical properties of the systems through a dispersion model (e.g., measurement of Lamb wave velocity) [52]. Another example, already presented in Chapter II, is guided wave propagation inside thin layered soft tissue, which has shown to be an efficient way for retrieving the tissue biomechanical properties. Feasibility studies recently carried out in cornea [44] and the arterial wall [45], [51] demonstrates this fact. Moreover, unbounded shear wave propagation in tissues has also shown to be dispersive due to the presence of viscosity [94], leading to the concept of shear wave spectroscopy introduced by *Deffieux et al.* [61]. Thus, shear wave spectroscopy is a quantitative method to assess tissue's viscosity and elasticity by measuring the dispersion affecting the propagation of shear waves within the tissue.

In Chapter IV, a technique based on an adaptation of the inverse filter to a passive source configuration was presented: the passive inverse filter. This novel technique presents two main advantages when compared to normalized/phase correlation: it corrects for the directivity of the time reversed field and the temporal frequency dominating the spatial focalization is known. The first advantage was already exploited in the preceding Chapter, when imaging small inclusions embedded in a larger medium. In this Chapter, the advantage of having a monochromatic focalization will be used to measure wave dispersion from a complex reverberated field.

In order to understand and to demonstrate how the passive inverse filter is able to measure wave dispersion, firstly, a widely studied situation will be considered: guided wave propagation in metals. Thus, in a first step, a finite difference simulation is conducted in a metallic bar, where wave propagation is known to be highly dispersive. Secondly, in order to confirm the potential of the passive inverse filter to measure wave dispersion, an experiment is carried out in a stainless steel plate, where the complex reverberated field is known to be dominated by Lamb waves.

Once the ability of the passive inverse filter to conduct a wave spectroscopy experiment is demonstrated in metals, a more complex situation will be considered: measuring dispersive effects in the case of the elastography experiments. As stated above, in soft tissues dispersion causes are twofold: guided wave propagation, as it was introduced in Chapter II, and viscosity effects. Both situations will be considered when measuring dispersive effects in a soft solid thin layer and while conducting an *in vivo* passive shear wave spectroscopy experiment in the liver and muscle.

5.1: Wave spectroscopy from reverberated elastic field in metals

In this section the feasibility for conducting a wave spectroscopy experiment from a complex reverberated wave field will be studied in metals. For this purpose phase correlation and the passive inverse filter will be tested. In a first step, a finite difference simulation is conducted in a metallic bar, where wave propagation is known to be highly dispersive. Secondly, an experiment is carried out in a stainless steel plate where the complex reverberated field is known to be dominated by Lamb waves.

5.1.1 Simulation in a duralumin bar

The simulated experiment is the following: a 1 MHz central frequency sinusoid cycle excitation is applied to a 41.6 mm length duralumin bar. A schematic representation of the simulated experiment is illustrated in Fig. 5.1(a). The cross sectional area is negligible compared to the bar length and the wavelengths involved, thus, a one dimensional propagation is considered. The displacement field is acquired at a 10 MHz sampling rate during 616.6 μs in a control line consisting of 160 sensor, distributed along the bar. The spatial pitch between sensors was set to 0.26 mm. In Fig. 5.1(b) a zoom of the displacement field for the first 120 μs is presented. Two different zones can clearly be identified, one corresponding to the direct wave propagation and the other one to reverberations.

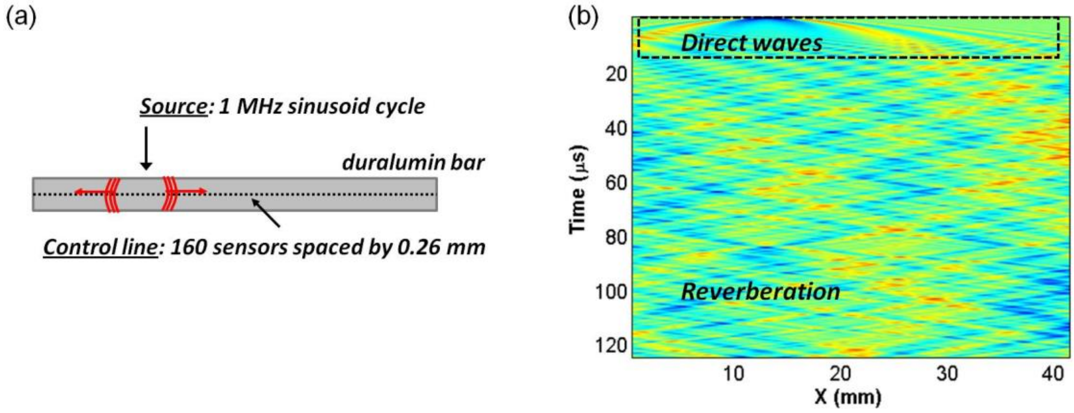

Fig. 5.1 (a) Schematic representation of finite difference simulation. A 1 MHz central frequency sinusoid cycle excitation is applied to a 41.6 mm length duralumin bar. The displacement field is acquired by 160 sensor distributed along the bar at 10 MHz sampling rate during 616.6 µs. The spatial pitch between sensors was set to 0.26 mm. (b) Simulated displacement field in a duralumin bar. Two zones can clearly be identified, one corresponding to the direct wave propagation and the second corresponding to the reverberated field.

For the direct wave propagation, which corresponds to the first 15 μs, dispersion is clearly visible, since high frequency components propagate faster than low frequency components. A usual way for measuring the dispersion curve from the direct wave propagation is by performing a two dimensional Fourier transform and finding for each frequency the phase velocity at which the Fourier transform's amplitude is maximal (for further details please refer to section 2.5.3).

However, if only the reverberated field is accessible, would it still be possible to extract the wave dispersion curve from the measured displacement field? Based on the work of *Benech et al.* [3], by using correlations interpreted in the frame of a time reversal experiment, two independent approaches for extracting the wave phase velocity from a reverberated field could be applied: the phase method and the focal width method (Chapter III, section 3.2.3). The phase method consists in measuring the phase of the converging wave in a time reversal/correlation experiment as a function of distance. On the other hand, the focal width method consists in measuring the shear wavelength from the focal spot width. Hereinafter, the phase method and the focal width method will be used to extract the wave dispersion curve by using the reverberated field in the simulated experiment. As reference, the extracted dispersion curve from the direct wave propagation will be used.

- Wave spectroscopy from phase correlation

The spatial-temporal correlation field shown in Fig. 5.2(a) was computed, from the reverberated part of field presented in Fig 5.1(b), by using phase correlation with a frequency band from 0.2 to 2 MHz. A spatial average over the different focalization points was performed for the final result. A remarkable difference is observed in the correlation field presented in Fig. 5.2(a) when compared to the correlation field in Fig. 3.6. The correlation field in Fig. 3.6 was computed for an homogeneous, isotropic medium, thus no strong dispersive effects were attended. The wave package travels without being dispersed, focalizing at the desired position. This is clearly not the case for Fig. 5.2(a). Since the wave propagation is highly dispersive, the different frequency components of the time reversed field travel different distances, due to its different phase velocities, in order to reach the focal spot at the same time.

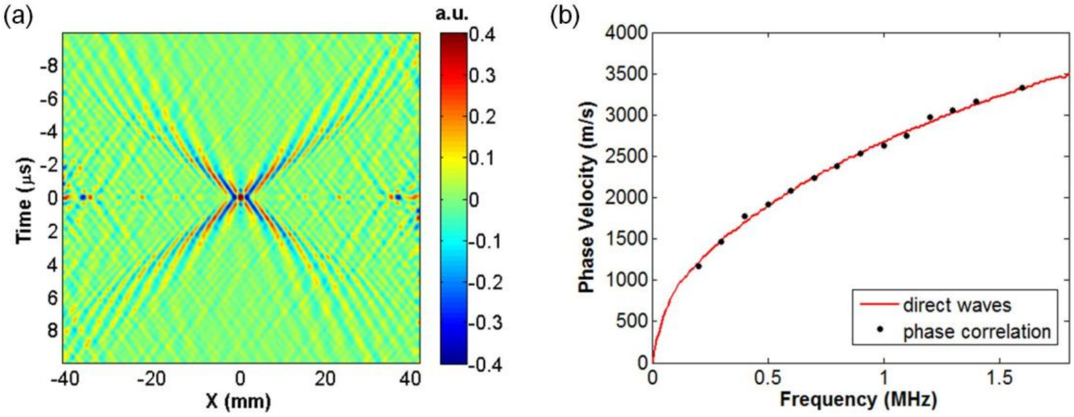

Fig. 5.2 (a) Correlation field computed using phase correlation (0.2 MHz - 2 MHz) from the reverberated part of the field presented in Fig. 5.1. (b) Comparison between the dispersion curve extracted from the correlation field (black dots) and the dispersion curve calculated from the direct wave propagation (red full line).

The dispersion curve is extracted from the spatial-temporal correlation field by performing a two dimensional Fourier transform and finding for each frequency, the phase velocity at which the Fourier transform amplitude is maximal (as introduced in section 2.5.3). The obtained result is presented in Fig. 5.2(b) in black dots. For comparison, the extracted dispersion curve from the direct wave propagation zone is also presented in Fig. 5.2(b) in a red full line. A complete agreement is found between both dispersion curves. Thus, the phase method could be used for extracting the dispersion curve from a complex reverberated field. However, as stated in section 3.2.3, its main drawback is its lack of robustness to low signal to noise ratio. Thus, for low signal to noise ratio the focal method is preferred, since it deals with the maximum energy at the focal spot. The main problem in the focal width method for wave spectroscopy experiments when computed through correlations, is the lack of control on the temporal frequency dominating the spatial focalization. Thus, the passive inverse filter is proposed as a solution to this problem.

- Wave spectroscopy from passive inverse filter

Hereinafter, the passive inverse filter will be used to measure the dispersion curve from the spatial focalization. For each frequency component, waves will be focalized at a given position by means of the passive inverse filter. Then, from the spatial focalization an estimation of the wavelength will be obtained. Since the temporal frequency is known, the phase velocity can be easily calculated by multiplying the measured wavelength by the frequency.

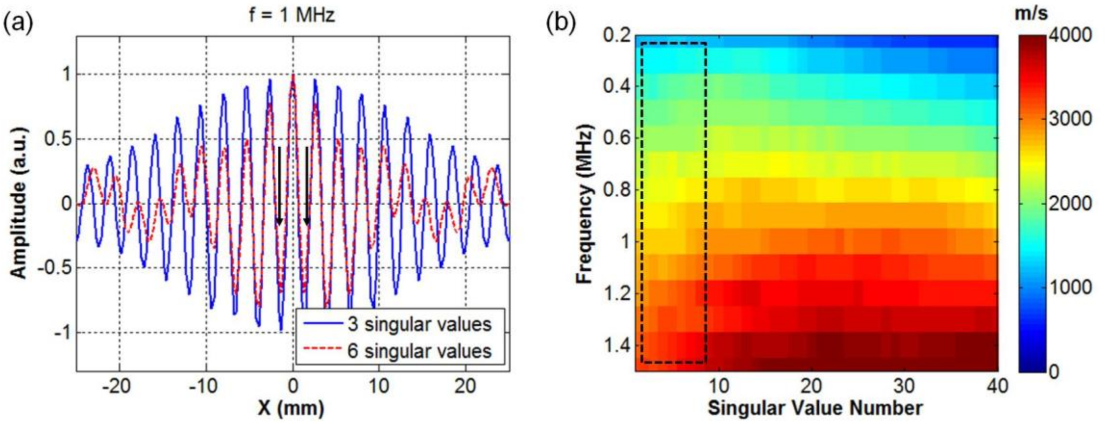

Fig. 5.3 (a) Spatial refocalization using passive inverse filter for a frequency of 1 MHz by using 3 singular values (blue full line) and 6 singular values (red dashed line). The black arrows indicate the minimums position. (b) Phase velocity distribution calculated from wavelength estimation obtained from the spatial focalization for the metallic bar. The black dashed rectangle indicates the zone used to retrieve the wave dispersion curve.

In Fig. 5.3(a) the focal spots computed through passive inverse filter, at a 1 MHz frequency, by using the first 3 singular values and the first 6 singular values are presented, in blue and red dashed line respectively. It can be observed, that the position of the first two minimums aside the focalization point (indicated with black arrows in Fig. 5.3(a)), remains practically constant when the number of single values is changed. The distance between this two minimums corresponds to the wavelength dominating the spatial focalization. Thus, an estimation of the phase velocity is obtained as $c_{\phi} = \lambda f$. Repeating this procedure for different frequencies and by varying the number of singular value used in the passive inverse filter computation the "phase velocity distribution" presented in Fig. 5.3(b) is obtained. For Fig. 5.3(b), the color scale represents the phase velocity calculated from the minimum's positions. Each line corresponds to a fixed frequency. On the other hand, each column corresponds to the number of singular values used in the passive inverse computation, e.g. four singular values mean that the first four singular values were used to compute the passive inverse filter through Eq. 4.16.

It was observed that, by taking until to eight singular values in the passive inverse computation, the retrieved phase velocity for a given frequency remains approximately constant (the zone is marked with a dashed black rectangle in Fig. 5.3(b)). Thus, by performing an average over the first eight columns on the phase velocity distribution, the dispersion curve, presented in Fig. 5.4 in black dots, is extracted. Each black dot corresponds to the mean value calculated from the phase velocity distribution for the first eight columns for a given frequency. The error bar corresponds to one standard deviation. In red the dispersion curve obtained from the direct wave propagation is presented.

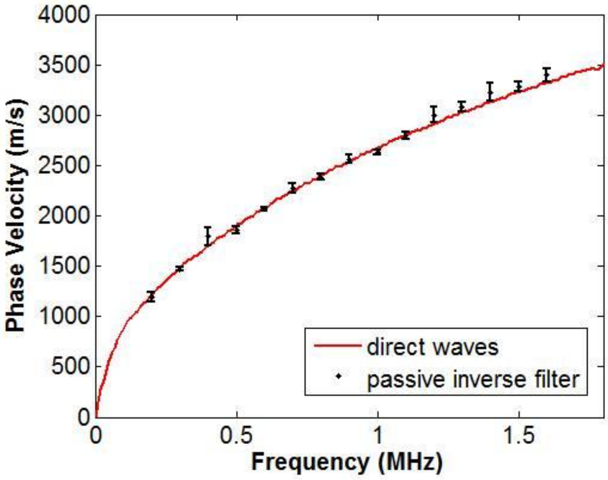

Fig. 5.4 Comparison between the dispersion curve obtained through the passive inverse filter (black dots) and the one obtained from the direct waves (red full line). Each black dot corresponds to the mean value calculated from phase velocity distribution (Fig. 5.3(b)) for the first eight singular values at a fixed frequency. The error bars correspond to one standard deviation.

From Fig. 5.4, a very good agreement is found between both dispersion curves. A mean relative error of 2% is found for each phase velocity estimation at a given frequency. This shows the potential of the passive inverse filter to perform a wave spectroscopy experiment in metals at ultrasonic frequencies. But in order to confirm such potential, an experiment in a stainless steel plate will be carried out below.

5.1.2 Experimental wave spectroscopy in a stainless steel plate

The experiment described in this section was carried out by Guillemette Ribay during her PhD thesis at the Laboratoire Ondes et Acoustique entitled "Source localization by time reversal in reverberant medium" [95]. The data set was kindly given to me by Dr. Catheline, for testing the the passive inverse filter to measure the dispersion curve in the case of metals.

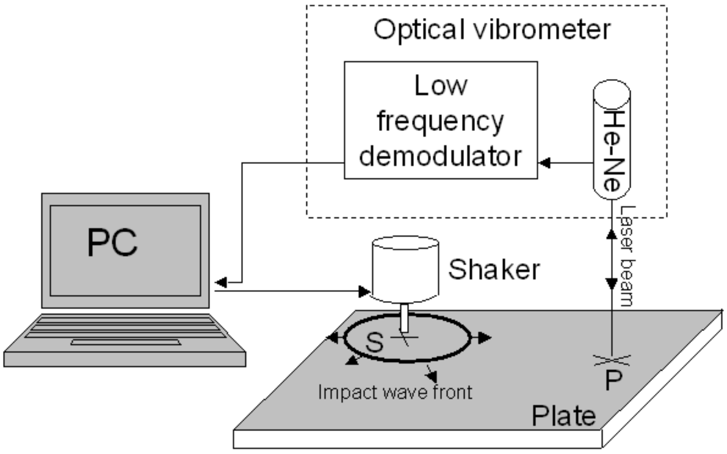

Fig. 5.5 Schematic representation of the experimental setup used for wave dispersion measurements in a stainless steel plate. **Source:** ***Ribay et al.*** **[96]**

In Fig. 5.5 a schematic representation of the experimental setup is presented: a 1 mm width steel plate of dimensions 30 x 40 cm is excited through a short knock, given by a metallic ball attached to mechanical vibrator applied perpendicular to the plate. The displacement field is measured in 200 control points forming a 65 mm radius circle at a 250 kHz sampling rate by an heterodyne interferometer equipped with a 100 mW frequency doubled Nd:YAG laser, coupled to a low frequency demodulator (0 - 2.5 MHz plane response). The measured displacement field, as well as its spectrum, are presented in Fig. 5.6 (a) and (b) respectively. From the displacement field, the presence of a reverberated field is clearly visible. As already demonstrated in [95] and [96], due to the type of source, the plate thickness and the frequencies involved in the experiment, the displacement field is dominated by the zero order anti-symmetric Lamb mode.

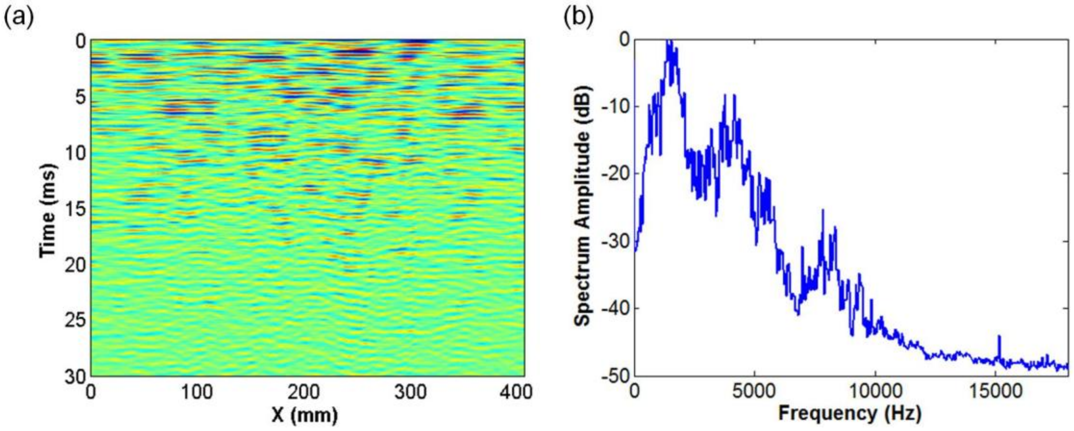

Fig. 5.6 (a) Measured displacement field in the steel plate experiment. (b) Spectrum of the acquired displacement field.

To measure the dispersion curve, the same procedure as in the case of the simulation will be followed. Firstly, the dispersion curve will be extracted by using correlation through the phase method. Secondly, the passive inverse filter will be applied for measuring the wave dispersion curve in the case of the focal width method.

- Experimental wave spectroscopy in a steel plate from phase correlation

Based on Fig. 5.6(b) the frequency content of the displacement field rises up to approximately 9000 Hz. Thus a whitening process from 1000 Hz to 8000 Hz will be used to compute the correlation field through phase correlation. The resulted correlation field is presented in Fig. 5.7(a). In this case, dispersion is not clearly visible in the spatial-temporal correlation field as in the case of the simulation study. As already explained in the preceding section, by computing the two dimensional Fourier transform of the correlation field, the wave dispersion curve is extracted. The obtained result is presented in Fig. 5.7(b) in black dots. For comparison, in Fig 5.7(b) in a red full line the theoretical zero order anti-symmetric Lamb mode for a steel plate in vacuum is presented. For calculating the Lamb theoretical dispersion curve, a shear wave speed value of 3260 m/s, a longitudinal shear wave speed value of 5960 m/s and a density of 7700 kg/m^3 were assumed for the steel plate. These values were extracted from [97].

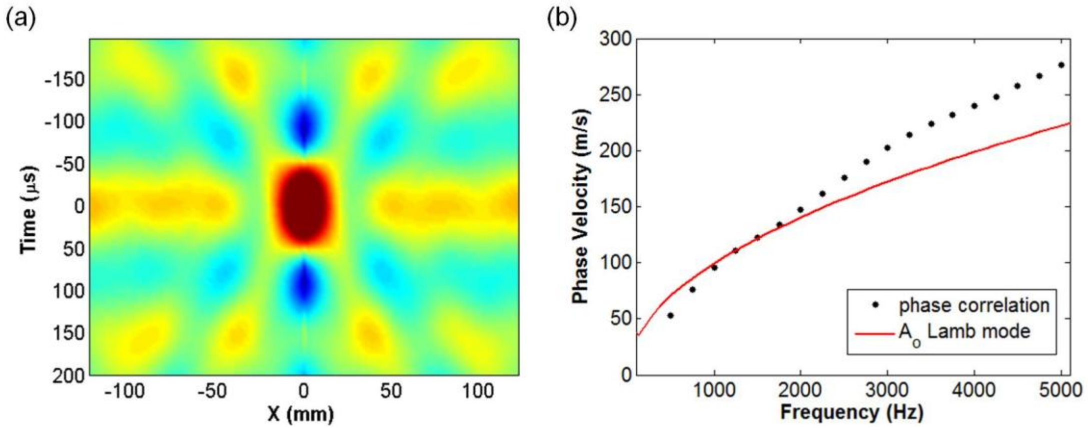

Fig. 5.7 (a) Experimental correlation field computed using phase correlation (1000 Hz - 80000 Hz) for the steel plate. (b) Comparison between the dispersion curve extracted from the correlation field (black dots) and the dispersion curve corresponding to the zero order anti-symmetric Lamb mode of a steel plate in vacuum. A shear wave speed, a longitudinal shear wave speed and a density of 3260 m/s, 5960 m/s, 7700 kg/m^3 were respectively assumed.

A not so good agreement is observed between the measured and the theoretical dispersion curve. This behavior could be anticipated, since as mentioned above, no dispersion is appreciable in Fig. 5.7(a). The cause of this misestimation can be attributed to the low signal to noise ratio outside the focal spot, since the phase method is known to be very sensitive to noise. Hereinafter, the focal width method, which is more robust to low signal to noise ratio, along with the passive inverse filter, will be used to extract the dispersion curve.

- Experimental wave spectroscopy in a steel plate from passive inverse filter

In this section the dispersion curve will be extracted by means of the passive inverse filter. The main difference between the present case and the finite difference simulation in a metallic bar lies in the wave propagation model that should be considered for the inverse problem. While in the case of the simulations it was sufficient to consider it as one dimensional, for the present case the wave propagation should be considered as two dimensional. For the case of a two dimensional scalar wave field the spatial focalization is given by the function $sinc(kr)$ [98], where k is the wavenumber and r the position respect to the focal point. As for a two dimensional elastic field, the spatial focalization is described by the zero order Bessel function of the first kind: $J_o(kr)$ [95]. By assuming this model, it will be possible to measure k from the spatial focalization as it will be described below.

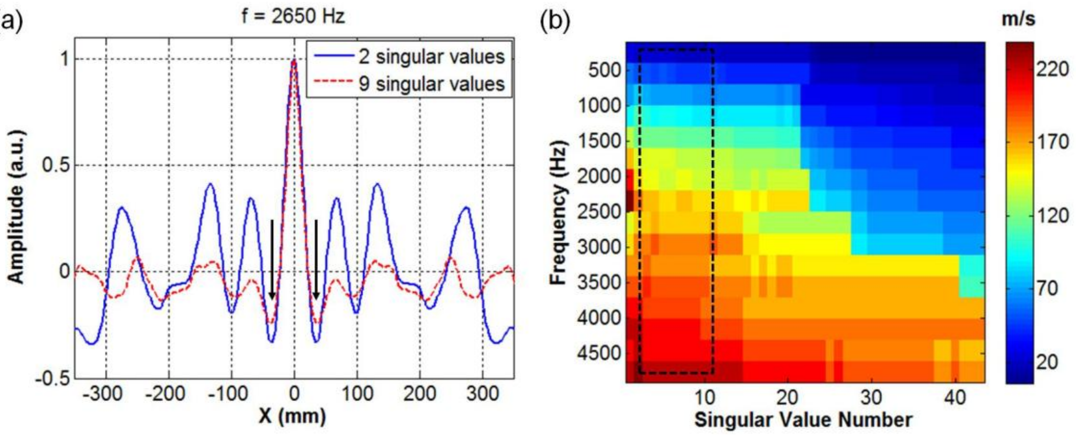

Fig. 5.8 (a) Spatial refocalization using passive inverse filter for two (blue full line) and nine (red dashed line) singular values for a 2650 Hz frequency. The first two minimums are indicated by black arrows, remaining constant with the singular value number. (b) Phase velocity distribution calculated from the spatial focalization minimums position by assuming a $J_o(kr)$ focalization model.

In Fig. 5.8(a), for a frequency of 2650 Hz, the spatial focalization computed through the passive inverse filter, by using two (blue full line) and nine (red dashed line) singular values is presented. The window length for the passive inverse filter computation was set to 0.8 ms. As it was already observed in the finite difference simulation, in Fig. 5.8(a) the position of the first minimums asides the maximum (which are indicated by black arrows) remains approximately constant as a function of the singular value number used in the passive inverse computation. Thus, by assuming that the spatial focalization is described by a zero order Bessel function of the first kind, the minimum's positions are given by the zero's position of the first order Bessel function of the first kind $J_1(kr)$, since $J_1(kr)$ is proportional to the derivative of $J_o(kr)$. Thus, the following relation between k and the minimum's position r_{min} can be established:

$$k.r_{min} = 3.83 \tag{5.1}$$

Where 3.83 correspond to the first zero's position of $J_1(x)$. By measuring the minimum's position and solving for k and estimation of the phase velocity is obtained. For the final wavenumber estimation, an average over the first two minimums is used. The obtained phase velocity distribution is presented in Fig. 5.8(b).

From the phase velocity distribution, it can be observed that for a fixed frequency the phase velocity remains approximately constant until a given column m_o, which corresponds to the maximum number of singular values that should be taken into account in the passive inverse computation. For example, for 3000 Hz, m_o is approximately 13. After this value is reached, a strong decrease in the velocity value is observed. The maximum singular value number m_o depends on the frequency, as it was already discussed in Chapter IV. Best results were obtained by performing an average over the first ten columns on the phase velocity distribution (marked with a dashed line in Fig. 5.8(b)). The extracted dispersion curve is presented in Fig 5.9 in black dots along with the anti-symmetric Lamb mode in red full line. The error bars correspond to one standard deviation.

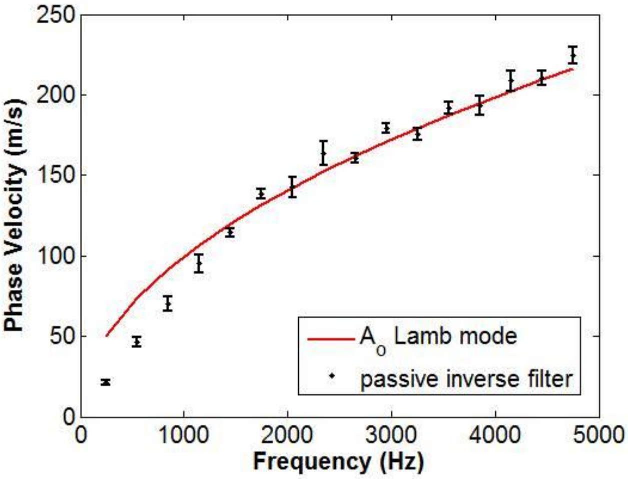

Fig. 5.9 Experimental dispersion curve for a steel plate using the passive inverse filter (black dots). The theoretical dispersion curve corresponding to the zero order anti-symmetric Lamb mode for a steel plate in vacuum is presented in red full line.

A good general agreement is observed between the measured and the theoretical dispersion curve. However, an underestimation of the phase velocity is observed for lower frequencies. A similar behavior was already described in [95] for a duralumin bar. For the lower frequencies the measured wavelength correspond to approximately 9 cm, thus the effect of edges, due to the finite size of the plate (30 x 40 cm), is not negligible. In [96] it was reported that the focal spot shape varies from a circular shape into an oval shape near the edges. This could a possible explanation to the underestimation at lower frequencies, although further studies need to be carried out to further clarify this point.

5.2: Shear wave spectroscopy from reverberated elastic field in soft solids: application to elastography

In the previous section, the ability of the passive inverse filter for conducting a wave spectroscopy experiment was demonstrated in metals. In this section, the concepts previously developed for metals, will be applied to measure the shear wave dispersion in the case of the elastography experiments presented throughout this manuscript. Two situations will be considered: guided wave propagation in a soft solid thin layer and dispersion due to viscosity effects.

5.2.1 Wave dispersion due to guided wave propagation in a soft solid thin layer

By using phase correlation and the passive inverse filter, the feasibility for conducting a wave spectroscopy experiment from a complex reverberated wave field will be studied in the case of a soft solid thin layer. As it was done in section 5.1 for metals, in a first step, a finite difference simulation is conducted to test the potential of these techniques in the case of the elastography experiments. Secondly, an experiment will be carried out in a thin layer embedded in a larger medium.

- Finite difference feasibility study

The simulated experiment was carried out using ACEL software [58]. A schematic representation of the simulation grid is presented in Fig. 5.10. The propagating medium was set to be a thin layer with a 2 mm width and 5 m/s shear wave speed value embedded in a larger medium with a shear wave speed of 1 m/s, very similar to the samples evaluated in Chapter II. The longitudinal wave speed and density were set constant throughout the sample with values 1500 m/s and 1000 kg/m^3 respectively. Triangular, rectangular and round sections were cut off in order to avoid symmetry effects. The sources (marked as stars in Fig. 5.10), were randomly distributed and activated on the simulation grid surface, as its the case of the noise experiments presented in Chapters III and IV. Each source was excited with two sinusoid cycles ranging randomly from 20 Hz to 450 Hz central frequency. The vertical component (z-component) of the displacement field was acquired at 1000 Hz sampling rate during 1 second. The simulation spatial grid consisted in 120 points separated by a 0.4 mm spatial pitch. The 120 control points were placed on a line parallel to the x-axis at 18 mm depth (inside the layer), each one spaced by the simulation spatial pitch.

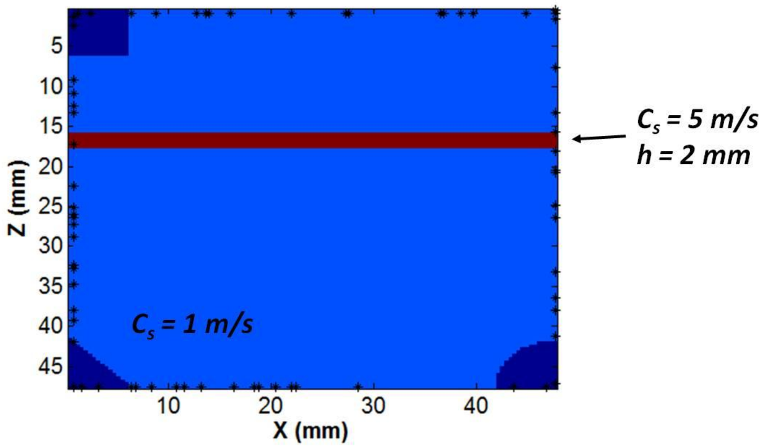

Fig. 5.10 Schematic representation of the simulation grid. The propagating medium was set to be a thin layer with a 2 mm width and 5 m/s shear wave speed value embedded in a larger medium with a shear wave speed of 1 m/s. The longitudinal wave speed of 1500 m/s and density of 1000 kg/m3 were set constant throughout the sample.

By following an analogous procedure to the preceding section, first the wave dispersion curve will be retrieved by using phase correlation. Second, the passive inverse filter will be applied to extract the shear wave dispersion curve. For the final correlation map/spatial focalization a spatial average over the different control points was performed.

In Fig. 5.11(a) the spatial-temporal correlation field computed using phase correlation with a whitening process from 20 Hz to 450 Hz is presented. Dispersion is clearly visible in the spatial-temporal correlation field, as in the case of the finite difference simulation carried out in the metallic bar (Fig. 5.2). By computing the two dimensional Fourier transform from the correlation field, the wave dispersion curve is extracted. The obtained result is presented in Fig. 5.11(b) in black dots.

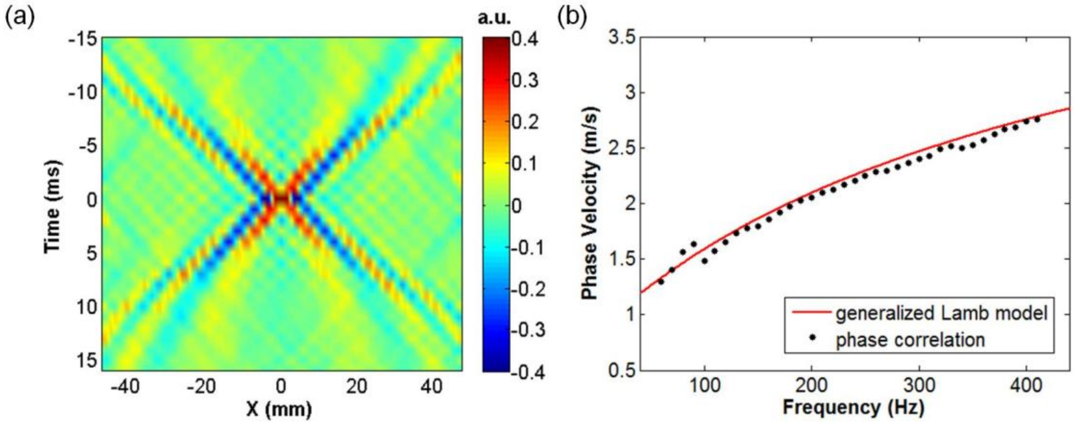

Fig. 5.11 (a) Correlation field computed using phase correlation (20 Hz - 450 Hz) for the thin layer. (b) Comparison between the dispersion curve extracted from the correlation field (black dots) and the dispersion curve calculated from the generalized Lamb model presented in Chapter II (red full line).

As it was already discussed in Chapter II for this kind of wave propagation due to the low frequency content of the elastic field as well as to the bulk wave speeds and thickness values involved, the guided wave will propagate mainly as a zero order Lamb mode [55]. Since the vertical component (z-component) of the displacement field was acquired, the wave field will be therefore dominated by the zero order anti-symmetric Lamb mode. Using the generalized Lamb model presented in Chapter II, the theoretical dispersion curve was numerically computed for the configuration presented in Fig. 5.10. The obtained result is presented in a full red line in Fig. 5.11(b). A very good agreement is found between the extracted dispersion curve from phase correlation and the generalized Lamb model. A small underestimation for the phase velocity calculated from phase correlation compared to the generalized Lamb model is observed. This could be attributed to small differences between the finite difference simulation and the numerical resolution of the generalized Lamb model. Now that the potential of phase correlation for measuring the dispersion curve was demonstrated through simulation, the passive inverse filter will be tested.

For the passive inverse filter, although the simulation was carried out in two dimensions the wave propagation inside the layer can be considered as one dimensional. Thus, hereinafter, the same procedure described in section 5.1.1, for extracting the Lamb wave dispersion curve using the passive inverse filter for the case of a metallic bar, will be utilized. First, the phase velocity distribution is computed from the minimum's position of the spatial focalization as a function of the number of singular values and frequency. The obtained result is presented in Fig. 5.12(a).

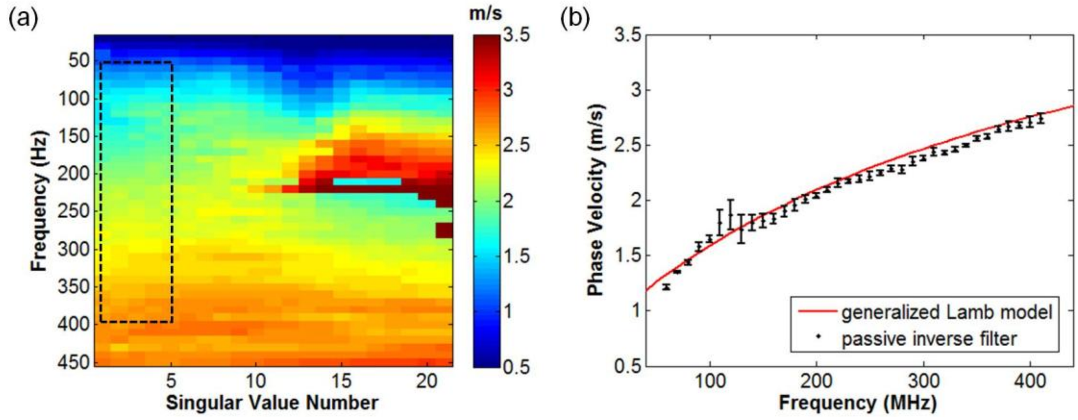

Fig. 5.12 (a) Phase velocity distribution calculated from the minimum's position of spatial focalization in the case of the thin layer. (b) Comparison between the dispersion curve obtained through passive inverse filter (black dots) and the one obtained from the generalized Lamb model (red full line). Each black dot corresponds to the mean value calculated from (a) for the first 5 singular values at a fixed frequency. The error bars correspond to one standard deviation.

To extract the wave dispersion curve from the phase velocity distribution, an average over the first five columns of the phase velocity distribution is performed. The obtained dispersion curve is presented in Fig. 5.12(b) in black dots. The error bars correspond to one standard deviation. The theoretical dispersion curve obtained from the generalized Lamb model is also presented in Fig. 5.12(b), in a red full line. A good agreement between both dispersion curves is observed. A mean relative error of 2% is found for each phase velocity estimation at a given frequency. Again, a mean underestimation within 3.3 % on the phase velocity is observed when compared to the model. The obtained results through passive inverse filter agree with the ones obtained through phase correlation.

From the results presented in this section, the passive inverse filter could be used for measuring the wave dispersion curve in a soft solid thin layer. Below, the feasibility of the passive inverse filter for measuring dispersion in a soft solid thin layer will be tested experimentally.

- Experimental wave spectroscopy in a soft solid thin layer

The phantom used for the experiments consists of an elastic plate of 6.0 ± 0.1 mm thickness surrounded by a PVA-C gel [57]. The layer, also made of PVA-C, underwent four freeze-thaw cycles while the surrounding gel only underwent one. The layer, as well as the surrounding gel, were previously characterized by 1D transient elastography. A shear wave speed of 3.25 ± 0.2 m/s and 1.8 ± 0.1 m/s were respectively measured for the layer and the surrounding gel. The complex reverberated field inside the layer was created by finger impacts given randomly all over the phantom accessible surface. One component (along z direction) of the complex elastic field is measured on a control line placed inside and parallel to the plate at 1000 Hz frequency rate by a standard speckle tracking technique using a 64 elements, 6 MHz central frequency ultrasonic linear array and an ultrafast scanner (Lecoeur Electronique, France). A schematic representation of the experimental setup is presented in Fig. 5.13.

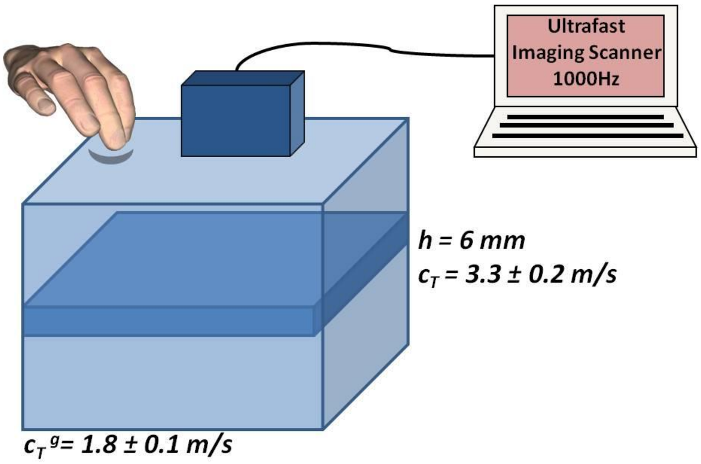

Fig. 5.13 Experimental setup used for measuring the dispersion curve in a soft solid thin layer. The phantom used for the experiments consists of an elastic plate of 6.0 ± 0.1 mm thickness and 3.3 ± 0.2 m/s shear wave speed surrounded by a PVA-C gel of 1.8 ± 0.1 m/s shear wave speed. The displacement field created inside de the layer by finger impacts given randomly all over the phantom accessible surface is imaged with an ultrafast scanner.

Due to the noise present in the acquired displacement field, phase correlation could not be used for extracting the wave dispersion curve. Thus, the focal width method through the passive inverse filter will be used, since as explained previously, it is more robust to low signal to noise ratio.

For extracting the wave dispersion curve through the passive inverse filter the same procedure presented in section 5.1.2, for the case of a metallic plate, will be followed. Firstly, the phase velocity distribution is computed by estimating the wave number k from the minimum's position of the spatial focalization through Eq. 5.1. The measured phase velocity distribution is presented in Fig. 5.14(a). As it was already observed in section 5.1.2, in the case of a metallic plate, the phase velocity distribution for a fixed frequency remains approximately constant until a given column m_o, from which it decreases abruptly, this columns corresponding to the maximum number of singular values that should be taken into account in the passive inverse filter computation. In this case, from Fig. 5.14(a), the value of m_o is between two and three, being three for the higher frequencies. The wave phase velocity for each frequency is extracted by performing an average over the first three columns of the phase velocity distribution. The zone used for performing the average is indicated in Fig. 5.14(a) by a dashed black rectangle. The extracted dispersion curve is presented in Fig. 5.14(b), where the error bars correspond to one standard deviation.

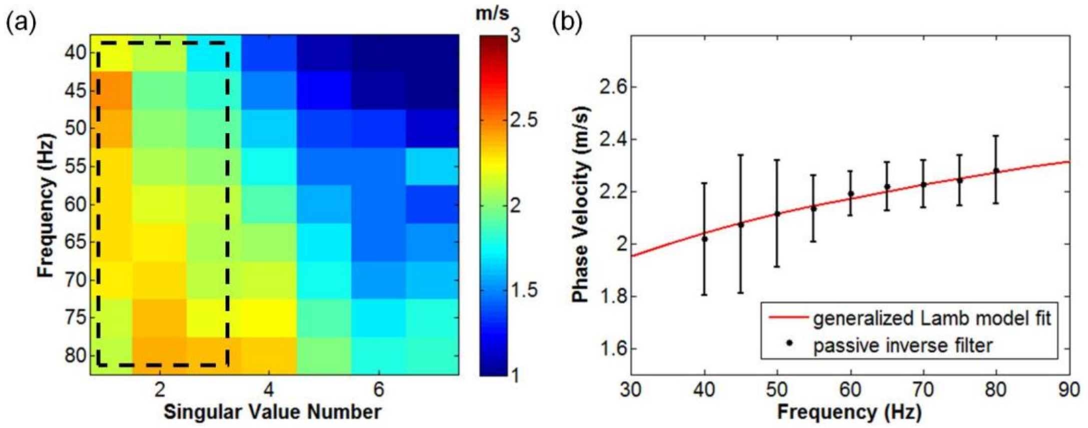

Fig. 5.14 (a) Experimental phase velocity distribution for the soft solid thin layer. The dashed black rectangle indicates the zone utilized for extracting the wave dispersion curve. (b) Dispersion curve obtained through passive inverse filter (black dots). Each black dot corresponds to the mean value calculated from (a) for the first 3 singular values at a fixed frequency. The error bars correspond to one standard deviation. In red full line the fit through the generalized Lamb model is presented.

From Fig. 5.14 (b), a mean relative error of 7%, with a mean relative deviation from the theoretical model of 3% is obtained for each individual phase velocity estimation. By fitting the generalized Lamb model presented in Chapter II section 2.2.4 to the experimental data, a plate shear wave velocity of 3.1 ± 0.4 m/s was obtained. The error was estimated by taking into account the error on each individual measurement. The theoretical fit is presented in a red full line in Fig. 5.14(b). The retrieved plate shear wave speed coincides, within the error margins, with the 1D transient elastography estimation, demonstrating the potential of the passive inverse filter for measuring the wave dispersion curves due to guided wave propagation in a soft solids thin layers.

However, guided wave propagation is not the only cause for dispersion in the case of soft solid. In the following section, the ability of the passive inverse filter for measuring dispersion caused by viscosity will be tested *in vitro* and *in vivo* in the abdominal muscle and liver.

5.2.2 Measuring shear wave dispersion due to viscosity

The assessment of dispersion affecting the propagation of viscoelastic waves in soft tissues is key to understand the rheology of human tissues. In Chapter I several dynamic methods for retrieving the shear elasticity based on shear wave propagation were presented. One of the main advantages of dynamic methods is the potential for revealing the medium dynamic properties, such as viscosity. For example in the case of a plane monochromatic shear wave, the measured phase velocity and attenuation can be converted into elasticity and viscosity by assuming an appropriate rheological model. The simplest viscoelastic models utilizing two parameters are the

Voigt and Maxwell model, represented in Fig. 5.15 (a) and (b) respectively. The Voigt's model is composed of a spring, with spring constant μ_1 , and a dashpot, with viscosity coefficient μ_2, in parallel, while the Maxwell model is composed of a spring and a dashpot in series. In the case of the Voigt model the relationship between phase velocity and attenuation of a plane shear wave and the mechanical properties of the medium is given by

$$c_\phi(f) = \sqrt{\frac{2\left(\mu_1^2+4\pi^2 f \mu_2^2\right)}{\rho\left(\mu_1+\sqrt{\mu_1^2+4\pi^2 f^2 \mu_2^2}\right)}} \tag{5.2a}$$

$$\alpha(f) = \sqrt{\frac{4\pi^2 f^2 . \rho\left(\sqrt{\mu_1^2+4\pi^2 f^2 \mu_2^2} - \mu_1\right)}{2\left(\mu_1^2+4\pi^2 f^2 \mu_2^2\right)}} \tag{5.2b}$$

where ρ is the medium's mass density, $c_\phi(f)$ the phase velocity and $\alpha(f)$ the wave attenuation.

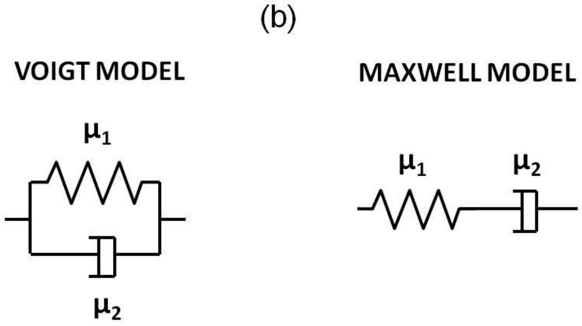

Fig. 5.15 Schematic illustration of (a) the Voigt model and (b) the Maxwell model.

In the work of *Catheline et al.* [94] a plate attached to a mechanical vibrator was used to generate plane shear waves in the monochromatic regime, in order to obtain the dispersion curves of gelatin phantoms and *ex vivo* muscle in the 50 Hz to 1 kHz frequency range. Measuring both, shear wave speed and attenuation, it was demonstrated that gelatin phantoms can be described using a Voigt model in the aforementioned frequency range. However, the use of the Voigt model for *ex vivo* muscle was more controversial. In 2004, *Chen et al.* [35] proposed to use the ultrasonic radiation of a focused ultrasound transducer in order to generate a shear wave in gelatin phantoms. The displacement field induced by the shear wave propagation was tracked using a laser vibrometer and a micro-mirror embedded in the phantom. By fitting the Voigt model to the shear wave speed dispersion curve, in a least square sense, a global shear modulus and viscosity estimation were retrieved. Although very interesting, the preceding approaches, due to the experimental setups involved, were limited to an *in vitro* estimation and unfortunately difficult to apply *in vivo*. To overcome this limitation, *Deffieux et al.* [61] proposed the use of the SSI technique to conduct a shear wave spectroscopy experiment *in vivo* in the biceps brachii, abdominal muscle and liver of three healthy volunteers, showing important differences in the rheological behavior for these different tissues. In 2007, *Sabra et al.* [9] measured the shear wave dispersion curve through cross correlation *in vivo* in skeletal muscle by using the noise naturally present in such tissue. For the experiment sixteen miniature accelerometers were skin mounted along the *vastus lateralis* muscle providing a surface measurement.

In this section, the passive inverse filter will be used for measuring the dispersion curve in the volume of a tissue, from a complex reverberated field. For this purpose, two types of experiments were performed: an *in vitro* experiment in PVA-C phantoms and an *in vivo* experiment in the liver/abdominal muscle of one healthy volunteer.

- In vitro shear wave spectroscopy experiment

The *in vitro* experiment is carried out by tapping with the fingers on the bi-layer phantom's surface as described in section 3.3. Contrary to section 3.3, in this section, an estimation of the shear wavenumber k is obtained by measuring the curvature of the spatial focalization (as introduced in section 4.3.4). Thus, the shear wave phase velocity can be calculated as:

$$c_{\phi}(f) = \omega \backslash k = 2\pi f \sqrt{-\frac{1}{5.S_x}} \tag{5.3a}$$

$$c_{\phi}(f) = \omega \backslash k = 2\pi f \sqrt{-\frac{1}{10.S_z}} \tag{5.3b}$$

Where S_x and S_z are the curvatures of the spatial focalization along the x-axis and z-axis respectively. The noise introduced due to the inverse of the curvature in Eq. 5.3, is reduced by performing a spatial average over different focal points. The averaged spatial focalization for the hard and soft layer are presented in Fig. 5.16 (a) and (b) respectively. As consequence of the spatial averaging, a global shear wave dispersion curve is obtained.

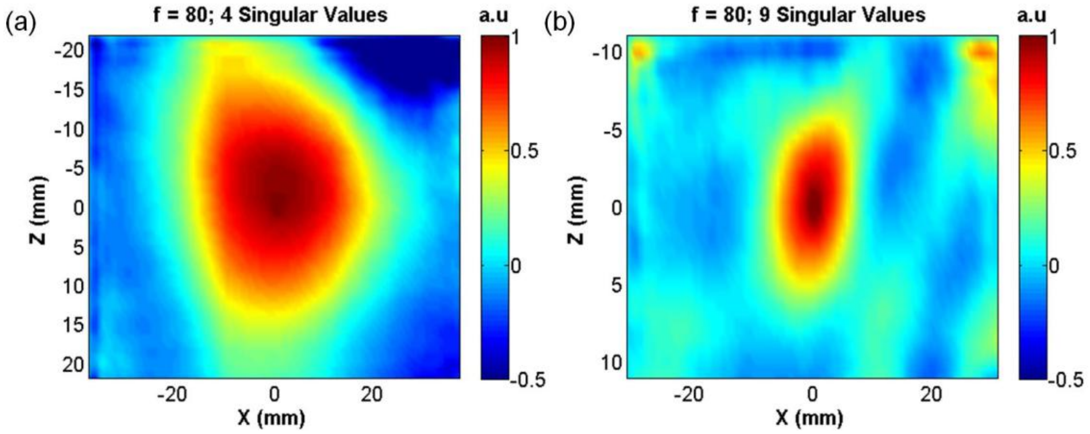

Fig. 5.16 Averaged spatial focalization through passive inverse filter for the (a) hard and (b) soft layer for a 80 Hz frequency. For the passive inverse filter computation four and nine singular values were used respectively.

Best results were found when calculating the shear wave phase velocity from Eq. 5.3b. For the parabolic fit, eight and fourteen points around the focal point (set as zero) were used for the soft and hard layer respectively. The final shear wave dispersion curves are presented in Fig. 5.17. In Fig. 5.17(a) the boxes on each layer indicate the zone used for the spatial averaging. For the shear wave dispersion curves, in Fig. 5.17(b), an average over the different number of eigenvalues used for computing the passive inverse filter was performed. The error bar corresponds to one standard deviation. While for the soft layer from four to ten singular values were used for the average, in the hard layer only three and four singular values were used. The difference on the number of useful singular values, is due to the number of independent focal spots is much smaller in the hard than in the soft medium, as it was already discussed in Chapter IV.

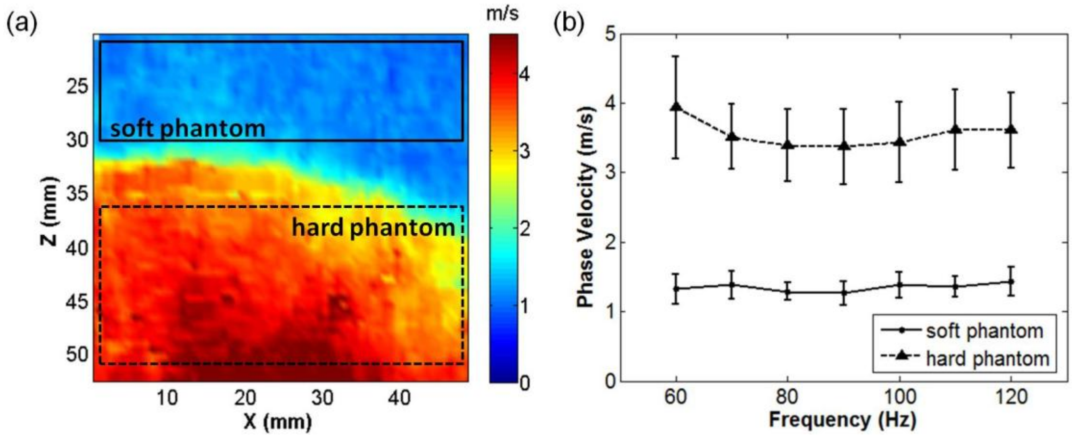

Fig. 5.17 (a) Shear wave speed map for the bi-layer phantom obtained through passive inverse filter. The boxes indicate the zones used for computing the average spatial focalization. (b) Shear wave speed dispersion curves obtained for each layer. An average over different singular values was used for the final result. The error bar corresponds to one standard deviation.

From 5.17(b) no dispersion is observed neither for the soft layer nor for the hard layer. This is consistent with the behavior of PVA-C based phantoms as was already observed in section 2.5.1. A mean shear wave speed of 3.6 ± 0.6 m/s and 1.3 ± 0.2 m/s were found for the hard and soft layer respectively. A mean relative error of 14% is obtained for each single shear wave speed estimation at a given frequency. This is consistent with the relative error estimation given in section 4.3.1 due to a miss estimation on N.

- In vivo passive shear wave spectroscopy from physiological noise

In this section a passive shear wave spectroscopy experiment using the physiological noise present in the human body is carried out by following the same procedure explained in the previous section. The averaged spatial focalization for the muscle and liver are presented in Fig. 5.18 (a) and (b) respectively. Thanks to the spatial averaging, the focus on the muscle is better resolved when compared to the local spatial focalization presented in Fig. 4.17(a). In the case of the liver some noise appears on the spatial focalization (right down corner of Fig. 5.18(b)) however it does not affect the shear wave speed retrieval through the curvature measurement.

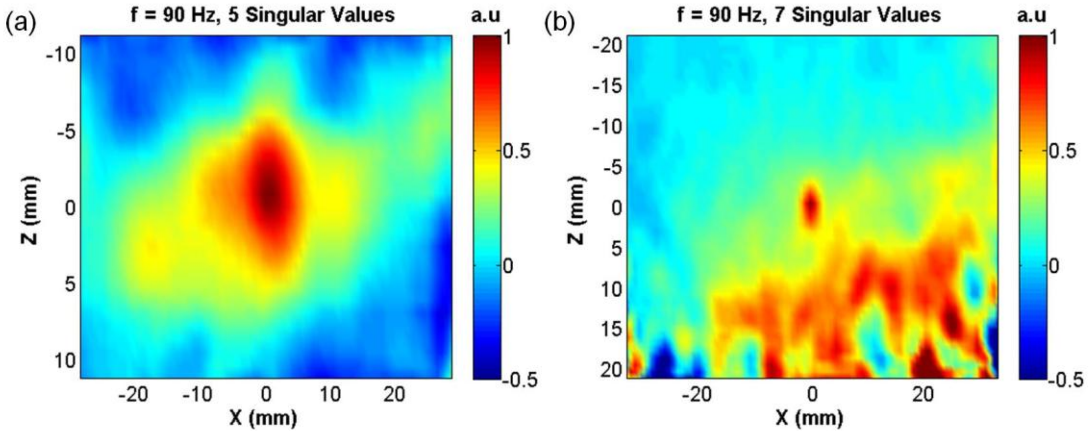

Fig. 5.18 Averaged spatial focalization through passive inverse filter for the (a) muscle and (b) liver for a 90 Hz frequency. For the passive inverse filter computation five and seven singular values were used respectively.

For this case, best results were found when calculating the shear wave phase velocity from the curvature along the x - axis (Eq. 5.3a). For the parabolic fit eight points around the focal point were used. The final shear wave dispersion curves are presented in Fig. 5.19. In Fig. 5.19(a) the boxes on each tissue indicate the zone used for the spatial averaging. For the shear wave dispersion curves in Fig. 5.19(b) an average over the different number of eigenvalues used for computing the passive inverse filter was performed. The error bar corresponds to one standard deviation. For the final result, an average from four to six and from three to five singular values was performed in the liver and muscle respectively.

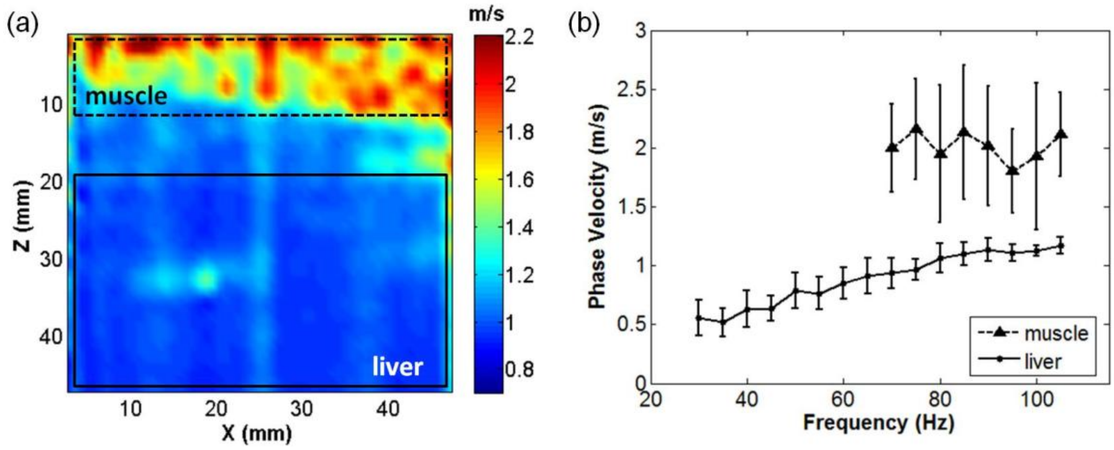

Fig. 5.19 (a) Shear wave speed map for the passive elastography experiment in the liver obtained through passive inverse filter. The boxes indicate the zones used for computing the average spatial focalization. (b) Shear wave speed dispersion curves obtained for each tissue. An average over different singular values was used for the final result. The error bar corresponds to one standard deviation.

The first thing to note in Fig. 5.19(b) is that the frequency band for the dispersion curves in the muscle and in the liver is not the same. This difference can be explained based on the fact that muscle is harder than liver and as a consequence the focal spots in the muscle are larger than in the liver. Since the surface occupied by the muscle in the imaging plane is small, only small wavelength could be measured properly which is equivalent to high frequencies, which was not the case for the liver.

For the belly muscle no dispersive effects are observed in agreement with the reported behavior in [61]. A mean shear wave speed value of 2.0 ± 0.5 m/s is obtained in good agreement with the reported results in the literature as discussed in sections 3.3.4 and 4.3.4.

Contrary to the muscle, an increase in the shear wave speed value as a function of frequency is observed for the liver. This is consistent with the behavior observed in [61] and [38]. The slope of the phase velocity dispersion curve, however, was found to be 6.9 ± 2.4 mm, which is approximately two times bigger than the value found in [38] for the SSI technique. The difference between both slopes can be attributed to the different frequency bandwidths used in the SSI technique and the passive inverse filter experiment. While the SSI technique works in a frequency bandwidth ranging from 70 to 400 Hz, the passive inverse filter only works between 30 and 105 Hz. Thus small fluctuation have a stronger influence in the passive shear wave spectroscopy than in the SSI technique. A shear wave speed of 0.8 ± 0.1 m/s was found for the liver at 50 Hz again in good agreement with the reported results in the literature as was already discussed in previous Chapters.

5.3: Conclusions

In this Chapter the frequency control in the spatial focalization through the passive inverse was exploited for measuring the wave dispersion. Two different scenarios were considered. Firstly, the ability of the passive inverse filter to conduct a wave spectroscopy experiment from a complex reverberated field was demonstrated experimentally in metals. Secondly, the passive inverse filter was applied to measure dispersion in two different elastography experiments: guided wave propagation in a soft solid thin layer and dispersion due to viscosity effects.

In metals, the passive inverse filter showed to be more robust than phase correlation for low signal to noise ratio. This fact was also verified when measuring the wave dispersion curve in a soft solid thin layer. For both cases, the low signal to noise ratio was prohibitive for phase correlation. Contrary, when using the passive inverse filter the dispersion curve was successfully measured. The experimental dispersion curves showed to be in good agreement when compared to the theoretical dispersion curves computed from the generalized Lamb model. For the soft solid thin layer, by fitting the generalized Lamb model to the experimental dispersion curve, the plate shear wave speed was retrieved in good agreement with a previous estimation through 1D transient elastography.

Nevertheless, in soft tissues guided wave propagation is not the only cause of dispersion, viscosity effects lead to shear wave dispersion too. To finish demonstrating the potential of the passive inverse filter for measuring dispersion an *in vivo* passive shear wave spectroscopy experiment was carried out on the liver/abdominal muscle of one healthy volunteer. No dispersive effects where observed in the abdominal muscle, contrary, in the liver, an increase in the phase velocity with frequency was observed. In both cases the observed behavior coincides with the reported results in the literature, demonstrating in this way the potential of the passive inverse filter for evaluating the rheological properties of biological tissue *in vivo.*

General conclusions and perspectives

In this thesis a study of different elastography techniques from a basic point of view, as well as from its potential applications, was proposed. The main contributions of this work to the field of elastography can be sub divided in two different categories: active and passive elastography.

Regarding active elastography techniques, in this thesis, the use of 1D transient elastography for the assessment of the elasticity of sub-wavelength layered soft tissues was proposed and validated in Chapter II. The good agreement between the 1D transient elastography shear wave speed estimations and the material shear wave speed as well as simulations validated the use of this technique. The main advantage of 1D transient elastography stands in its simplicity of application as the true shear wave speed is directly retrieved from a time of flight algorithm without the need of a model. Interestingly, the diffraction pattern of the shear wave in the near field of the piston is particularly well suited to such plate stiffness estimation as the wave polarization is parallel to its propagation direction and perpendicular to the plate. This well adapted geometry optimizes the wave propagation pattern that is not affected by guidance effects. The obtained results were also compared with the ones obtained by the SSI technique. The SSI technique uses a completely different propagation mode for which the inverse problem requires a much more complex acquisition sequence and post-processing analysis: dispersion effects have to be measured and used for the recovery of the plate stiffness by using a generalized Lamb model. Finally, through both techniques the same shear wave speed estimation is obtained. The obtained results allow thinking in applying 1D transient elastography for the *in vivo* elasticity assessment of thin tissue, like the arterial wall.

Regarding passive elastography techniques, in this thesis, two novel imaging modalities for extracting the soft tissue's elasticity from a complex reverberated elastic field generated by a set of uncontrolled sources were deepen: Time Reversal Elastography (TRE) and the Passive Inverse Filter. The goal of both techniques is to locally estimate the tissue's elasticity, by measuring the spatial focal spot size in a virtual time reversal experiment involving shear waves.

In Chapter III the feasibility of TRE as a quantitative elasticity imaging technique was demonstrated in the cases of a bi layer mediums (e.g. phantom and muscle-liver). For this purpose, in a first step, an analytical expression for the spatial focalization at a single frequency was derived, in the general case of an elastic wave field. The validity of the derived expression was tested experimentally in the volume of an homogeneous phantom. The virtual time reversed field in TRE is computed by using either normalized or phase correlation. As a consequence the spatial focalization is composed of multiple temporal frequencies.

The main drawback of normalized correlation is the lack of knowledge on the frequency components contributing to the spatial focalization. In order to solve this problem, an empirical formula, based on the derived analytical expression for the spatial focalization, at a single effective frequency was proposed. This empirical formula was interpreted as the spatial focalization being dominated by one effective frequency which equals the mean root square frequency calculated by using as a weighting function the power spectrum. Based on this empirical formula, quantitative shear wave speed maps were retrieved using normalized correlation in good agreement with the B-mode images and prior elasticity estimations. The main advantage of normalized correlation is its compatibility with "ultraslow" imaging devices, such as standard two-dimensional and three-dimensional ultrasound and magnetic resonance devices, placing this approach as a promising imaging technique.

In order to assure the same weight, for all the frequency components contributing to the time reversed field, phase correlation was introduced. An analytical formula which relates the mean radius or surface of the focal spot at a given isolevel curve, the frequency bandwidth used for phase correlation computation and the tissue elasticity was developed. By using the analytical formula quantitative shear wave speed maps were obtained in good agreement with the B-mode images, prior elasticity estimations and the images obtained through normalized correlation.

Finally, to show the potential of TRE as a passive imaging technique, a feasibility *in vivo* study in the human liver was carried out. For the first time, a passive quantitative elasticity image was obtained, in good agreement with reported results. It is important to notice that while other elastography techniques suffer from the physiological noise in the human body, TRE takes advantage of this permanent elastic field. However, when using the physiological noise the spatial-temporal frequency content of the elastic field is not controlled. This could set a limitation to the applicability of TRE when trying to measure the elasticity of small organs or tissue. On the other hand, passive elastography might be an alternative for elasticity imaging in deep organs or barely accessible regions where high-power ultrasound needed for radiation force is difficult to use.

The main drawback of the TRE technique arises when trying to image small inclusion embedded in a larger medium. The cause of this problem lies in the directivity of the computed time reversed field. Since the source distribution in the noise experiments is not homogeneously distributed, the resulting time reversed has privileged propagation direction, leading to deformed focal spots due to diffraction effects. In this manuscript a solution to this problem was proposed by adapting the technique known as inverse filter to particular case of a passive source configuration, resulting in the technique termed as passive inverse filter. The passive inverse filter uses in an optimal way the information conveyed by the wavefield. As a result, the directivity of the time reversed field is corrected and inclusions could be satisfactory resolved.

Nevertheless, the directivity correction of the time reversed field is not the only advantage of the passive inverse filter. The optimal use of information achieved through the passive inverse filter, allows a spatial focalization which is composed of a single temporal frequency. This advantage was exploited to perform a passive wave spectroscopy experiment. Firstly, the ability of the passive inverse filter for measuring wave dispersion was demonstrated experimentally in metals. Secondly, the passive inverse filter was used to measure the shear wave dispersion in the case of the elastography experiments presented throughout this manuscript. Two situations were considered: guided wave propagation in a soft solid thin layer and dispersion due to viscosity effects. In both situations, through the passive inverse filter, dispersive effects were measured in good agreement with the theoretical models and the reported results in the literature. This allows thinking in several applications of the passive inverse filter, like passive elasticity assessment of thin layered soft tissue or *in vivo* passive visco-elastic imaging.

References

[1] M. Fink, “Time-reversal of ultrasonic fields part I: Basic principles,” *IEEE Trans. Ultrason. Ferroelectr. Freq. Control*, vol. 39, no. 5, pp. 555–566, 1992.

[2] S. Catheline, N. Benech, J. Brum, and C. Negreira, “Time-reversal of elastic waves in soft solids,” *Phys. Rev. Lett.*, vol. 100, art. no. 064301, 2008.

[3] N. Benech, S. Catheline, J. Brum, T. Gallot, C. Negreira, “1D elasticity assessment in soft solids from shear wave correlation: The time-reversal approach,” *IEEE Trans. Ultras. Ferroelec. Freq. Control*, vol. 56, pp. 2400-2410, 2009.

[4] J. Brum, S. Catheline, N. Benech, C. Negreira, “Shear elasticity estimation from surface waves: the time-reversal approach”, *J. Acoust. Soc. Am.*, vol. 124, no. 6, pp. 3377-3380, 2008.

[5] A. P. Sarvazyan, O. V. Rudenko, S. D. Swanson, J. B. Fowlkes, S. Y. Emelianov, "Shear wave elasticity imaging: a new ultrasonic technology of medical diagnostics," *Ultrasound in Med. & Biol.*, vol. 24, no. 9, pp. 1419–1435,1998.

[6] J. Ophir, I. Céspedes, H. Ponnekanti, Y. Yasdi, and X. Li, “Elastography: A Quantitative Method for Imaging the Elasticity of Biological Tissues,” *Ultrason. Imaging*, vol. 13, pp. 111-134, 1991.

[7] J. Ophir, B. Garra, F. Kallel, E. Konofagou, T. A. Krouskop, R. Righetti, and T. Varghese, “Elastographic Imaging,” *Ultrasound Med. Biol.*, vol. 26, no. 1, pp. S23-S29, 2000.

[8] K. J. Parker, D. Fu, S. M. Graceswki, F. Yeung, S. F. Levinson, "Vibration sonoelastography and the detectability of lesions," *Ultrasound in Med. & Biol.*, vol. 24, no. 9, pp. 1437–144, 1998.

[9] K. Sabra, S. Conti, P. Roux, W. Kuperman, “Passive in vivo elastography from skeletal muscle noise,” *Appl. Phys. Lett.*, vol. 90, no. 19, pp.194101 - 194101 - 3,2007.

[10] T. Gallot, S. Catheline, P. Roux, J. Brum, N. Benech, C. Negreira, " Passive elastography: shear-wave tomography from physiological-noise correlation in soft tissues," *IEEE Trans. Ultrason. Ferroelectr. Freq. Control*, vol. 58, no. 6, pp. 1122-1126, 2011.

[11] L. Gao, K. J. Parker, and S. K. Alam, “Sonoelasticity imaging: Theory and experimental verification,” *J. Acoust. Soc. Am.*, vol. 97, no. 6, pp. 3875-3886, 1995.

[12] L. Sandrin, M. Tanter, S. Catheline, and M. Fink, “Shear modulus imaging using 2D transient elastography,” *IEEE Trans. Ultrason. Ferroelectr. Freq. Control*, vol. 51, pp. 396-409, 2004.

[13] A. Manduca, T. E. Oliphani, M. A. Dresner, J. L. Mahowald, S. A. Kruse, E. Amromin, J. P. Felmlee, J. F. Greenleaf, and R. L. Ehman, “Magnetic resonance elastography: Non-invasive mapping of tissue elasticity,” *Medical Image Analysis*, vol. 5, no. 4, pp. 237-254, 2001.

[14] S. Catheline, F. Wu, and M. Fink, “A solution to diffraction biases in sonoelasticity: the acoustic impulse technique,” *J. Acoust. Soc. Am.*, vol 105, no. 5, pp. 2941-2950, 1999.

[15] L. Sandrin, M. Tanter, J.L. Gennisson, S. Catheline, M. Fink, “Shear elasticity probe for soft tissues with 1D transient elastograhy,” *IEEE Trans. Ultras. Ferroelec. Freq. Control*, vol. 49, no. 4, pp. 426-435, 2002.

[16] X. Zhang, B. Qiang, R. D. Hubmayr, M. W. Urban, R. Kinnick, J. F. Greenleaf, “Noninvasive ultrasound image guided surface wave method for measuring the wave speed and estimating the elasticity of lungs: A feasibility study,” *Ultrasonics*, vol. 51, issue 3, pp. 289 – 295, 2011.

[17] K. Nightingale, M. S. Soo, R. Nightingale, and G. Trahey, “Acoustic radiation force impulse imaging: in vivo demonstration of clinical feasibility,” *Ultrasound Med. Biol.*, vol. 28, no. 2, pp. 227-235, 2002.

[18] J. Bercoff, M. Tanter, and M. Fink, “Supersonic shear imaging: A new technique for soft tissue elasticity mapping,” *IEEE Trans. Ultras. Ferroelec. Freq. Control*, vol. 51, pp. 396-409, 2004.

[19] S. Catheline, "Ultrasonic speckle interferometry: application to the elasticity measurement," *PhD Thesis*, University Paris VII, Paris, France, 1998.

[20] J. L. Gennisson, T. Baldeweck, M. Tanter, S. Catheline, M. Fink, L. Sandrin, C. Cornillon, B. Querleux, "Assessment of elastic parameters of human skin using dynamic elastography," *IEEE Trans. Ultras. Ferroelec. Freq. Control*, vol. 51, no. 8, pp. 980-989, 2004.

[21] J. L. Gennisson, C. Cornu, S. Catheline, M. Fink and P. Portero, “Human muscle hardness assessment during incremental isometric contraction using transient elastography,” *J. Biomechanics*, vol. 38, no. 7, pp. 1543-1550, 2005.

[22] N. Benech, C. Negreira, "Monitoring heat-induced changes in soft tissues with 1D transient elastography," *Phys. Med & Biol.*, vol. 55, pp. 1753-1765, 2010.

[23] N.Benech, C. Negreira, G. Brito, "Elastografía ultrasónica para evaluación de terneza en carne vacuna,", pp 29-44, in *"Herramientas tecnológicas aplicadas a calidad y diferenciación de carne",* PROCISUR, ISBN: 9789292483920, Montevideo, 2012.

[24] R. Muthupillai, D. J. Lomas, P. J. Rossman, J. F. Greenleaf, A. Manduca, R. L.Ehman, "Magnetic resonance elastography by direct visualization of propagating acoustic strain waves," *Science*, vol. 269, no. 5232, pp. 1854-1857, 1995.

[25] R. Sinkus, J. Lorenzen, D. Schrader, M. Lorenzen, M. Dargatz, D. Holz. “High-resolution tensor mr elastography for breast tumor detection,” *Physics in Medicine and Biology*, vol. 45, pp. 1649–1664, 2000.

[26] L. Huwart, F. Peeters, R. Sinkus, L. Annet, N. Salameh, “Liver fibrosis : non-invasive assessment with mr elastography,” *NMR in Biomedicine*, vol. 19, no. 2, pp. 173–179, 2006.

[27] M. A. Green, L. E. Bilston, R. Sinkus, “In vivo brain viscoelastic properties measured by magnetic resonance elastography,” *NMR in Biomedicine*, vol. 21, no. 7, pp. 755–64, 2008.

[28] M. A. Dresner, G. H. Rose, P. J. Rossman, R. Muthupillai, A. Manduca, R. L. Ehman, “Magnetic resonance elastography of skeletal muscle,” *J. Mag. Res. Imag.*, vol. 13, no. 2, pp. 269–76, 2001.

[29] G. R. Torr, "The acoustic radiation force," *Am. J. Phys.*, vol. 52, pp. 402–408, 1984.

[30] M. L. Palmeri, M. H. Wang, J. J. Dahl, K. D. Frinkley, K. R. Nightingale, "Quantifying hepatic shear modulus *in vivo* using acoustic radiation force," *Ultrasound in Med. & Biol.*, vol. 34, no. 4, pp. 546–558, 2008.

[31] M. Fatemi, J. F. Greenleaf, "Ultrasound-Stimulated Vibro-Acoustic Spectrography," *Science,* vol. 280, pp. 82 -85, 1998.

[32] M. Fatemi, J. F. Greenleaf, "Vibro-acoustography: an imaging modality based on ultrasound-stimulated acoustic emission," *Proc. Natl. Acad. Sci. USA*, vol. 96, pp. 6603–6608, 1999.

[33] M. W. Urban, A. Alizad, W. Aquino, J. F. Greenleaf, K. E. Thomenius, M. Fatemi, "A review of vibro-acoustography and its applications in medicine," *Curr. Med. Imaging Rev.*, vol. 7, no. 4, pp. 350-359, 2011.

[34] M. W. Urban, C. Chalek, R. R. Kinnick, T. M. Kinter, B. Haider, J. F. Greenleaf, K. E. Thomenius, M. Fatemi, "Implementation of vibro-acoustography on a clinical ultrasound system," *IEEE Trans. Ultras. Ferroelec. Freq. Control*, vol. 58, no. 6, pp. 1169-1181, 2011.

[35] S. Chen, M. Fatemi, J. Greenleaf, “Quantifying elasticity and viscosity from measurement of shear wave speed dispersion,” *J. Acoust. Soc. Am.*, vol. 115, no. 6, pp. 2781–2785, 2004.

[36] T. Deffieux, "Palpation par force de radiation ultrasonore et échographie ultrarapide: applications à la caractérisation tissulaire in vivo," *PhD Thesis*, University Paris VII, Paris, France, 2008.

[37] M. Tanter, J. Bercoff, A. Athanasiou, T. Deffieux, J. L. Gennisson, G. Montaldo, M. Muller, A. Tardivon, and M. Fink, “Quantitative assessment of breast lesion viscoelasticity: Initial clinical results using supersonic shear imaging,” *Ultrasound Med. Biol.*, vol. 34, no. 9, pp. 1373-1386, 2008.

[38] M. Muller, J. L. Gennisson, T. Deffieux, M. Tanter, M. Fink, “Quantitative viscoelasticity mapping of human liver using supersonic shear imaging: preliminary *in vivo* feasability study,” *Ultrasound Med. Biol.*, vol. 35, no. 2, pp. 219-229, 2009.

[39] J. L. Gennisson, T. Deffieux, E. Macé, G. Montaldo, M. Fink, and M. Tanter, “Viscoelastic and anisotropic mechanical properties of in vivo muscle tissue assessed by Supersonic Shear Imaging,” *Ultrasound Med. Biol.*, vol. 36, no. 5, pp. 789-801, 2010.

[40] D. Gallichan, M. D. Robson, A. Bartsch, K. L. Miller, "TREMR: Table-Resonance Elastography with MR," *Mag. Res. in Med.*, vol. 62, pp. 815–821, 2009.

[41] L. Sandrin, B. Fourquet, J. M. Hasquenoph, S. Yon, C. Fournier, F. Mal, C. Christidis, M. Ziol, B. Poulet, F. Kazemi, M. Beaugrand, R. Palau, “Transient elastography: a new noninvasive method for assessment of hepatic fibrosis,” *Ultrasound Med Biol.*, vol. 29, no. 12, pp. 1705-1713, 2003.

[42] E. Dolan, L. Thijs, Y. Li, N.Atkins, P. McCormack, S. McClory, E. O’Brien, J. A. Staessen, A. V. Stanton, “Ambulatory arterial stiffness index as a predictor of cardiovascular mortality in the Dublin Outcome Study,” *Hypertension*, vol. 47, pp. 365–370, 2006.

[43] S. Laurent, P. Boutouyrie, R. Asmar, I. Gautier, B. Laloux, L. Guize, P. Ducimetiere, A. Benetos, “Aortic stiffness is an independent predictor of all-cause and cardiovascular mortality in hypertensive patients,” *Hypertension*, vol. 37, pp. 1236–1241, 2001.

[44] M. Tanter, D. Touboul, J. L. Gennisson, J. Bercoff, and M. Fink, “High resolution quantitative imaging of cornea elasticity using supersonic shear imaging,” *IEEE Trans. Med. Imaging*, vol. 28, no. 2, pp. 1881-1893, 2009.

[45] M. Couade, M. Pernot, C. Prada, E. Messas, J. Emmerich, P. Bruneval, A. Criton, M. Fink and, M. Tanter, “Quantitative assessment of arterial wall biomechanical properties using shear wave imaging,” *Ultrasound Med. Biol.*, vol. 36, no. 10, pp. 1662-1676, 2010.

[46] T. M. Nguyen, M. Couade, J. Bercoff, and M. Tanter, “Assessment of viscous and elastic properties of sub-wavelength layered soft tissues using Shear Wave Spectroscopy: theoretical framework and experimental in vitro experimental validation,” *IEEE Trans. Ultras. Ferroelec. Freq. Control*, vol. 58, no. 11, pp. 2305-2315, 2011.

[47] J. Brum, G. Balay, D. Bia, R. Armentano, C. Negreira, “Feasibilty of a transient elastography technique for in vitro arterial elasticity assessment,” *Proceedings of the 32nd Annual International Conference of the IEEE EMBS*, pp. 37-40, 2010.

[48] J. Brum, J. L. Gennisson, T. M. Nguyen, N. Benech, M. Fink, M. Tanter, C. Negreira, "Application of 1D transient elastography for the shear modulus assessment of thin layered soft tissue: comparison with Supersonic Shear Imaging technique," *IEEE Trans. Ultras. Ferroelec. Freq. Control*, vol. 59, no. 4, pp. 703-714, 2012.

[49] K. Aki and P. G. Richards, "Quantitative Seismology, Theory and Methods" (2nd Edition), vol. 1, Chap. 4, pp. 72.

[50] D. C. Gakenheimer and J. Miklowitz, ‘‘Transient excitation of an elastic half-space by a point load traveling on the surface,’’ *J. Appl. Mech.*, vol. 36, pp. 505, 1969.

[51] M. Bernal, I. Nenadic, M. W. Urban, J. F. Greenleaf, "Material property estimation for tubes and arteries using ultrasound radiation force and analysis of propagating modes," J. Acoust. Soc. Am., vol 129, no. 3, pp. 1344-1354, 2011.

[52] M. J. S Lowe, “Plate waves for the NDT of diffusion bonded titanium,” *PhD Thesis*, Imperial College of Science, Technology and Medicine, University of London, England, 1992.

[53] H. Schmidt and F. B. Jensen, “A full wave solution for propagation in multilayered viscoelastic media with application to Gaussian beam reflection at liquid-solid interfaces,” *J. Acoust. Soc. Am.*, vol. 77, pp. 813-825, 1985.

[54] M. J. S. Lowe, “Matrix techniques for modeling ultrasonic waves in multilayered media,” *IEEE Trans. Ultras. Ferroelec. Freq. Control*, vol. 42, pp. 525-542, 1995.

[55] M. Couade, “Imagerie des propriétés viscoélastiques du coeur et des artères par échographie ultrarapide et palpation à distance,” *PhD Thesis*, University Paris VII, Paris, France, 2011.

[56] J. A. Nelder and R. Mead, “A simplex method for function minimization,” *Computer Journal*, vol. 7, pp. 308-313, 1965.

[57] J. Fromageau, J. L. Gennisson, C. Schmitt, R. L. Maurice, R. Mongrain, G. Cloutier, “Estimation of ployvinil alcohol cryogel mechanical properties with four ultrasound elastography methods and comparison with gold standard testings,” *IEEE Trans. Ultras. Ferroelec. Freq. Control*, vol. 54, no. 3, pp. 498-509, 2007.

[58] M. Tanter, “Application of time reversal to brain hyperthermia,” *PhD Thesis*, University Paris VII, Paris, France, 1999.

[59] T. Deffieux, J. L. Gennisson, J. Bercoff and M. Tanter, “On the effects of reflected waves in transient shear waves elastography,” *IEEE Trans. Ultras. Ferroelec. Freq. Control*, vol. 58, no. 10, pp. 2032-2035, 2011.

[60] C. Prada, D. Clorennec and D. Royer, “Local vibration of an elastic plate and zero-group velocity Lamb modes,” *J. Acoust. Soc. Am.*, vol 124, no. 1, pp. 203-212, 2008.

[61] T. Deffieux, G. Montaldo, M. Tanter, and M. Fink, “Shear wave spectroscopy for in vivo quantification of human soft tissues visco-elasticity,” *IEEE Trans. Med. Im.*, vol. 28, no. 3, pp. 313-322, 2009.

[62] G. Lerosey, J. de Rosny, A. Tourin, and M. Fink, “Focusing beyond the diffraction limit with far-field time-reversal,” *Science*, vol. 315, pp. 1120–1122, 2007.

[63] P. Roux and M. Fink, “Time-reversal in a waveguide: Study of the temporal and spatial focusing,” *J. Acoust. Soc. Am.*, vol. 107, pp. 2418–2429, 2000.

[64] N . Chakroun, M. Fink, and F. Wu, “Time-reversal processing in ultrasonic non-destructive control,” *IEEE Trans. Ultrason. Ferroelectr. Freq. Control*, vol. 42, pp. 1087–1098, 1995.

[65] R . Ing, N. Quieffin, S. Catheline, and M. Fink, “In solid localization of finger impacts using acoustic time-reversal process,” *Appl. Phys. Lett.*, vol. 87, art. no. 204104, 2005.

[66] J. L. Thomas, F. Wu, and M. Fink, “Time-reversal focusing applied to lithotripsy,” *Ultrason. Imaging*, vol. 18, pp. 106–121, 1996.

[67] F. Wu, J. L. Thomas, M. Fink, "Time reversal of ultrasonic fields part II: Experimental results," *IEEE Trans. Ultrason. Ferroelectr. Freq. Control*, vol. 39, no. 5, pp. 567–578, 1992.

[68] C. Draeger and M. Fink, "One-channel time-reversal in chaotic cavities: theoretical limits," *J. Acoust. Soc. Am.*, vol. 105, pp. 611–617, 1999.

[69] J. Brum, "Métodos para la evaluación de la elasticidad del tejido arterial," *Master Thesis*, PEDECIBA - Física, Universidad de la República, Montevideo, Uruguay, 2009.

[70] E. de Castro and C. Morandi, "Registration of rotated and translated images using finite Fourier transforms," *IEEE Trans. Pattern Anal. Mach. Intell.*, vol. 9, pp. 700–703, 1987.

[71] R. Snieder, K. Wapenaar, U. Wegler, "Unified Green's function retrieval by cross-correlation; Conection with energy principles," *Phys. Rev. E*, vol. 75, art. no. 036103, 2007.

[72] F. J. Sánchez-Sesma, J.A. Pérez-Ruiz, F. Luzón, M. Campillo, A. Rodríguez-Castellanos, "Diffuse fields in dynamic elasticity," *Wave Motion*, vol. 45, pp. 641-654, 2008.

[73] K. Wapenaar, "Retriving the Green's function of an arbitrary inhomogeneous medium by cross-correlation," *Phys. Rev. Lett.*, 93, art. no. 254301, 2004.

[74] O. Lobkis and R. Weaver, "On the emergence of Green's function in the correlations of a diffuse field," *J. Acoust. Soc. Am.*, vol. 110, pp. 3011-3017, 2001.

[75] M. Campillo and A. Paul, "Long-range correlations in the diffuse seismic coda," *Science*, vol. 299, pp. 547-549, 2003.

[76] A. E. Malcom and J. A. Scales, "Extracting the Green's function from diffuse, equipartitioned waves," *Phys. Rev. E*, vol. 70, art. no. 015601, 2004.

[77] L. Stehly, M. Campillo, N. Shapiro, "A study of seismic noise from its long-range correlation properties," *J. Geoph. Research*, vol. 111, art. no. B10306, 2006.

[78] R. L. Weaver and A. J. Lobkis, "Ultrasonics without a source: Thermal fluctuation correlations at MHz frequencies," *Phys. Rev. Lett.*, vol. 87, art. no. 134301, 2001.

[79] K. Sabra, P. Gerstoft, P. Roux and W. Kuperman, "Extracting time-domain Green's function from ambient seismic noise," *Geoph. Res. Lett.*, vol. 32, art. no. L03310, 2005.

[80] P. Roux, K. G. Sabra, W. A. Kuperman, A. Roux, "Ambient noise cross-correlation in free space: Theoretical approach," *J. Acoust. Soc. Am.*, vol. 117, pp. 79-84, 2005.

[81] K. Aki and P. G. Richards, "Quantitative Seismology, Theory and Methods" (2nd Edition), vol. 1, Chap. 4, p. 85.

[82] F. J. Sánchez-Sesma and M. Campillo, “Retrieval of Green’s function from cross-correlation: The canonical elastic problem,” *Bull. Seismol. Soc. Am.*, vol. 96, pp. 1182-1191, 2006.

[83] W. F. Walker and G. E. Trahey, ‘‘A fundamental limit on the performance of correlation based on phase correction and flow estimation technique,’’ *IEEE Trans. Ultrason. Ferroelectr. Freq. Control,* vol. 41, no. 5, pp. 646 -654, 1994.

[84] R. Weaver, B. Froment, M. Campillo, “On the correlation of nonisotropically distributed ballistic scalar diffuse waves,” *J. Acoust. Soc. Am.*, vol. 126, no. 4, pp. 1817–1826, 2009.

[85] P. Gouedard, P. Roux, M. Campillo, A. Verdel, “Convergence of the two-point correlation function toward the Green’s function in the context of a seismic-prospecting data set,” *Geophysics*, vol. 73, no. 6, pp. V47–V53, 2008.

[86] M. Tanter, J. L. Thomas, M. Fink, "Time reversal and the inverse filter," *J. Acoust. Soc. Am.*, vol. 108, no. 1, pp. 224-234, 2000.

[87] M. Nieto-Vesperinas, "Scattering and diffraction in physical optics," (2nd Edition, World Scientific Printers), Chapter 2, p. 38.

[88] M. von Laue, "The variability of ray beams" *,Annalen der Physik.*, vol. 44, no. 16, pp. 1197 - 1212, 1914.

[89] D. Gabor, in *Proc. of the Symp. of Astronomical Optics* (ed. Z. Kopal, North-Holland, Amsterdam), p. 17, 1956.

[90] D. Gabor, "The transmission of information by coherent light I. Classical theory," *J. Phys. E: Sci. Instrum.*, vol 8, pp. 73-78, 1975.

[91] G. Toraldo di Francia, "Degrees of freedom of an image," *J. Opt. Soc. Am.*, vol 59, no. 7, pp. 799-804, 1969.

[92] J.-F. Aubry, M. Tanter, J. Gerber, J. L. Thomas, M. Fink, "Optimal focusing by spatio-temporal inverse filter. II. Experiments. Application to focusing through absorbing and reverberating media," *J. Acoust. Soc. Am.*, vol. 110, no. 1, pp. 48-58, 2001.

[93] T. Gallot, S. Catheline, P. Roux, M. Campillo, "A passive inverse filter for Green’s function retrieval," *J. Acoust. Soc. Am.*, vol. 131, no. 1, pp. EL21-EL27, 2012.

[94] S. Catheline, J. L. Gennisson, G. Delon, M. Fink, R. Sinkus, S. Abouelkaram, J. Culiolic, "Measurement of viscoelastic properties of homogeneous soft solid using transient elastography: an inverse problem approach," *J. Acoust. Soc. Am.*, vol. 116, no. 6, pp. 3734-3741, 2004.

[95] G. Ribay, "Localisation de source en milieu réverbérant par retournement temporel," *PhD Thesis*, University Paris VII, Paris, France, 2006.

[96] G. Ribay, S. Catheline, D. Clorennec, R. K. Ing, N. Quieffin, M. Fink, "Acoustic impact localization in plates: properties and stability to temperature variation," *IEEE Trans. Ultrason. Ferroelectr. Freq. Control*, vol. 54, no. 2, pp. 378 - 385, 2007.

[97] B. Pavlakovic and M. J. S. Lowe, "DISPERSE a system for generation dispersion curves," User's manual, version 2.0.16B, p. 194, 2003.

[98] D. Cassereau and M. Fink, " Time-reversal of ultrasonic fields part III: theory of the closed time-reversal cavity," *IEEE Trans. Ultrason. Ferroelectr. Freq. Control*, vol. 39, no. 5, pp. 579 - 592, 1992.